
AFRL-RX-WP-TR-2018-0062

# MICROSTRUCTURAL AND MECHANICAL CHARACTERIZATION OF 2-D AND 3-D SiC/SiNC CERAMIC-MATRIX COMPOSITES

**Larry Zawada**
**Universal Technology Corporation**

**Lawrence E. Carson and Craig Przybyla**
**AFRL/RXCCP**

**23 FEBRUARY 2018**
**Final Report**



**AIR FORCE RESEARCH LABORATORY**
**MATERIALS AND MANUFACTURING DIRECTORATE**
**WRIGHT-PATTERSON AIR FORCE BASE, OH 45433-7750**
**AIR FORCE MATERIEL COMMAND**
**UNITED STATES AIR FORCE**

# NOTICE AND SIGNATURE PAGE

Using Government drawings, specifications, or other data included in this document for any purpose other than Government procurement does not in any way obligate the U.S. Government. The fact that the Government formulated or supplied the drawings, specifications, or other data does not license the holder or any other person or corporation; or convey any rights or permission to manufacture, use, or sell any patented invention that may relate to them.

Qualified requestors may obtain copies of this report from the Defense Technical Information Center (DTIC) (http://www.dtic.mil).

AFRL-RX-WP-TR-2018-0062 HAS BEEN REVIEWED AND IS APPROVED FOR PUBLICATION IN ACCORDANCE WITH ASSIGNED DISTRIBUTION STATEMENT.

//SIGNATURE//
CRAIG P. PRZYBYLA
Project Engineer
Composite Branch
Structural Materials Division
Materials and Manufacturing Directorate

//SIGNATURE//
TIMOTHY D. BREITZMAN
Branch Chief
Composite Branch
Structural Materials Division
Materials and Manufacturing Directorate

//SIGNATURE//
AMBER I. DAVIS
Deputy Division Chief
Structural Materials Division
Materials And Manufacturing Directorate

This report is published in the interest of scientific and technical information exchange, and its publication does not constitute the Government's approval or disapproval of its ideas or findings.

# REPORT DOCUMENTATION PAGE

*Form Approved*
*OMB No. 0704-0188*



| 1. REPORT DATE *(DD-MM-YY)* | 2. REPORT TYPE | 3. DATES COVERED *(From - To)* |
|---|---|---|
| 23 February 2018 | Final | 1 March 2004 – 1 March 2005 |

**4. TITLE AND SUBTITLE**
MICROSTRUCTURAL AND MECHANICAL CHARACTERIZATION OF 2-D AND 3-D SiC/SiNC CERAMIC-MATRIX COMPOSITES

**5a. CONTRACT NUMBER**
In-House

**5b. GRANT NUMBER**

**5c. PROGRAM ELEMENT NUMBER**
62102F

**6. AUTHOR(S)**
Larry P. Zawada –UTC
Lawrence E. Carson and Craig Przybyla – AFRL/RXCC

**5d. PROJECT NUMBER**
4347

**5e. TASK NUMBER**

**5f. WORK UNIT NUMBER**
X0S7

**7. PERFORMING ORGANIZATION NAME(S) AND ADDRESS(ES)**
AFRL/RXCC
AFRL Materials and Manufacturing Directorate
2230 Tenth Street, Suite 1
Wright-Patterson AFB, OH 45433-7750

Universal Technology Corporation
1270 North Fairfield Road
Dayton, OH 45432-2600

**8. PERFORMING ORGANIZATION REPORT NUMBER**
AFRL-RX-WP-TR-2018-0062

**9. SPONSORING/MONITORING AGENCY NAME(S) AND ADDRESS(ES)**
Air Force Research Laboratory
Materials and Manufacturing Directorate
Wright-Patterson Air Force Base, OH 45433-7750
Air Force Materiel Command
United States Air Force

**10. SPONSORING/MONITORING AGENCY ACRONYM(S)**
AFRL/RXCC

**11. SPONSORING/MONITORING AGENCY REPORT NUMBER(S)**
AFRL-RX-WP-TR-2018-0062

**12. DISTRIBUTION/AVAILABILITY STATEMENT**
Distribution Statement A. Approved for public release; distribution unlimited.

**13. SUPPLEMENTARY NOTES:**
Report contains color. Cleared 88ABW-2017-5865 on 20Nov2017.

**14. ABSTRACT (*Maximum 200 words*):**
Microstructural and mechanical characterization of SiC/SiNC ceramic-matrix composite (CMC) materials was conducted. Materials investigated in this study were woven composite systems in both 2-D and 3-D weave architectures. Two matrix precursors were evaluated for tensile, creep, and shear applications: the standard S200-1 and the Starfire® resin systems. In addition, two different ply thicknesses were evaluated: a 4-ply, 0.080-inch laminate and a 9-ply, 0.145-inch material..

**15. SUBJECT TERMS**
Ceramic-matrix composites, SiC/SiNC, tensile, interlaminar shear, creep, stress rupture, elevated temperature

| 16. SECURITY CLASSIFICATION OF: | | | 17. LIMITATION OF ABSTRACT: | 18. NUMBER OF PAGES | 19a. NAME OF RESPONSIBLE PERSON (Monitor) |
|---|---|---|---|---|---|
| a. REPORT | b. ABSTRACT | c. THIS PAGE | SAR | 148 | Craig Przybyla |
| Unclassified | Unclassified | Unclassified | | | 19b. TELEPHONE NUMBER *(Include Area Code)* (937) 255-9396 |

## TABLE OF CONTENTS

**Section** **Page**

List of Figures ..... iii
List of Tables ..... vi
PREFACE ..... vii
1.0 SUMMARY ..... 1
2.0 INTRODUCTION ..... 2
2.1 Background ..... 2
2.2 Program Objectives ..... 2
3.0 PROCEDURES ..... 4
3.1 Materials Description ..... 4
3.1.1 S200 Matrix. ..... 4
3.1.2 Starfire Matrix Material ..... 5
3.1.4 Fiber Coating. ..... 6
3.1.5 2-D. ..... 6
3.1.6 3-D. ..... 6
3.1.7 Acceptance Criteria. As part of the purchase agreement, COIC agreed to meet certain requirements, one of which was that the as-manufactured 2-D S200 material would exhibit a room-temperature (RT) tensile strength of >170 MPa. However, the 3-D materials are developmental. Therefore, no strength requirement was required and production would be on a best-effort basis. ..... 7
3.2 Panels and Test Specimens ..... 7
3.3 Test Plan ..... 8
3.4 Test Equipment Description ..... 12
3.4.1 Test System: SH#12. ..... 12
3.4.2 Shear Testing. ..... 14
3.4.3 Verification of Alignment for Servo-Hydraulic Test Frame. ..... 14
3.5 Material Characterization ..... 18
4.0 RESULTS ..... 20
4.1. Microstructural Analysis ..... 20
4.2 Porosity Measurements ..... 27
4.3 Tension Tests ..... 33
4.4 Creep Rupture Tests ..... 35
4.5 Fatigue Tests ..... 43
4.6 Shear Testing ..... 45
4.7 Transthickness Tension Tests ..... 47
5.0 DISCUSSION ..... 48
5.1 Tensile Results ..... 48
5.2 Residual Strength of Test Specimens Reaching Run-Out ..... 48
5.3 Fracture Surface Studies and Microstructural Analysis ..... 50
6.0 CONCLUSIONS ..... 53
7.0 RECOMMENDATIONS ..... 54
8.0 REFERENCES ..... 55
APPENDIX A ..... 56
A-1 MICROGRAPH IMAGES ..... 56
A-2 3-D, S200-1, 80 MIL ..... 61

A-3 3-D, S200-1, 145 MIL .....67
A-4 3-D, STARFIRE, 80 MIL .....75
A-5 3-D, STARFIRE, 80 MIL .....77
APPENDIX B .....81
B-1 FRACTURED SURFACE.....81
B-2 POLISHED SURFACE .....103
APPENDIX C: Stress vs. strain plots .....130
C-1 2-D, S200-1, 80 MIL .....130
C-2 3-D, S200-1, 80 MIL .....131
C-3 3-D, S200-1, 145 MIL .....133
C-4 3-D, STARFIRE, 80 MIL .....134
C-5 3-D, STARFIRE, 80 MIL .....136
LIST OF ACRONYMS, ABBREVIATIONS, AND SYMBOLS .....138

## LIST OF FIGURES

**Figure** **Page**

Figure 1. Simple Schematic of PIP Manufacturing Process Used to Manufacture CMC Panels Used in This Study ..... 5

Figure 2. SEM Image of Nine-Ply 3-D Fiber Preform. Image Clearly Shows Warp, Fill, and Warp Weaver Tows ..... 7

Figure 3. Diagram of S200 2-D Panel and Location of Test Specimens ..... 7

Figure 4. Diagram of 3-D SiC/SiNC Panels and Location of Test Specimens ..... 8

Figure 5. Schematic of Dogbone Specimen Used for All Tension, Creep, and Fatigue Testing .. 9

Figure 6. Double-Notch Compression Test Specimen Geometry ..... 10

Figure 7. Short-Beam Shear Test Specimen Geometry ..... 10

Figure 8. Short-Beam Shear Test Fixture ..... 11

Figure 9. Photograph of Horizontal Servo-Hydraulic Test System Used for Room- and Elevated-Temperature Testing ..... 13

Figure 10. This Photograph Highlights Wedge grips, Furnace, and Insulating Box Used to Minimize Noise in Strain Measurements ..... 13

Figure 11. Enclosure Used to Minimize Noise in Extensometer Resulting from Air Currents in Laboratory ..... 14

Figure 12. Strain-Gaged Steel Alignment Specimen Used to Verify Alignment ..... 14

Figure 13. Plot of Bending Strain Versus Average Axial Strain for Alignment Check of SH#12 ..... 15

Figure 14. Schematic Showing Placement of Thermocouples for Furnace Temperature Mapping ..... 16

Figure 15. Example ofCMC Test Specimen Instrumented with Thermocouples for Furnace Temperature Mapping ..... 17

Figure 16. Example of CMC Test Specimen Instrumented with Thermocouples for Furnace Temperature Mapping ..... 17

Figure 17. Temperature Profile Conducted on General Electric (GE) Gen 1.1 Mi-HiNiC/SiC Test Specimen ..... 18

Figure 18. Schematic Showing Actual Test Specimens Sectioned for Microstructural Studies. Double Lines Indicate Surfaces Polished and Studied. ..... 19

Figure 19. Method Used to Calculate Net Cross-Sectional Area ..... 20

Figure 20. Optical Micrograph of 3-D S200 80-mil CMC Showing How Z-Weaving Fibers Contribute to Almost Doubling Thickness ..... 21

Figure 21. Change in Stress-Versus-Strain Behavior When Comparing Net Thickness to Gross Thickness ..... 22

Figure 22. 2-D S200-1 @ 25×, AB ..... 23
Figure 23. 2-D S200-1 @ 25×, A ..... 23
Figure 24. 3-D S200-1, 80 mil @ 50×, AB ..... 24
Figure 25. 3-D S200-1, 145 mil @ 25×, AB ..... 24
Figure 26. 3-D S200-1, 145 mil @ 100×, AB ..... 25
Figure 27. 3-D Starfire, 80 mil @ 25×, AB ..... 25
Figure 28. 3-D Starfire, 80 mil @ 50×, AB ..... 26
Figure 29. 3-D Starfire, 145 mil @ 25×, AB ..... 26
Figure 30. 3-D Starfire, 145 mil @ 50×, AB ..... 27
Figure 31. Bar Chart Showing Percent Porosity for 2-D S200 and 3-D SiC/SiNC Manufactured with S200 Resin and Starfire Resin ..... 29
Figure 32. Porosity Pore Size Measurements for 2-D S200 6 Ply and 3-D S200 80 Mil Using Mercury Porosimeter ..... 30
Figure 33. Porosity Pore Size Measurements for 2-D S200 6 Ply, 3-D S200 80 Mil, and 3-D Starfire 80-Mil Using Mercury Porosimeter ..... 30
Figure 34. Porosity Pore Size Measurements for 2-D S200 6 Ply and 3-D Starfire 80 Mil Using Mercury Porosimeter ..... 31
Figure 35. Porosity Pore Size Measurements for 3-D Starfire 80 Mil and 3-D Starfire 145 Mil Using Mercury Porosimeter ..... 31
Figure 36. Porosity Pore Size Measurements for 3-D S200 145 Mil and 3-D Starfire 145 Mil Using Mercury Porosimeter ..... 32
Figure 37. Porosity Pore Size Measurements for 3-D S200 80 Mil and 3-D Starfire 80 Mil Using Mercury Porosimeter ..... 32
Figure 38. Porosity Pore Size Measurements for 3-D S200 80 Mil and 3-D S200 145 Mil Using Mercury Porosimeter ..... 33
Figure 39. Tensile Stress-Versus-Strain Behavior for 2-D S200 and 3-D SiC/SiNC Manufactured with S200 Resin and Starfire Resin ..... 35
Figure 40. Creep Rupture Plot Showing Net Stress Versus Time to Failure in Seconds for 2-D S200 and 3-D SiC/SiNC Manufactured with S200 Resin and Starfire Resin ..... 37
Figure 41. Creep Rupture Data for 2-D S200 versus S200-1 ..... 37
Figure 42. Creep Strain Versus Time for 2-D S200 Creep Tested at 1000°C ..... 38
Figure 43. Total Creep Strain Versus Time for 2-D S200 Creep Tested at 1000°C ..... 39
Figure 44. Creep Strain Versus Time for 3-D S200 80 Mil Creep Tested at 1000°C ..... 39
Figure 45. Total Strain Versus Time for 3-D S200 80 Mil Creep tested at 1000°C ..... 40
Figure 46. Creep Strain Versus Time for 3-D S200 145 Mil Creep Tested at 1000°C ..... 40

Figure 47. Total Strain Versus time for 3-D S200 145 mil Creep Tested at 1000°C ..... 41
Figure 48. Creep Strain Versus Time for 3-D Starfire 80 Mil Creep Tested at 1000°C ..... 41
Figure 49. Total Strain Versus Time for 3-D Starfire 80 Mil Creep Tested at 1000°C ..... 42
Figure 50. Creep Strain Versus Time for 3-D Starfire 145 Mil Creep Tested at 1000°C ..... 42
Figure 51. Total Strain Versus Time for 3-D Starfire 145 Mil Creep Tested at 1000°C ..... 43
Figure 52. Fatigue Plot of Net Stress Versus Cycles to Failure for 2-D S200 and 3-D SiC/SiNC Manufactured with S200 Resin and Starfire Resin ..... 44
Figure 53. Fatigue Plot of Net Stress Versus Cycles to Failure for 2-D SiC/SiNC S200-1 Compared to Data Generated on S200-0 Manufactured in 1994 ..... 45
Figure 54. Double-Notch Compression Shear Stress Values for 2-D S200 and 3-D SiC/SiNC Manufactured with S200 Resin and Starfire Resin ..... 47
Figure 55. Short-Beam Shear Stress Values for 2-D S200 and 3-D SiC/SiNC Manufactured with S200 Resin and Starfire Resin ..... 47
Figure 56. SEM Image of Polished 2-D S200-1, 80 mil @ 1000× ..... 51
Figure 57. SEM Image of Fractured 2-D S200-1, 80 mil @ 1000× ..... 51
Figure 58. SEM Image of Fractured 2-D S200, 80 mil @ 5000× ..... 51
Figure 59. SEM Image of Polished 3-D S200-1, 145 mil @ 1000× ..... 52
Figure 60. SEM Image of Fractured 3-D S200, 145 mil @ 1000× ..... 52

## LIST OF TABLES

**Table** **Page**

Table 1. Actual Net Thickness Measurements Made on Polished Cross-Sections of Test Specimens ..... 21

Table 2. Average Net Thickness Values Used to Calculate Net Stress Values ..... 22

Table 3. Density Measurements Using Archimedes Method for 2-D S200 and 3-D SiC/SiNC Manufactured with S200 Resin and Starfire Resin ..... 27

Table 4. Percent Open Porosity Measurements Using Archimedes Method for 2-D S200 and 3-D SiC/SiNC Manufactured with S200 Resin and Starfire Resin ..... 28

Table 5. Data from Mercury Porosimeter for 2-D S200 and 3-D SiC/SiNC Manufactured with S200 Resin and Starfire Resin ..... 29

Table 6. Tension Test Results for 2-D S200 and 3-D SiC/SiNC Manufactured with S200 Resin and Starfire Resin ..... 34

Table 7. Creep Rupture Results for 2-D S200 and 3-D SiC/SiNC Manufactured with S200 Resin and Starfire Resin ..... 36

Table 8. Fatigue Results for 2-D S200 and 3-D SiC/SiNC Manufactured with S200 Resin and Starfire Resin ..... 44

Table 9. Shear Results for 2-D S200 and 3-D SiC/SiNC Manufactured with S200 Resin and Starfire Resin ..... 46

Table 10. Residual Strength Tension Test Results for Creep Rupture Specimens Reaching Run-Out ..... 48

Table 11. Residual Strength Tension Test Results for Fatigue Specimens Reaching Run-Out . 49

## PREFACE

Mr. Larry Zawada of Universal Technology Corporation provided overall program guidance, Lt. Lawrence Carson of the Air Force Research Laboratory, Materials and Manufacturing Directorate, Composite Branch (AFRL/RXCC) at Wright-Patterson AFB, OH, performed the majority of the metallurgical investigations, and Dr. Edmund Moore of AFRL's Acquisition Support Branch (RXSC) provided overall assistance with testing. Craig Przybyla of the Air Force Research Laboratory, Materials and Manufacturing Directorate, Composite Branch (AFRL/RXCC) at Wright-Patterson AFB, OH, was the in-house research team leader. Special thanks are given to Mr. John Ruschau, University of Dayton Research Institute (UDRI) on-site program manager, for some of the testing, and also to Mr. Kenneth Combs of UDRI, who performed some of the mechanical tests and data reduction. Others involved include Pratt-Whitney, Mr. Kent Busker of MRD for expertise and knowledge provided, and COI Ceramics, Inc. (COIC) for manufacturing of components.

## 1.0 SUMMARY

The purpose of this endeavor was to investigate the effect of 3-D weave architecture on PIP-processed ceramic-matrix composites (CMC). Microstructural studies were performed to document the resulting microstructure. Mechanical testing was performed to determine the high-temperature durability of the five different variants of SiC/SiNC CMC investigated. The work was administered by AFRL/RXCC.

## 2.0 INTRODUCTION

### 2.1 Background

Ceramic-based material systems have the potential for significant weight reduction, greater fuel savings, and performance improvements in aerospace gas turbine engine (GTE) applications over their conventional metallic counterparts due to their higher specific strength properties and temperature capabilities. Of current interest to the United States Air Force (USAF) is the use of CMC materials such as SiC/SiNC laminates for aerospace turbine engine exhaust nozzle applications. For these types of applications, there is concern over inadequate interlaminar shear strength. In an attempt to reduce delamination problems that sometimes occur in two-dimensional (2-D) laminates, three-dimensional (3-D) architectures were examined. It is thought that a 3-D fiber preform should increase shear strength of the resulting laminate. Improvements in shear properties through 3-D architectures will result in changes to the in-plane strength and durability properties. Thus, the influence of the 3-D architecture on mechanical properties needed to be thoroughly evaluated.

In this effort, two lay-up constructions (i.e., 2-D and 3-D weave) were examined, along with two different precursor resin systems. Properties examined include tensile, creep, fatigue, and interlaminar shear, all at 1000°C. In addition to the varying weave construction and matrix resin systems, two laminate thicknesses (i.e., varying number of plies) were evaluated. Details of the materials, procedures, and resulting mechanical properties are described in the following sections.

### 2.2 Program Objectives

The overall objective of this research project was to evaluate the effect of a 3-D weave on the mechanical behavior and durability of SiC/SiNC by using the 2-D CMC as the baseline. The 3-D specimen would evaluate the standard-matrix precursor (S200) and one made by a Starfire®. Applying coatings to the fibers in a 3-D preform is challenging, so preforms with thicknesses of 2.03 mm (0.080 inches or 80 mil) and 3.68 mm (0.145 inches or 145 mil) were investigated. In much of the report, the preforms are referred to as either 80 mil or 145 mil preforms. In addition, these thicknesses are representative of exhaust nozzle components, which are briefly described in a following section.

The following CMCs were manufactured: 1) 2-D material with the S200 matrix pre-curser and 6 plies to produce a 2.03 mm (80 mil) thickness; 2) 3-D material with S200 prepreg followed by infiltration with S200 matrix precursor and 2.03 mm (80 mil) thickness; 3) 3-D material with S200 prepreg followed by infiltration with S200 matrix precursor and 3.68 mm (145 mil) thickness, 4) 3-D material with S200 prepreg followed by infiltration of Starfire matrix precursor and 2.03 mm (80 mil) thickness; and 5) 3-D material with S200 prepreg followed by infiltration of Starfire matrix precursor and 3.68 mm (145 mil) thickness. The following mechanical behavior tests were utilized to evaluate the strength and durability of the five CMC systems: tensile, creep, fatigue, interlaminar tension, and interlaminar shear.

In addition, extensive characterization was performed. This included optical and scanning electron microscopy (SEM) of the microstructure, porosity measurements, studies of fracture surfaces of the failed specimens from the mechanical behavior testing.

## 3.0 PROCEDURES

### 3.1 Materials Description

**3.1.1 S200 Matrix.** The S200 matrix is often called silicon carbonitride or silicon nitrocarbide (SiNC), but is most often described as simply silicon-nitrogen-carbon. The exact composition of the matrix is considered proprietary to COIC. For this study, the SiNC matrix was an improved version and is, therefore, sometimes referred to as S200-1. For this report, it will be referred to as either S200-1 or just S200. If reference is made to the earlier version of the matrix material, it will always be referred to as S200-0. The CMCs were prepared by the polymer-infiltrated pyrolysis (PIP) method.

The manufacturing process for the CMC materials was as follows. Fibers were first woven into cloth or 3-D weaves to form a fiber preform. The preforms were then given a fiber coating of boron nitride (BN) and silicon nitride ($Si_3N_4$). The BN provides a weak layer to promote debonding while the $Si_3N_4$ protects the BN during subsequent processing. The coated fiber preforms were then infiltrated with a liquid ceramic precursor that contains a filler of $Si_3N_4$ powder. The infiltrated fiber preforms were cured with the standard processing methods of vacuum bagging, autoclave pressure, and heat cycling, which are used to make organic-matrix composites. These cured composites provided preforms for converting to a ceramic by heating the composite in a non-reactive atmosphere to pyrolyze the organic polymer. The result of the pyrolysis was a matrix containing silicon, oxygen, nitrogen and carbon. After this first pyrolysis cycle, the preform was infiltrated with only the matrix resin and then went through the PIP cycle. A total of approximately nine PIP cycles were used to reduce the porosity to under approximately 5%. COIC reported that the S200 composite has a reported bulk density of about 2.2 $gm/cm^3$ with an open porosity of about 5%, as measured by water immersion. A schematic of the PIP process is shown in Figure 1.

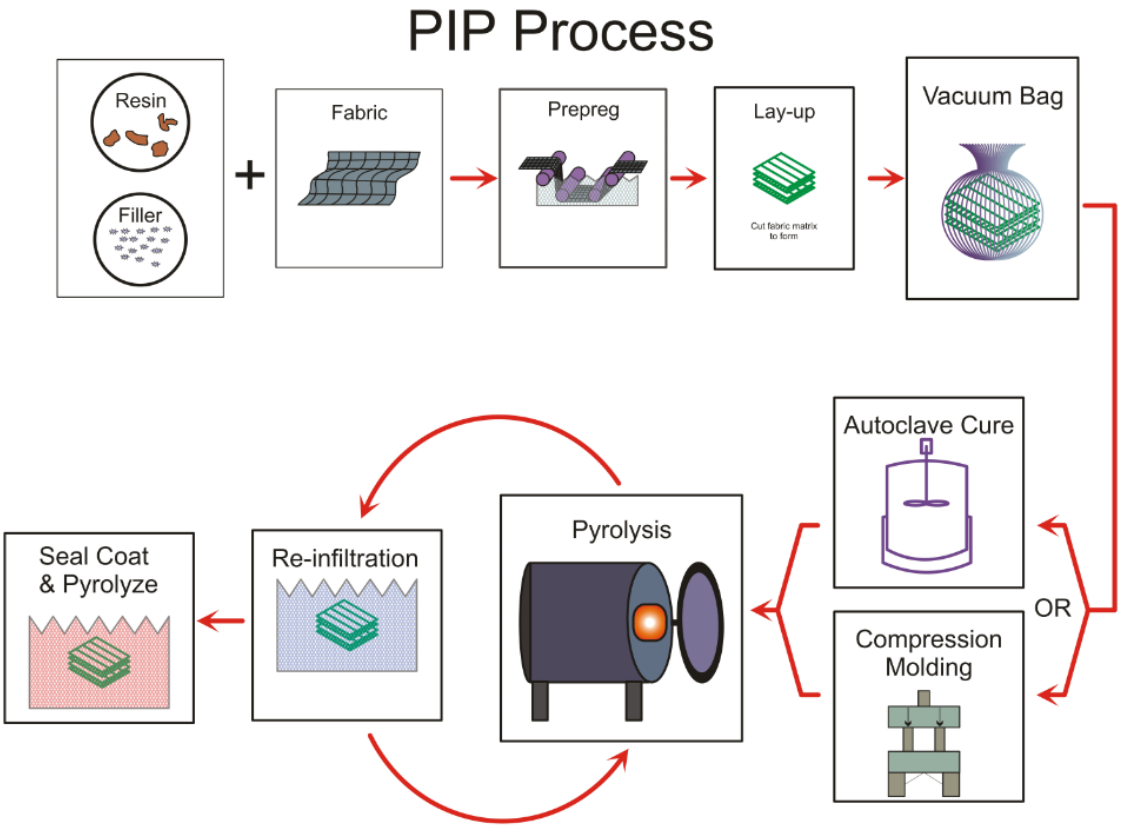


**Figure 1. Simple Schematic of PIP Manufacturing Process Used to Manufacture CMC Panels Used in This Study**

**3.1.2 Starfire Matrix Material.** The Starfire matrix material used in this investigation was the SMP-10 silicon carbide (SiC)-matrix precursor. This material is a one-component liquid precursor to silicon carbide. It has a low-temperature green cure at 180-400°C, and forms amorphous SiC at 850-1200°C with minimal shrinkage, 81% ceramic yield. Nano-crystalline Beta-SiC forms at 1250-1700°C with a 75-80% yield. The polymer name is Allylhydridopolycarbosilane and it has a viscosity of 80-100 CPS at 20°C.

Processing of this matrix material was similar to that used for the S200 matrix material. However, it is important to note that the preforms were first infiltrated with S200 resin with the filler, then all subsequent infiltration cycles were with the SMP-10 resin.

**3.1.3 Fiber.** The fiber used in the manufacturing of the CMC was ceramic-grade (CG) Nicalon™ (1800 denier, type NL-202, 1.2% M sizing). This fiber is often referred to as a SiC fiber, but is actually an amorphous silicon oxycarbide (SiOC) fiber that contains approximately 57% weight percent Si, 31% weight percent C, and 10% weight percent O. The fiber is homogeneously composed of ultra-fine beta-SiC crystallites and an amorphous mixture of silicon, carbon, and oxygen. The fiber comes in many grades – typical fibers are 14 microns in diameter and exhibit a tensile strength of ~2.6 GPa.

**3.1.4 Fiber Coating.** Fiber coating consisted of a boron-nitride layer applied to the fiber which serves as the debond layer. A silicon-nitride layer was placed over the boron-nitride layer both to protect it during PIP processing and to serve as an oxidative protection layer. Application of the fiber coatings is very critical, and uniform coating of each individual fiber is required for optimum composite strength.

**3.1.5 2-D.** The baseline material utilized fabric of ceramic-grade Nicalon woven in an eight-harness satin weave (8HSW). The composites were fabricated with a warp-aligned layup, and flipping of the plies to allow for nesting was not utilized. A total of six plies were used to manufacture the baseline 2-D material with a resultant total fiber volume of approximately 40%. The goal was to produce panels that would be approximately 2 mm thick (0.080 mil).

**3.1.6 3-D.** The three dimensional weave investigated was designed to attempt maximizing in-plane properties and be as nearly uniform in the x and y directions as possible. Therefore, the warp and fill fiber tows were allowed to remain relatively straight, and float warp weavers were used to hold the preform together and provide through-thickness reinforcement. The weave architecture was to be 43/35/22, 50°, with a fiber volume fraction of 36%. The float warp weavers passed completely through the thickness of the preform and then passed over two fill fiber tows at the surface, such that the bending radius would not be too small. Past experience with float warp weavers passing over one fill fiber tow resulted in a very sharp radius, many broken fibers in the weaver tow, and a much tighter-packed fiber preform. It is this tight packed preform that makes fiber coating and matrix infiltration much more difficult and non-uniform.

It was decided to investigate both a thin and thick 3-D weave. The thin weave was to represent a potential thickness for an exhaust nozzle divergent flap insert [1], while the thicker weave represented a potential thickness for an exhaust nozzle's divergent seal [2]. In addition, as stated above, the thicker the fiber preform, the more difficulty in coating all the fibers uniformly with an interphase coating. Therefore, investigating a thicker preform was important to determine how well it could be infiltrated.

The thin 3-D weave utilized nine layers (four warp layers and five fill layers) and float warp weavers that passed through the entire thickness and then over two fill tows. The target thickness was 0.080″ thick, 36 volume fraction of fibers. Actual construction consisted of 16 columns per inch in warp and 15 pick columns per inch in fill. Measured thickness was 0.095″ as woven. Calculated fiber architecture was 48% @ 0 degree, 33% @ 90 degree, and 19% z-fiber @ ±60 degree. Calculated fiber volume was 36.7%.

The thicker 3-D weave utilized nine warp layers, 10 fill layers, and float warp weavers that passed through the entire thickness and then over two fill tows. The target thickness was 0.145″, 36 volume fraction of fibers. Actual construction consisted of 16 columns per inch in warp and 14.7 pick columns per inch in fill. Measured thickness was 0.150″ as woven. Calculated fiber architecture was 36% @ 0 degree, 39% @ 90 degree, and 25% z-fiber @ ±68 degree. Calculated fiber volume was 36.1%.

A photograph of one of the nine-ply 3-D fiber preforms is shown in Figure 2.

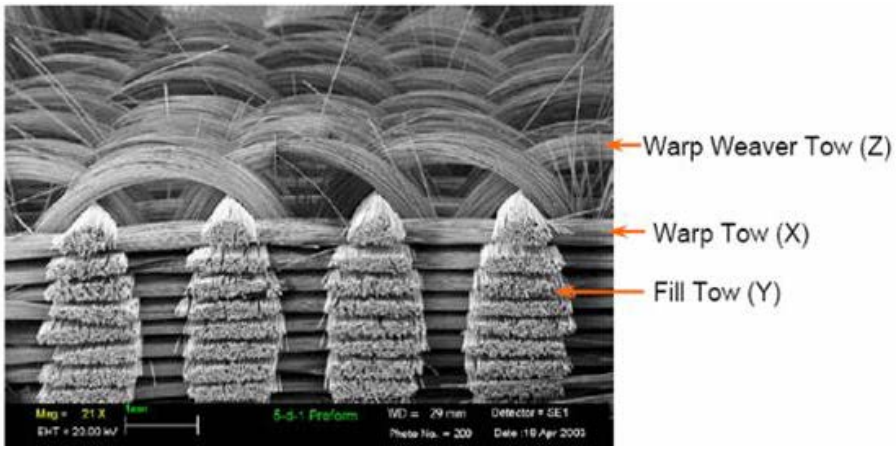


**Figure 2. SEM Image of Nine-Ply 3-D Fiber Preform.**
**Image Clearly Shows Warp, Fill, and Warp Weaver Tows**

**3.1.7 Acceptance Criteria.** As part of the purchase agreement, COIC agreed to meet certain requirements, one of which was that the as-manufactured 2-D S200 material would exhibit a room-temperature (RT) tensile strength of >170 MPa. However, the 3-D materials are developmental. Therefore, no strength requirement was required and production would be on a best-effort basis.

## 3.2 Panels and Test Specimens

A total of five different configurations were investigated: 0.080″ 2-D S200, 0.080″ 3-D S200, 0.145″ 3-D S200, 0.080″ 3-D Starfire, and 0.145″ 3-D Starfire. The 2-D material was manufactured as two 6″ × 6″ panels, while the 3-D panels were manufactured as four 6″ × 12″. panels. A machining drawing for the 2-D material is shown in Figure 3 and for the 3-D panels in Figure 4.

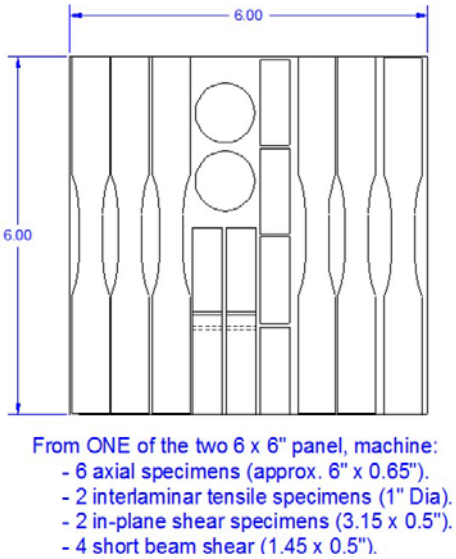


**Figure 3. Diagram of S200 2-D Panel and Location of Test Specimens**

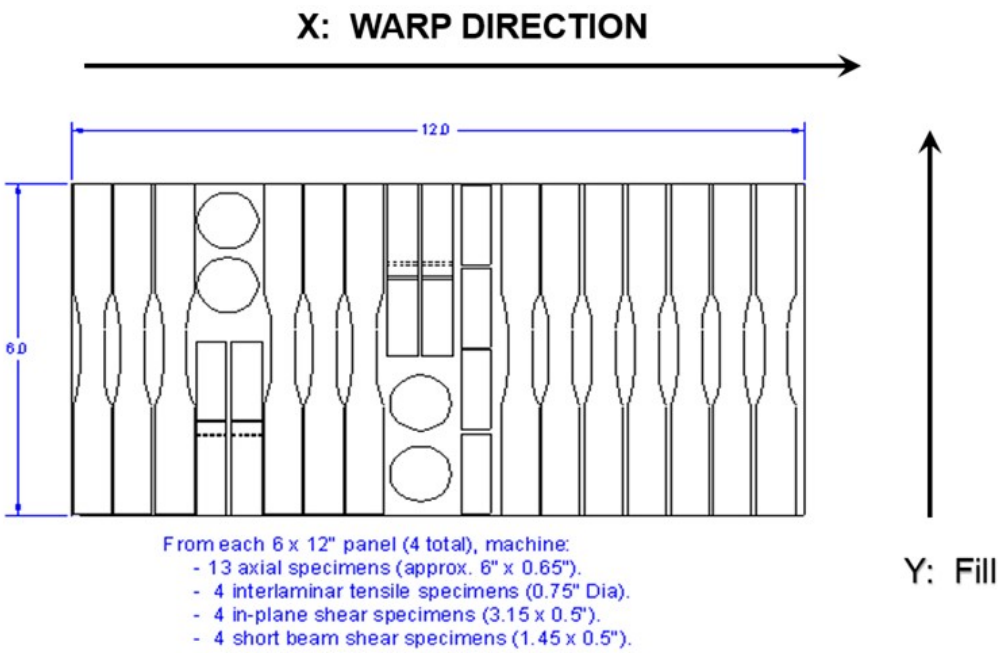


**Figure 4. Diagram of 3-D SiC/SiNC Panels and Location of Test Specimens**

### 3.3 Test Plan

The following sections describe the mechanical testing and material characterization. The primary focus of this investigation was to determine how transitioning from a 2-D SiC/SiNC to a 3-D SiC/SiNC material would affect strength and high-temperature durability. Several types of tests (tension test, creep-rupture, fatigue, and measurement of residual tensile for run-out conditions) were conducted on the 2-D and 3-D material systems at 1000°C and up to 360,000 seconds (100 hours) to generate durability data. . Data for the 2-D material system was used to create a baseline and the data collected from the 3-D material systems were then compared to the 2-D system. In addition, several specimens used in these tests were sectioned to evaluate the microstructure of both the 2-D and 3-D material systems.

**3.3.1 Baseline Tensile Properties.** In-plane tension tests were used to document the baseline properties such as modulus of elasticity (E), ultimate tensile strength (UTS), proportional limit (PL), and strain at failure ($\varepsilon_f$). A schematic of the tensile test specimen is shown in Figure 5. This specimen was used for all tension, creep rupture, and fatigue tests.

Tensile tests provide important information on the stress-strain behavior. The traces are used to identify both the initial linear-elastic behavior region as well as the non-linear damage-induced region. It is important to document the initial onset on non-linear behavior, as it identifies the onset of macro-damage in the CMC. This non-linear behavior develops as a result of a cumulative damage process that involves multiple damage mechanisms occurring at the same time. These damage mechanisms can include matrix cracking, fiber-matrix debonding, oxidation of constituents in the CMC, crack growth, viscoelastic deformation, delamination, etc. These tests were conducted according to the methods outlined in American Society for Testing and Materials (ASTM) Standards C1275 [3] and C1359 [4] for room- and elevated-temperature, respectively. All tension tests

were performed at 1000°C using a constant force rate of 25 MPa/s. The tension tests were critical for determining the onset of non-linear behavior identified as the Proportional Limit (PL), and the PL was used as a starting stress level for the creep and fatigue testing.

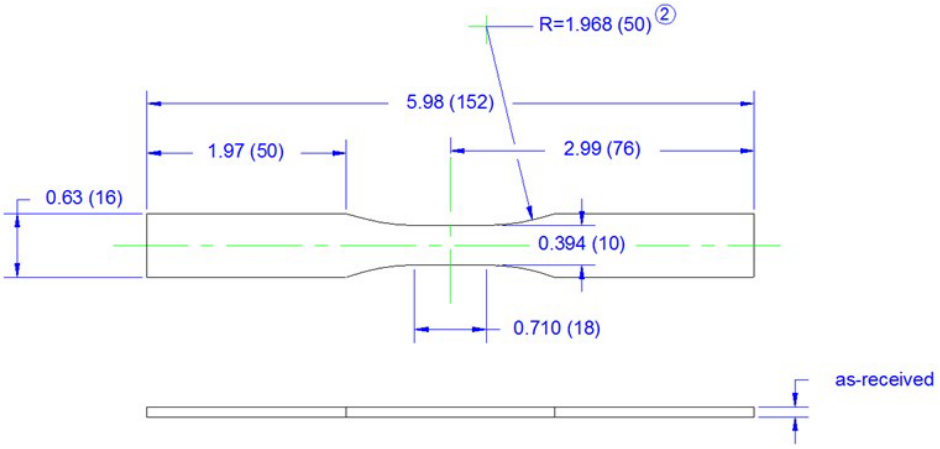


**Figure 5. Schematic of Dogbone Specimen Used for All Tension, Creep, and Fatigue Testing**

**3.3.2 Fatigue Testing.** Data from the tension tests was used to guide the selection of an appropriate initial stress level for conducting the fatigue tests. These tests were conducted according to the methods outlined in ASTM C1360-96 [5] for fatigue testing of CMCs. The objective of the fatigue testing was to determine the highest stress that could reach run-out. The initial starting stress level was selected to be approximately 10% below the PL. If the first specimen failed, the stress would be dropped 10 MPa and, if the specimen ran out, the next test would be conducted at a stress level 10 MPa higher. The fatigue testing was used to determine if this SiC/SiNC (S200) CMC experiences cyclic damage and fatigue crack growth. Tests were conducted at a load ratio of 0.1 (min/max load) and a frequency of 1 Hz. Run-out was determined to be 360,000 seconds (100 hours). Any specimens that ran out were cooled to RT and tension tested to determine the retained strength. Any changes in the tensile stress-strain response would indicate that damage had been introduced into the test specimen. Testing was conducted in accordance with ASTM C1360 for fatigue testing of CMCs.

**3.3.3 Creep Rupture Testing.** The initial starting stress levels were based on the highest stress level to reach run-out during fatigue testing. This type of testing is important, as it is used to identify time-dependent behavior.

Creep rupture testing was performed following ASTM C1337. Specimens were first heated to temperature and held for 15 minutes. Load was then applied at a rate of 25 MPa/s up to the desired stress value. Strain was recorded during both the ramp-up to the desired stress value and during the creep tests. Time to failure was recorded as a function of applied stress. Plots of creep strain versus time and total strain versus time were generated from the test data. Test time to reach a run-out condition was selected to be 360,000 seconds (100 hours). Any specimens that ran out were cooled to RT and tension tested to determine the retained strength.

**3.3.4 Interlaminar Shear: Double-Notch Compression (DNC).** Interlaminar shear tests were accomplished using two procedures. Shear strength testing was performed at RT on the DNC samples following procedures outlined in ASTM C1292. A schematic of the DNC test specimen is shown in Figure 6. A slightly longer sample than that described in the cited test method was used to accommodate the available anti-buckling guide. A displacement rate of 1 mm/min was used in all tests, which corresponded to a nominal shear stress rate of 100 MPa/min.

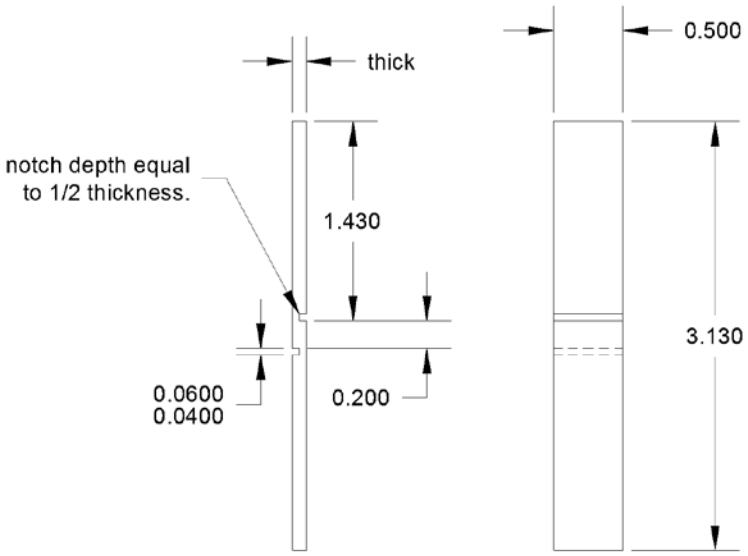


**Figure 6. Double-Notch Compression Test Specimen Geometry**

**3.3.5 Interlaminar Shear: Short-Beam Shear.** Interlaminar shear testing at RT and 1000°C was also performed using the short-beam-shear method described in ASTM D2344. A drawing of the test specimen is shown in Figure 7. A fully articulating three-point flexural fixture, fabricated from SiC, was placed in the center of a large resistance furnace. An optical photograph of the fixture is shown in Figure 8. A span-to-depth ratio of 4:1 was used for all tests, based on gross sample thickness (gross thickness discussed in later sections).

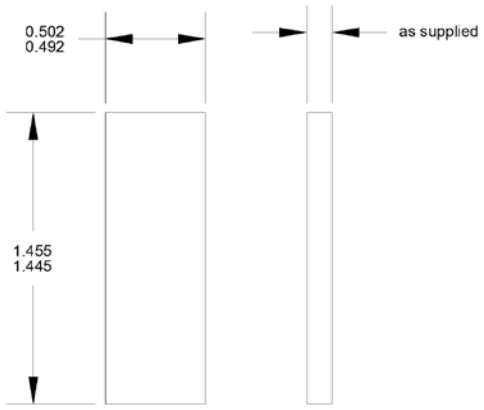


**Figure 7. Short-Beam Shear Test Specimen Geometry**

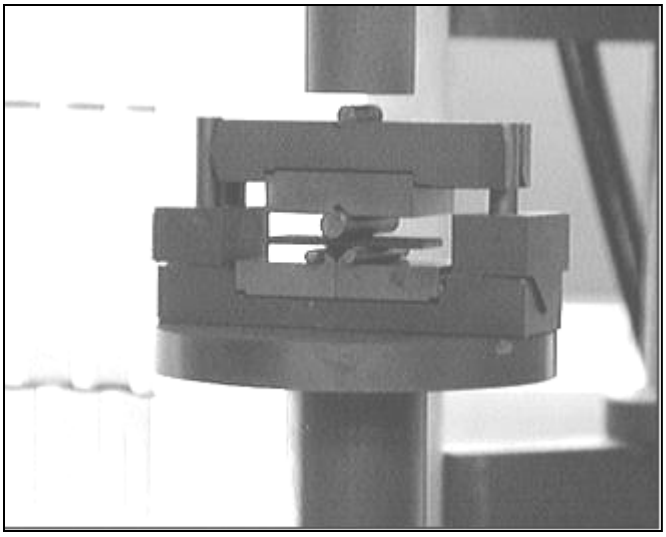

**Figure 8. Short-Beam Shear Test Fixture**

Interlaminar shear stress was estimated from the following equation:

$$\tau = \frac{3}{4}\left(\frac{P}{w * t_{net}}\right) \quad (1)$$

where $P$ is the applied force, $w$ is sample width, and $t_{net}$ is the net sample thickness.

**3.3.6 Porosity Measurements.** To fully assess the mechanical behavior of the 2-D and 3-D systems, it was important to quantify the porosity in each CMC. Porosity was measured using the Archimedes' Method of Density Measurement and the AutoPore III Mercury Porsimeter analysis technique.

**3.3.6.1** ***Archimedes' Method of Density Measurement.*** This method yields the percentage of open porosity within the specimen. ASTM B962-15 was used to calculate density and porosity. The procedure followed for the samples was:

A. Boil for 40 minutes in distilled water for degassing purposes.

B. Immerse in the water to fill out any pores (immersed weight = w1).

C. Remove and gently tap to remove the water from the top and bottom surfaces, and measure the weight (= w2).

D. Dry in an oven for 1 hour and note the weight (= w3).

E. Make the following calculation:

Exterior volume of samples, V = (w3-w1)/density of water (~1.0 g/cc)

Bulk or Archimedes density = (w3)/V

Volume of pores, vp = (w2-w3)/density of water

Apparent porosity (%) = vp/V

Relative density (%) = Bulk density/theoretical density

**3.3.6.2** ***AutoPore III Mercury Porosimeter Analysis.*** Pore-size distribution can be determined using mercury porosimetry. A material's porosity is determined by applying increasing levels of pressure to a sample immersed in liquid mercury. The pressure required to force mercury into a pore, or void, is inversely proportional to the size of the pore opening.

To perform the analysis, a sample is loaded into a penetrometer, which consists of a sample cup connected to a metal-clad, glass capillary stem. The penetrometer is sealed and placed in a low-pressure port where the sample is evacuated to remove air and moisture. The penetrometer is then backfilled with mercury, which occupies the available volume of the sample cup and fills the capillary in the penetrometer stem. Pressure is incrementally increased, which forces the mercury into voids found on or near the surface of the sample.

As mercury moves from the capillary stem into the sample cup, a decrease in electrical capacitance is observed between the external metal cladding and the internal core of mercury in the penetrometer stem. This change in capacitance is directly related to the change of mercury volume remaining in the capillary stem. These pressure (pore-size) and change-of-capacitance (total void volume) values are recorded and used to calculate a variety of parameters.

Some of the most commonly used parameters that are calculated and reported include total pore volume, bulk density, skeletal density, percent porosity, and median pore diameters. Many other graphical options are available to visually display the pore-size and pore-volume relationships.

A major advantage of this technique is the abundance of information provided. Another advantage is the ability to measure a broad range of pore sizes (as large as 900 microns and as small as 0.003 microns). The disadvantage is the handling of liquid mercury. Moreover, results can sometimes be difficult to interpret properly.

## 3.4 Test Equipment Description

**3.4.1 Test System: SH#12.** Room- and elevated-temperature tests were performed using a horizontal MTS servo-hydraulic test system. A photograph of the test system is shown in Figure 9 and Figure 10. This test frame is uniquely orientated in the horizontal configuration and is equipped with MTS 647 hydraulic grips, a MTS 609 alignment device, a 5.5-kip (25kN) MTS load cell, and a MTS 458 analog MicroConsole signal controller. This test frame was designed and built in the horizontal configuration specifically for characterization of the high-temperature mechanical properties of CMCs, which demonstrate less than 1% strain to failure. Furnaces that operate in the vertical position experience "chimney" effects where the hot air rises and cooler air is drawn in from the bottom of the furnace. This can make it difficult to generate a uniform temperature profile along the gage section of the test specimen (as the lower end of the gage section is always cooler than the top end), though multiple heating zones and strategic placement of insulation can somewhat mitigate this effect. In contrast, furnaces operated with the specimen in the horizontal orientation produce a very symmetric and uniform temperature profile across the gage section. In addition, the high-temperature extensometer mounting design requires substantially less spring force to keep it in contact with the test specimen compared to when it is mounted in the vertical configuration. The grips, furnace, and extensometer were surrounded by a sealed metal box to limit air currents, as shown in Figure 11.

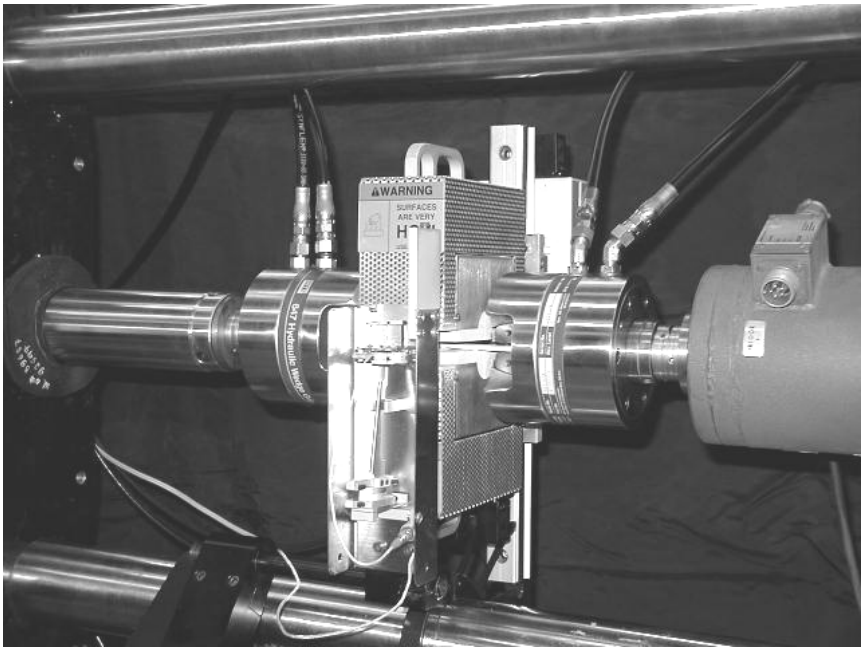


**Figure 9. Photograph of Horizontal Servo-Hydraulic Test System Used for Room- and Elevated-Temperature Testing**

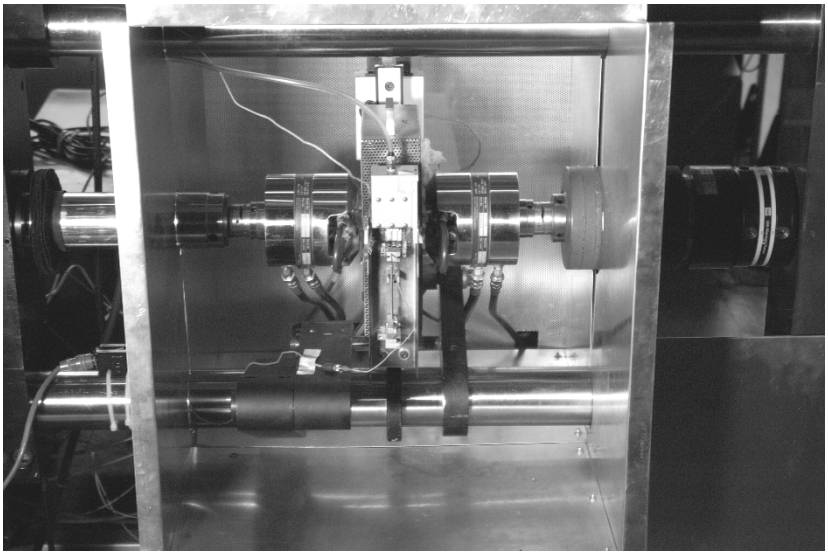

**Figure 10. This Photograph Highlights Wedge grips, Furnace, and Insulating Box Used to Minimize Noise in Strain Measurements**

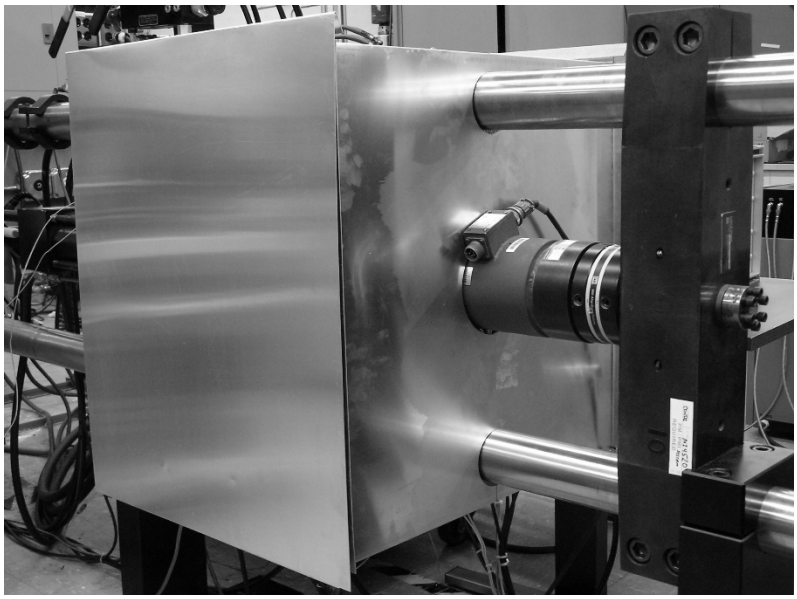

**Figure 11. Enclosure Used to Minimize Noise in Extensometer Resulting from Air Currents in Laboratory**

**3.4.2 Shear Testing.** Shear testing was performed on a screw-driven vertical machine.

**3.4.3 Verification of Alignment for Servo-Hydraulic Test Frame.** The grip/load train alignment was verified using a highly ground, hard steel, straight-sided specimen instrumented with eight strain gages, as shown in Figure 12. The goal for alignment was to be within ASTM E1012-99 [9] specifications of less than 5% bending at 500 με displacement in all four specimen orientations. A plot of percent bending versus axial load is shown in Figure 13. Often, the percent bending at this ASTM specification was about only 2%.

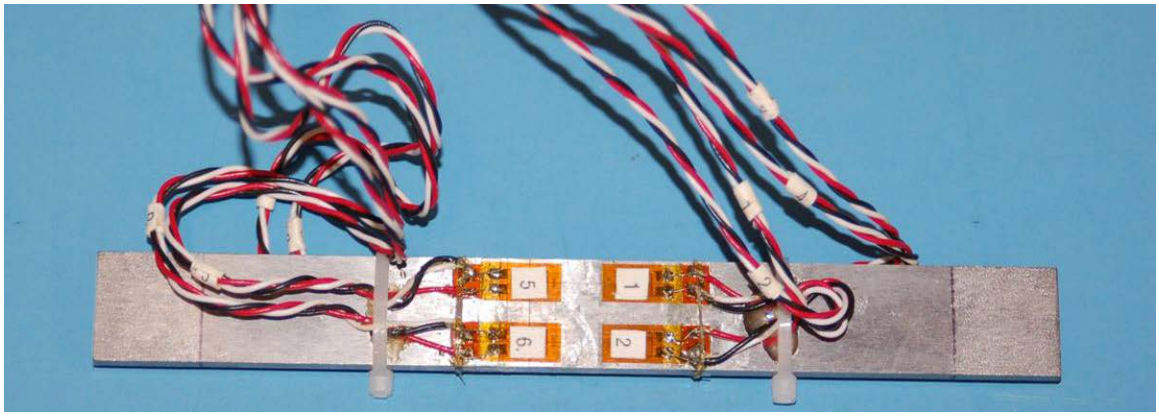


**Figure 12. Strain-Gaged Steel Alignment Specimen Used to Verify Alignment**

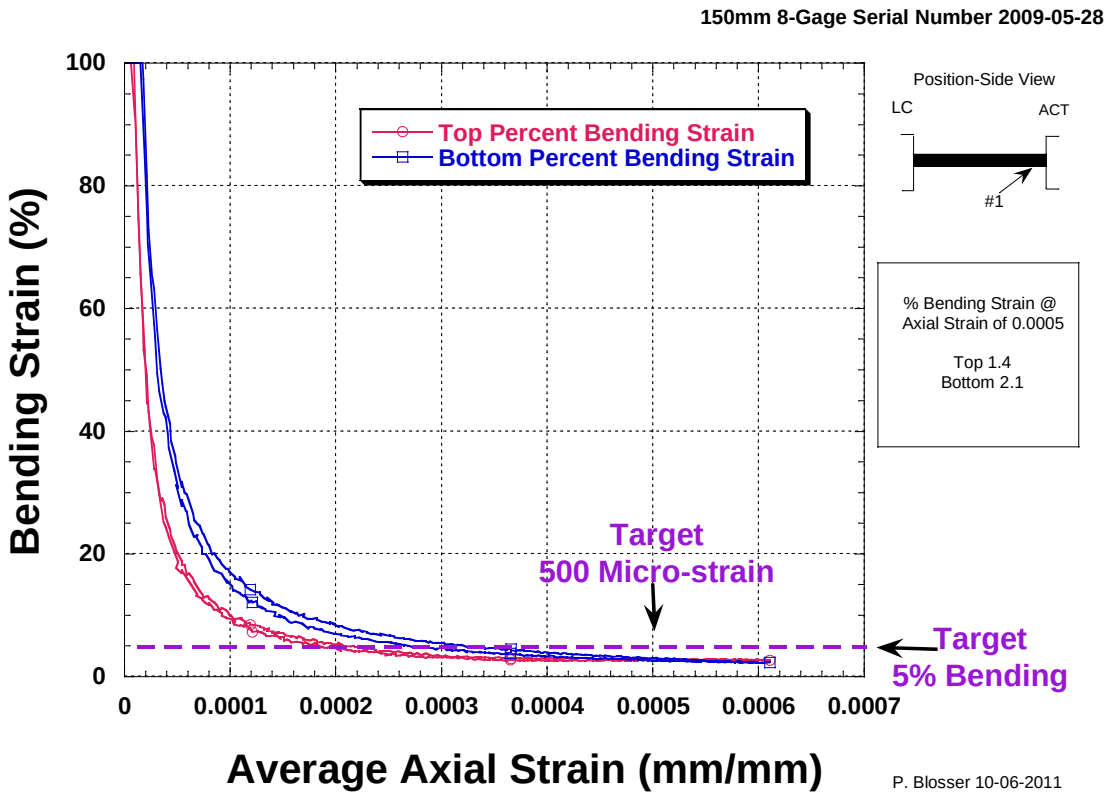


**Figure 13. Plot of Bending Strain Versus Average Axial Strain for Alignment Check of SH#12**

**3.4.4** ***Verification of Furnace Thermal Profile.*** Elevated-temperature testing was conducted using a commercially available three-zone furnace made by Amteco, Inc. This split-design furnace uses three silicon-carbide heating elements in each furnace half which are similar to the ignitor elements used in house furnaces. There are three S-type control thermocouples within the furnace cavity, allowing for three zones of temperature control. Insulation with specimen and instrumentation cut-outs was placed between the two furnace halves to help preserve the integrity of the furnace cavities and keep the furnace well-sealed. Having the furnace in a horizontal position allowed for the use of these easily replaced insulation cut-outs.

Prior to starting this testing program, the furnace temperature set points were determined for the desired specimen temperatures. For all high-temperature testing, it is very important to calibrate the furnace using an actual test specimen and not just a thermocouple probe. Therefore, one SiC/SiC test specimen was dedicated to mapping the temperature profile across the gage length and determining the corresponding furnace set-point temperatures required to operate the furnace in an automated-control mode. The test specimen was instrumented with thermocouples across the extensometer gage length, as well as outside of, the specimen gage length, as depicted schematically in Figure 14. The exact locations of the thermocouples relative to the center of the specimen were 0 mm, -7 mm, +7 mm, -14 mm, and +22 mm. Great care was taken to locate the

thermocouples on the temperature calibration specimen such that there was no twist to the thermocouple wires. The TC were attached to the calibration specimen with "B"-type wire ties and cemented in place with a ceramic adhesive. Photographs of a specimen set for temperature profile measurement are shown in Figure 15 and Figure 16. The furnace set points were adjusted to achieve temperatures across the extensometer gage length that were within 1% of the target temperature. Figure 17 is an example plot of temperature versus location along a CMC test specimen. Plotted in the figure are the actual temperatures of the test specimen and the temperature of each of the three zones in the furnace. The data shows that one cannot simply use the thermocouples located inside this type of furnace to accurately measure temperature on the specimen. Documentation of the furnace set points allowed for automatic control of the furnace temperature using the furnace thermocouples rather than having to mount thermocouples to the CMC test specimen. This eliminated any chance of having an adverse reaction between the thermocouple or bonding material and the CMC test specimen. This same procedure was used for the S200 CMCs.

Strain was measured using either a 12.7-mm gage length MTS high-resolution Model 632.26B-40 clip-on extensometer calibrated at 0.089 mm per 10 volts for RT testing or a 15-mm gage length MTS 632.50B-04 high-temperature alumina rod extensometer calibrated at 0.1278 mm per 10 volts. Strategically placed insulation around the furnace and extensometer rods was required to minimize effects of the thermal radiation that cause distortion in the rods and produces noise in the strain signal. A low-pressure air stream was passed through a diffuser and pointed at the body of the extensometer during high-temperature measurements to create a constant environment around the extensometer body.

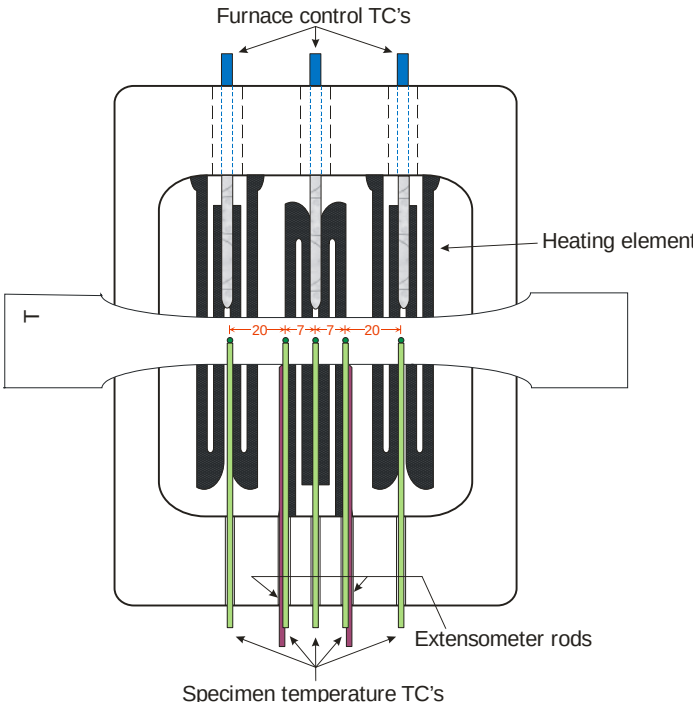


**Figure 14. Schematic Showing Placement of Thermocouples for Furnace Temperature Mapping**

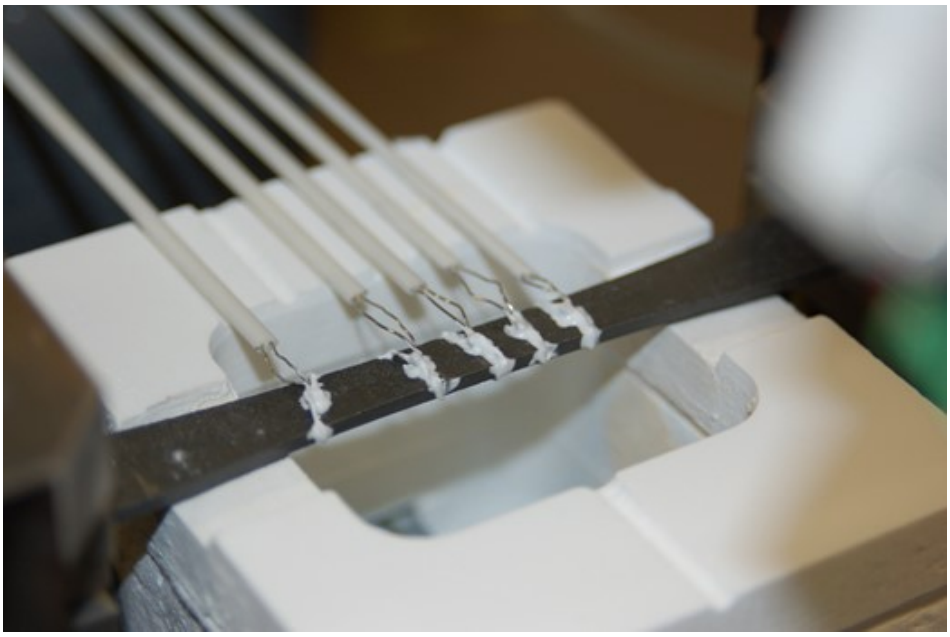

**Figure 15. Example ofCMC Test Specimen Instrumented with Thermocouples for Furnace Temperature Mapping**

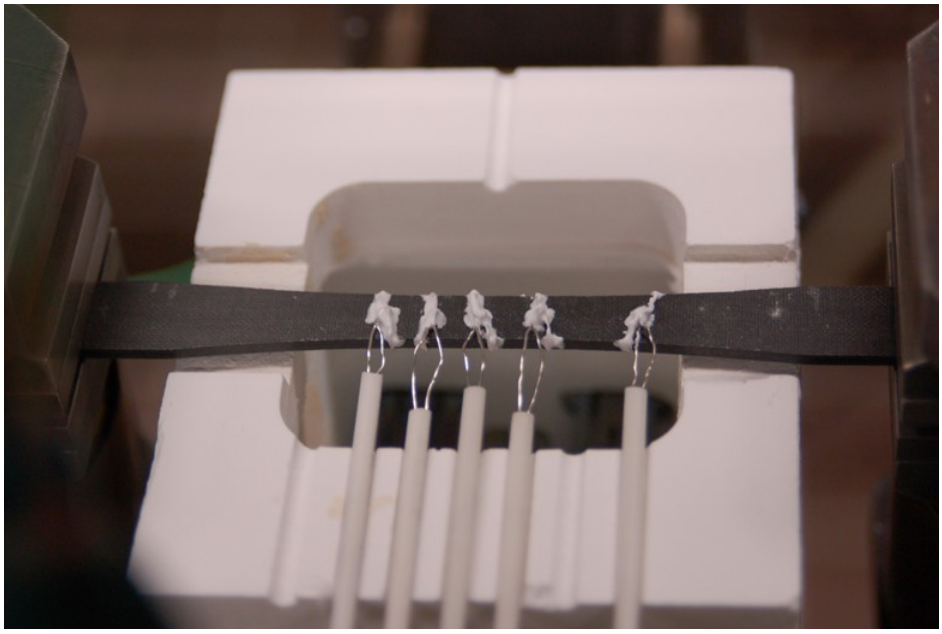

**Figure 16. Example of CMC Test Specimen Instrumented with Thermocouples for Furnace Temperature Mapping**

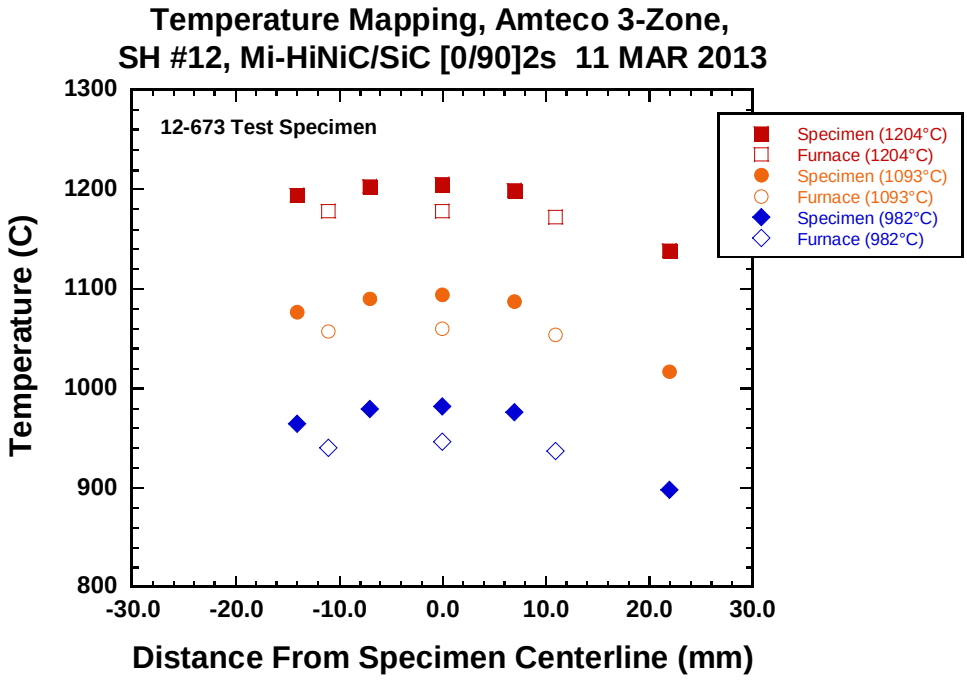


**Figure 17. Temperature Profile Conducted on General Electric (GE) Gen 1.1 Mi-HiNiC/SiC Test Specimen**

## 3.5 Material Characterization

**3.5.1 Cutting of Specimens For Microscopy.** There was no extra material supplied with the test specimens. Therefore, tested specimens were sectioned for ceramography. For each material system, a tested tensile specimen was selected and sectioned on a diamond saw normal and parallel to the warp direction, and 45° to the warp direction. A schematic of a dogbone test specimen and the location of the sectioning cuts is shown in Figure 18. Specimens were cut on a slow-speed diamond saw using saw blades embedded with a low concentration of diamond. A saw speed of approximately 30 RPM with kerosene as a cooling and lubricating fluid was used. Very little weight was used on the saw arm to reduce damage to the matrix material and reduce the size of the burr that typically remains as the saw completes the sectioning. If a small burr remained, it was removed by lightly holding the burr against the side of the saw blade. Great care was taken to make sure no burrs remained on the cut surface, as they will cause a large amount of mounting material to flow between the specimen surface and the mounting press during the mounting process. If this happens, the specimen will polish unevenly, requiring a great deal more time or going to much coarser-grit polishing media.

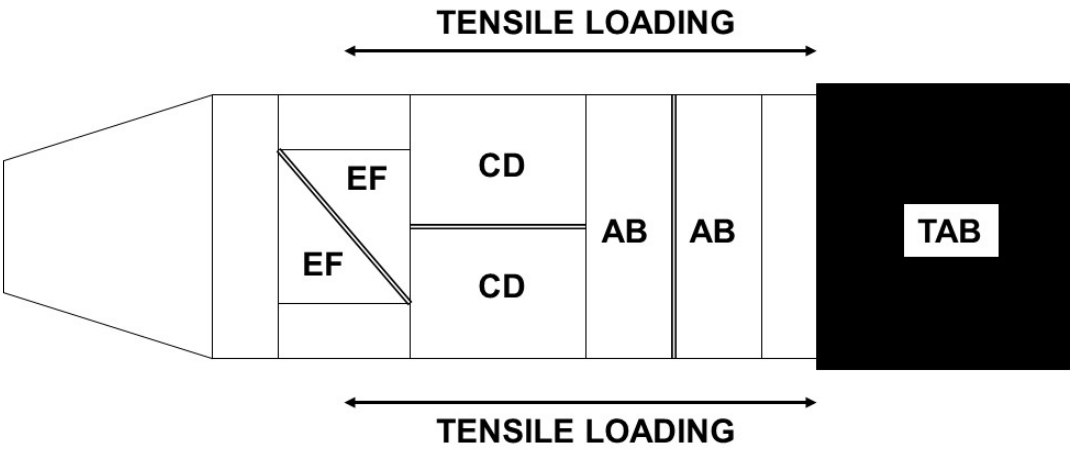


**Figure 18. Schematic Showing Actual Test Specimens Sectioned for Microstructural Studies. Double Lines Indicate Surfaces Polished and Studied.**

**3.5.2 Mounting and Polishing of Sectioned Test Specimens.** The diamond-cut specimens were then mounted using KonductoMet® to prepare them for polishing. Both faces from each cut were placed face down on the mounting pedestal side by side 2-3 mm apart. Placing both halves in one polishing mount results in less chance of rounding the edges of the CMC during polishing and provides twice as much material to study in the microscopes. Mounts of 32 mm diameter were selected to allow for mounting the ±45° cuts. Standard pressures, temperature, and times were used.

**3.5.3 Polishing.** Mounted specimens were never exposed to sanding paper or coarse polishing media since the great care exercised during cutting allowed them to be taken directly to intermediate and final polishing. This was performed on a Phoenix 4000 automatic polisher that could accommodate 10 mounted specimens at a time. Complimentary rotation was employed at a speed of 150 RPM and pressure was minimal, at approximately 0.5 lbs. The polishing cloth was perforated TexMet P® and the media was diamond paste dispersed and suspended in solution with a Hyprez® lubricating fluid. Specimens were run at 20-minute intervals, and then cleaned and inspected. Polishing grits were 15 micron, 6 micron, and 1 micron. Approximately 2 hours were spent polishing with each grit size.

After polishing with each grit size, the entire fixture holding the 10 mounts was immersed in a soapy bath and placed in an ultrasonic cleaner for 20 minutes to remove any remaining polishing media. After the final grit of 1 micron, each mount was removed from the Phoenix fixture and cleaned individually with a soapy bath and then an acetone bath in an ultrasonic cleaner to remove any remaining organic material. The cleaned specimens were then stored in a chamber under low vacuum until investigated in the SEM.

## 4.0 RESULTS

### 4.1. Microstructural Analysis

The unique weave of the 3-D materials resulted in very rough surfaces. The research team decided that using the as-measured thickness for each 3-D system would result in significant errors in UTS, modulus, and PL values. There were two reasons for this determination. The first was that the through-thickness weaving fiber tows generate large loops at the surface of the preforms (as shown earlier in Figure 2) while the warp and fill fibers were essentially straight. Between the loops were large regions that were either completely empty, partially full of matrix, or completely full of matrix. In all cases, those regions had large cracks. The same was observed inside the loops, with some completely void of matrix. The second reason was that this matrix-rich region represented a different percentage of the cross-section for the thin and thick preforms which would override any other difference one might observe in the strengths between the various 3-D materials. It was felt that it was more important to determine the thickness using the warp and fill fibers to allow a better comparison between the 3-D nine-warp layer preform and the 3-D four-warp layer preform.

Figure 19 schematically illustrates the difference between the original thickness (gross thickness) and the actual thickness (net thickness) for a 3-D 80-mil fiber preform, while Figure 20 is an actual microstructural cross-section. Table 1 presents the measured net section thickness values from polished cross-sections of actual specimens and Table 2 compares the average total thickness for each 3-D material to the average net thickness values. The actual thickness of each 3-D CMC is substantially larger than the net section thickness. For the 80-mil 3-D panels, there was almost a 50% difference between the two thickness measurements. These net thickness values were used to calculate stress values for all specimens.

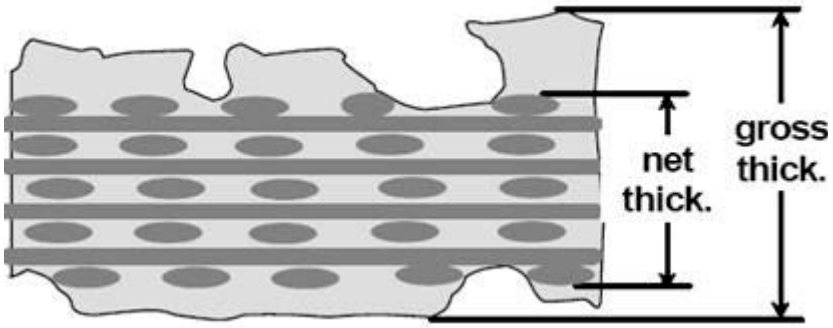


**Figure 19. Method Used to Calculate Net Cross-Sectional Area**

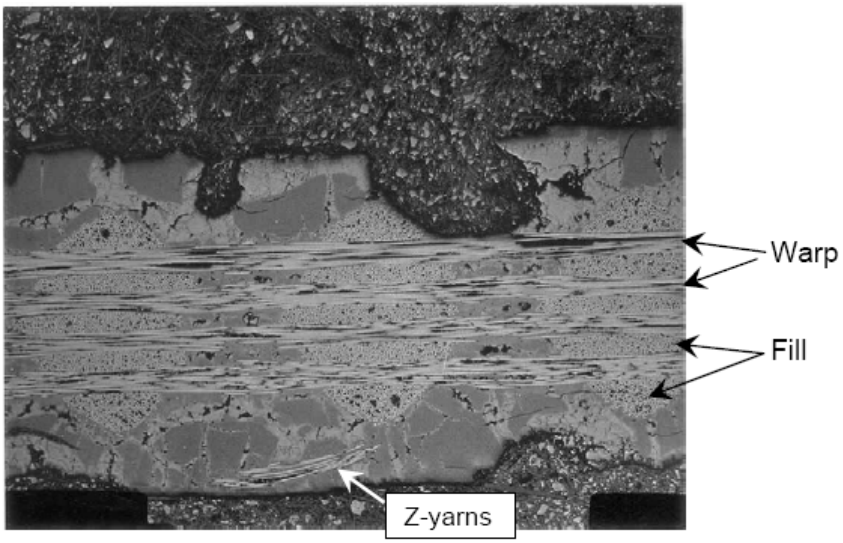


**Figure 20. Optical Micrograph of 3-D S200 80-mil CMC Showing How Z-Weaving Fibers Contribute to Almost Doubling Thickness**

**Table 1. Actual Net Thickness Measurements Made on Polished Cross-Sections of Test Specimens**

| Specmen Number | CMC Material Description | Mount 1 (mm) | | | Mount 2 (mm) | | |
|---|---|---|---|---|---|---|---|
| | | LS | M | RS | LS | M | RS |
| 3S280-5 AB | 3D, S200, 80 mil | 1.49 | 1.47 | 1.40 | N/A | N/A | N/A |
| 3S280-5 CD | 3D, S200, 80 mil | 1.45 | 1.22 | 1.13 | 1.22 | 1.25 | N/A |
| 3S280-5 EF | 3D, S200, 80 mil | 1.43 | 1.43 | 1.48 | 1.47 | 1.47 | N/A |
| | | | | | | | |
| 3S2145-1 AB | 3D, S200, 145 mil | 2.75 | 2.79 | 2.71 | 2.94 | 2.82 | 2.85 |
| 3S2145-1 CD | 3D, S200, 145 mil | 2.79 | 2.89 | 2.52 | N/A | N/A | N/A |
| 3S2145-1 EF | 3D, S200, 145 mil | 2.79 | 2.76 | 2.76 | 2.83 | 2.66 | 2.71 |
| | | | | | | | |
| 3ST80-1 AB | 3D, Starfire, 80 mil | 1.43 | 1.49 | 1.48 | 1.48 | N/A | N/A |
| 3ST80-1 CD | 3D, Starfire, 80 mil | 1.51 | 1.36 | 1.32 | 1.27 | 1.22 | 1.15 |
| 3ST80-1 EF | 3D, Starfire, 80 mil | 1.46 | 1.45 | 1.49 | 1.49 | 1.47 | 1.46 |
| | | | | | | | |
| 3ST145-18 AB | 3D, Starfire, 145 mil | 2.80 | 2.88 | 2.90 | 2.95 | 2.90 | 2.85 |
| 3ST145-18 CD | 3D, Starfire, 145 mil | 2.87 | 2.90 | 2.41 | 2.63 | 2.37 | 2.34 |
| 3ST145-18 EF | 3D, Starfire, 145 mil | 2.80 | 2.80 | 2.78 | N/A | N/A | N/A |

**Table 2. Average Net Thickness Values Used to Calculate Net Stress Values**

| Specimen Number | CMC Material Material | Average Total Thickness (mm) | Average Net Thickness (mm) |
|---|---|---|---|
| 3S280-5 | 3D, S200, 80 mil | 2.44 | 1.38 |
| 3S2145-1 | 3D, S200, 145 mil | 3.94 | 2.77 |
| 3ST80-1 | 3D, Starfire, 80 mil | 2.57 | 1.41 |
| 3ST145-18 | 3D, Starfire, 145 mil | 3.94 | 2.75 |

Figure 21 illustrates the difference in the UTS due to the difference in the specimen thickness. For specimen 3s280-11 (3-D, S200-1, 80 mil), the UTS increased from 94.1 MPa to 176 MPa, which is very close to a 100% increase. This method of determining thickness and calculating net stress more accurately measures the strength of the fill fibers and allows for a more accurate comparison between the five fill-fiber perform and the 10 fill-fiber preform.

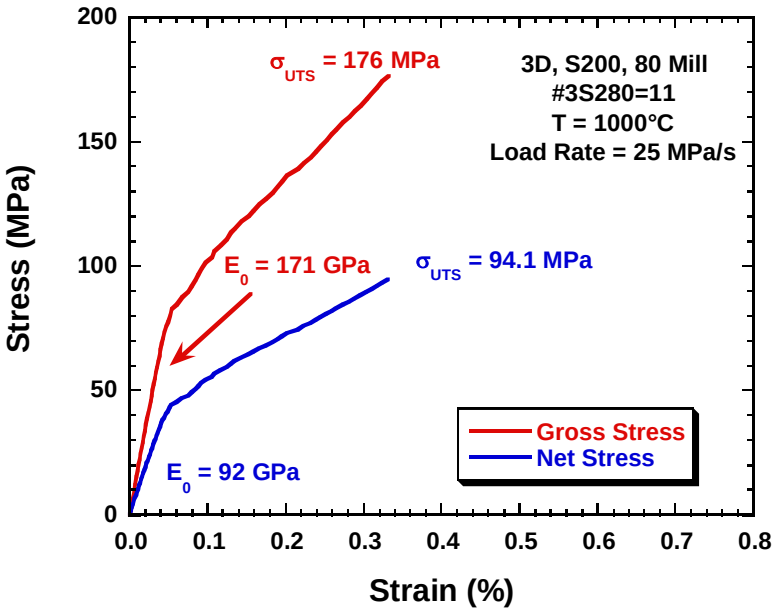


**Figure 21. Change in Stress-Versus-Strain Behavior When Comparing Net Thickness to Gross Thickness**

Figure 22 and Figure 23 are micrographs for the 2-D S200-1 material. This material system was used as the baseline to assess the performance and mechanical behavior of the 3-D material systems. There was little to no matrix-rich regions on the surface of the 2-D material, so no adjustments to the thickness were required. The composite was reasonably uniform, with the occasional large stringer-type pore observed in Figure 22.

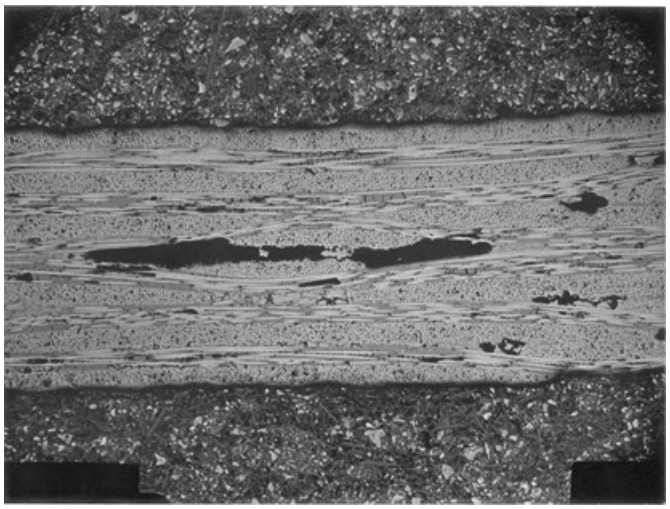

**Figure 22. 2-D S200-1 @ 25×, AB**

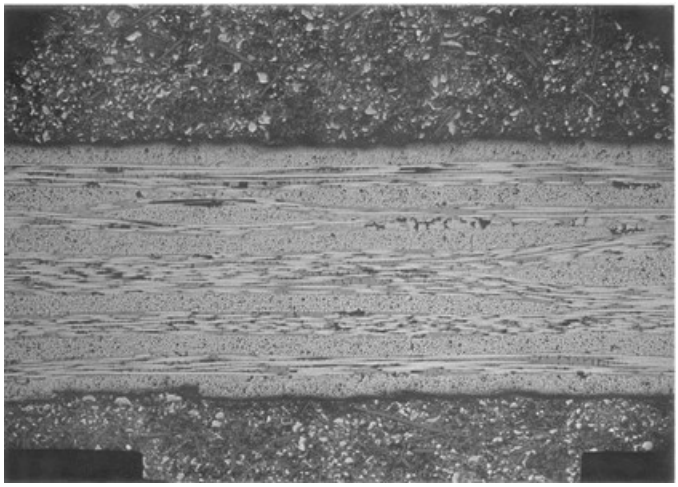

**Figure 23. 2-D S200-1 @ 25×, A**

A micrograph of the 3-D S200 80-mil CMC is shown in Figure 24, where one can clearly see that, in some areas, there is no matrix above or below the four warp fibers. This substantiates the decision to only use the net thickness to calculate stress values. The preform was to be approximately 2.03 mm (80 mil) thick, but was calculated to be 1.38 mm (54 mil).

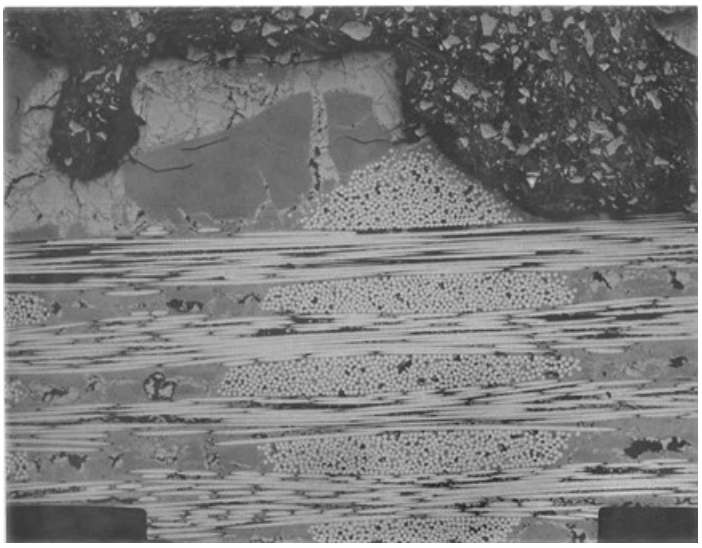

**Figure 24. 3-D S200-1, 80 mil @ 50×, AB**

Figure 25 is a micrograph of the 3-D S200-1 material system. The preform thickness was to be 3.68 mm (145 mil), but the net thickness is 2.77 mm (109 mil). In the images, one can clearly make out the looping z-weaver fiber tow and absence of any matrix above the warp fiber tows on the surface of the CMC. Figure 26 is a higher magnification showing the outermost warp fiber tow and how the z-weaver tow wraps around it.

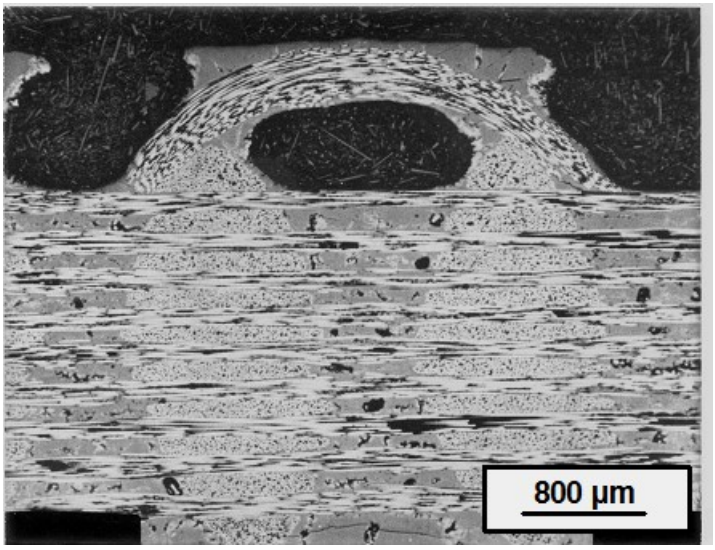


**Figure 25. 3-D S200-1, 145 mil @ 25×, AB**

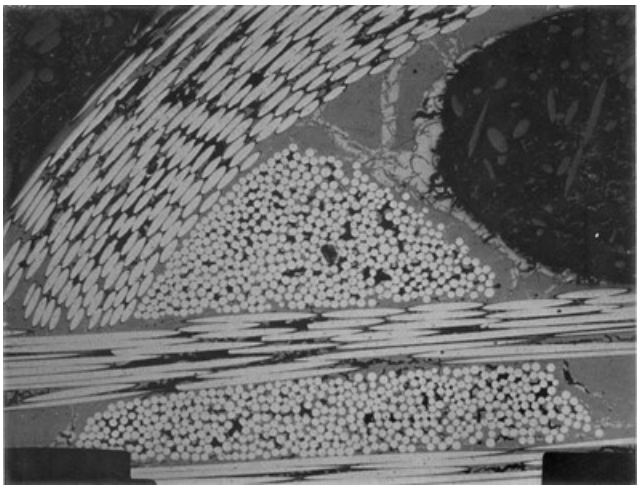

**Figure 26. 3-D S200-1, 145 mil @ 100×, AB**

Figure 27 and Figure 28 are micrographs of the 3-D Starfire material system. The preform thickness was to be 2.03 mm (80 mil), but actual thickness for this material system is 1.41 mm (55 mil).

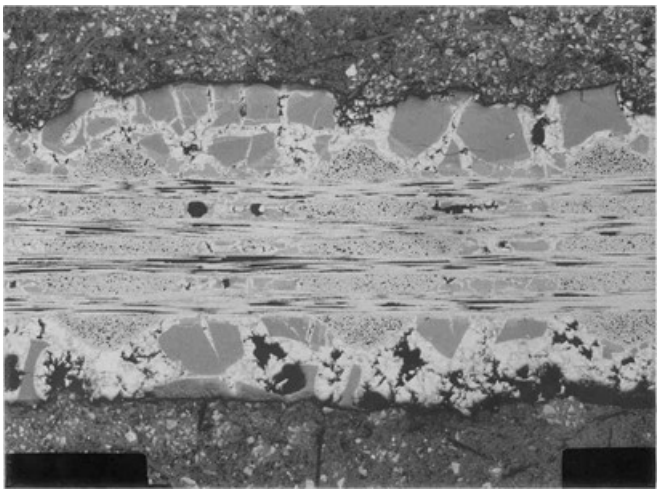

**Figure 27. 3-D Starfire, 80 mil @ 25×, AB**

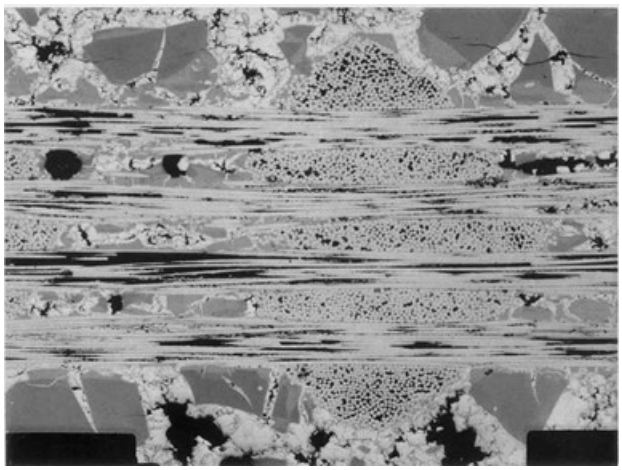

**Figure 28. 3-D Starfire, 80 mil @ 50×, AB**

Figure 29 is a micrograph of the 3-D Starfire material system. The preform thickness was to be 3.68 mm (45 mil), but the net -thickness for this material system is 2.75 mm (108 mil). Figure 30 is a higher magnification and shows that the weave pattern results in repeated matrix-rich regions and porosity between each of the warp and fill fiber tows because of the z-weaver tows.

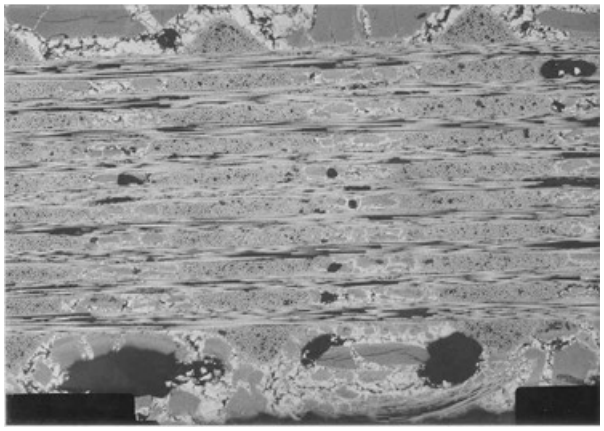

**Figure 29. 3-D Starfire, 145 mil @ 25×, AB**

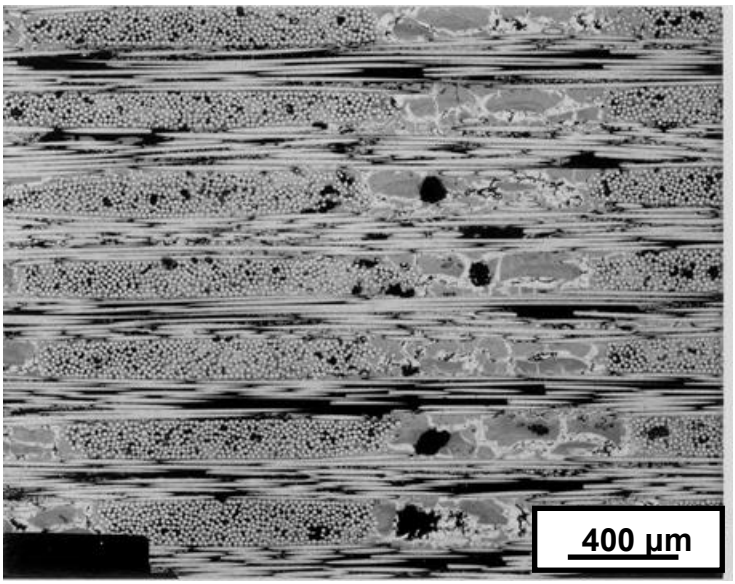


**Figure 30. 3-D Starfire, 145 mil @ 50×, AB**

## 4.2 Porosity Measurements

Porosity measurements were performed using two different techniques: Archimedes and porosimetry. Table 3 shows the average density measurements for the five CMCs, which were very similar since all used the same initial S200 matrix-filled resin for the first infiltration cycle.

**Table 3. Density Measurements Using Archimedes Method for 2-D S200 and 3-D SiC/SiNC Manufactured with S200 Resin and Starfire Resin**

| Material System Described | Sample 1 (gm/cc) | Sample 2 (gm/cc) | Sample 3 (gm/cc) | Average (gm/cc) |
|---|---|---|---|---|
| 2D, S200-1, 80 Mills, 6 Ply | 2.303 | 2.251 | 2.125 | 2.226 |
| 3D, S200, 80 mil | 2.199 | 2.222 | 2.245 | 2.222 |
| 3D, S200, 145 mil | 2.095 | 2.132 | 2.13 | 2.119 |
| 3D, Starfire, 80 mil | 2.172 | 2.177 | 2.169 | 2.172 |
| 3D, Starfire, 145 mil | 2.325 | 2.271 | 2.222 | 2.273 |

Open porosity was measured and is reported in Table 4, which is much lower in the 2-D than the 3-D material. However, the spread in values for the 3-D material makes it hard to draw any conclusions. The main takeaway is that there is, essentially, no difference between the infiltration using the S200 and Starfire SMP-10 resins. Again, this is likely attributed to using the same S200 plus resin for the first infiltration cycle.

**Table 4. Percent Open Porosity Measurements Using Archimedes Method for 2-D S200 and 3-D SiC/SiNC Manufactured with S200 Resin and Starfire Resin**

| Material System Described | Sample 1 (%) | Sample 2 (%) | Sample 3 (%) | Average (%) |
|---|---|---|---|---|
| 2D, S200-1, 80 Mills, 6 Ply | 0.000 | 0.718 | 0.525 | 0.414 |
| 3D, S200, 80 mil | 1.595 | 1.745 | 1.380 | 1.573 |
| 3D, S200, 145 mil | 2.251 | 1.526 | 2.306 | 2.027 |
| 3D, Starfire, 80 mil | 1.806 | 2.617 | 2.646 | 2.356 |
| 3D, Starfire, 145 mil | 2.078 | 0.516 | 1.875 | 1.490 |

Data from the porosimeter tests is presented in Table 5. All of the bulk density measurements are very similar, and percent porosity only ranges from a low of 5.4% to a high of only 7.5%. Thus, it appears that all of the CMCs are very similar, and suggests that performing re-infiltrations with either the S200 matrix or Starfire SMP-10 precursors did not result in any significant changes to the porosity or density. It is also worth noting that the density measurements are similar to the Archimedes measurements.

The only notable measurement is the medium pore diameter value. The 2-D S200 material has a medium pore diameter of 16.5 microns. This is significantly larger than the 3-D CMCs, which were either 6-7 microns or down under 1 micron. In addition, the 3D S200 145-mil system had the smallest medium pore size diameter of only 0.1 microns. This is very small and may play a role in the high-temperature durability.

Percent porosity is also presented graphically in the form of a bar chart in Figure 31. The only conclusion that can be made from the data is that there is significant variability in the amount and types of porosity measured between specimens of the same material, as well as between the five different SiC/SiNC systems.

**Table 5. Data from Mercury Porosimeter for 2-D S200 and 3-D SiC/SiNC Manufactured with S200 Resin and Starfire Resin**

| Property | 2D S200-1 S1 | 3D S200-1 80 mil S1 | 3D S200-1 80 mil S2 | 3D S200-1 145 mil S1 | 3D S200-1 145 mil S2 | 3D S200-1 145 mil S3 | 3D Starfire 80 mil S1 | 3D Starfire 145 mil S1 | 3D Starfire 145 mil S2 |
|---|---|---|---|---|---|---|---|---|---|
| Total Intrusion Volume (mUg) | 0.033 | 0.02 | 0.028 | 0.028 | 0.025 | 0.024 | 0.033 | 0.03 | 0.03 |
| Total Pore Area ($m_2$/g) | 10.07 | 4.016 | 5.326 | 11.395 | 9.232 | 7.608 | 2.482 | 3.688 | 2.835 |
| Median Pore Diameter: Vol (µm) | 16.453 | 6.52 | 6.92 | 0.019 | 0.043 | 0.112 | 1.551 | 0.442 | 0.569 |
| Median Pore Diameter: Area (µm) | 0.004 | 0.004 | 0.004 | 0.004 | 0.004 | 0.004 | 0.006 | 0.006 | 0.007 |
| Avg Pore Diameter: 4*V/A (µm) | 0.013 | 0.02 | 0.021 | 0.01 | 0.011 | 0.012 | 0.053 | 0.033 | 0.043 |
| Bulk Density (g/ml) | 2.27 | 2.3 | 2.263 | 2.29 | 2.299 | 2.305 | 2.295 | 2.289 | 2.3 |
| Apparent Skeletal Densitv (g/ml) | 2.452 | 2.41 | 2.413 | 2.447 | 2.442 | 2.437 | 2.483 | 2.46 | 2.471 |
| Porosity (%) | 7.411 | 4.547 | 6.217 | 6.411 | 5.848 | 5.44 | 7.547 | 6.957 | 6.93 |
| Stem Vol Used (%) | 35 | 18 | 28 | 25 | 22 | 24 | 32 | 33 | 28 |

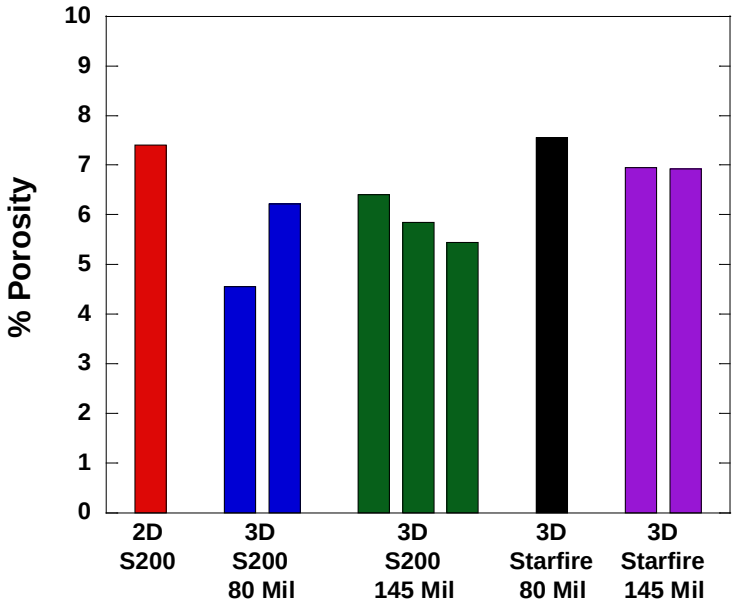


**Figure 31. Bar Chart Showing Percent Porosity for 2-D S200 and 3-D SiC/SiNC Manufactured with S200 Resin and Starfire Resin**

From the mercury porosimeter data, one can construct plots of percent intrusion versus pore size. These plots comparing the different SiC/SiNC CMCs are shown as Figures 32 through38. It appears that, for pores around 100-200 microns in size, the 2-D material had over 40% intrusion while all 3-D materials had significantly less. The four 3-D systems were all very similar. It was observed that the 2-D S200 material had the largest medium-pore diameter, which is in good agreement with the porosimeter data.

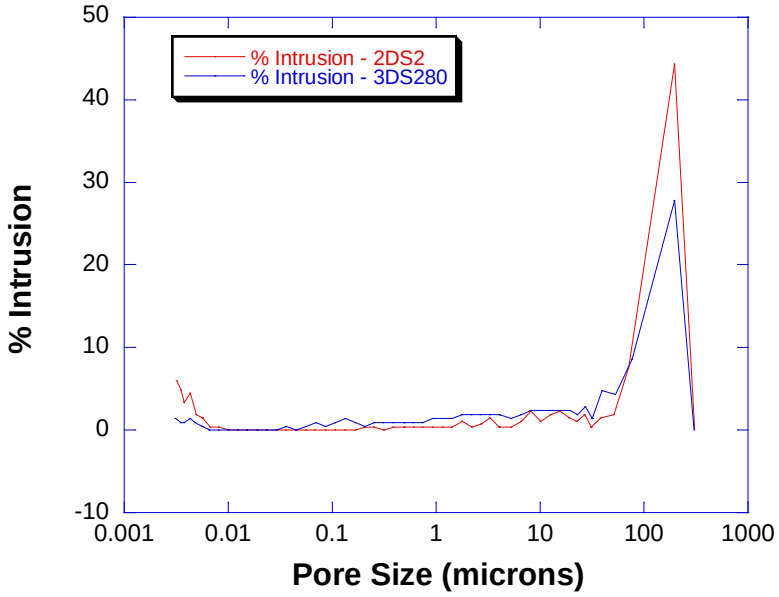


**Figure 32. Porosity Pore Size Measurements for 2-D S200 6 Ply and 3-D S200 80 Mil Using Mercury Porosimeter**

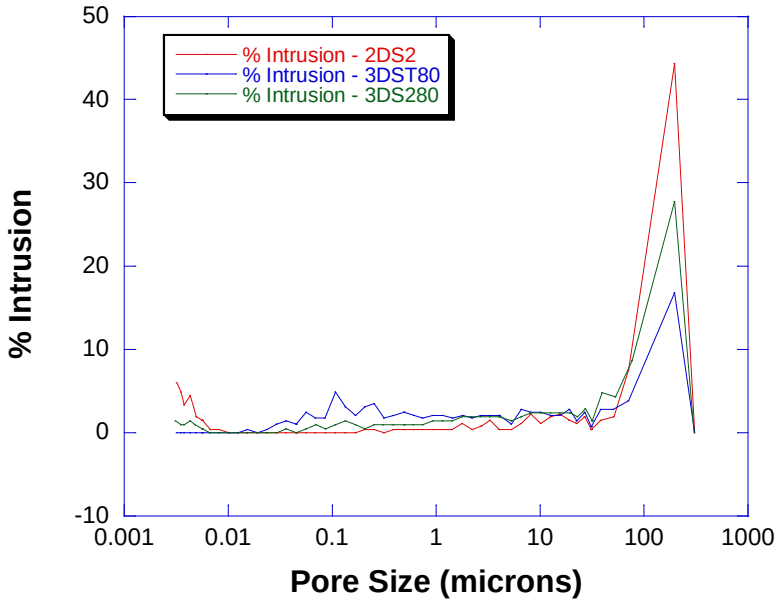


**Figure 33. Porosity Pore Size Measurements for 2-D S200 6 Ply, 3-D S200 80 Mil, and 3-D Starfire 80-Mil Using Mercury Porosimeter**

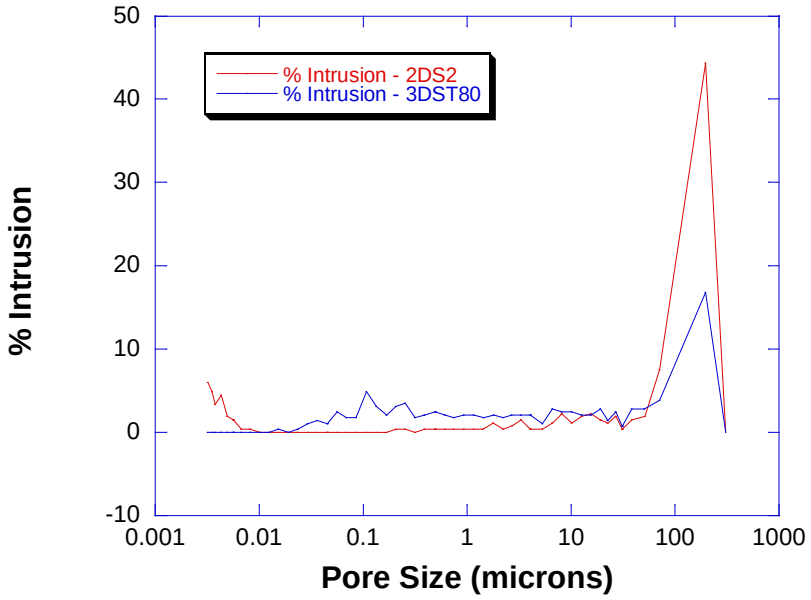


**Figure 34. Porosity Pore Size Measurements for 2-D S200 6 Ply and 3-D Starfire 80 Mil Using Mercury Porosimeter**

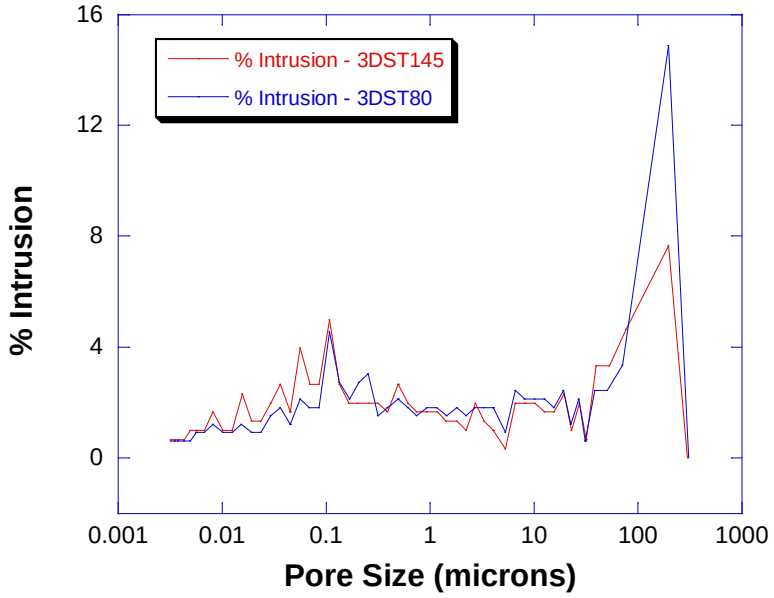


**Figure 35. Porosity Pore Size Measurements for 3-D Starfire 80 Mil and 3-D Starfire 145 Mil Using Mercury Porosimeter**

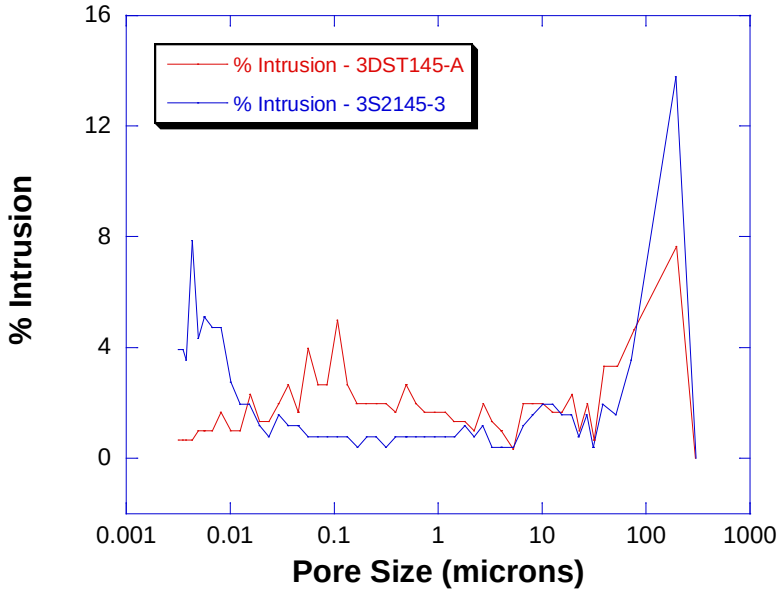


**Figure 36. Porosity Pore Size Measurements for 3-D S200 145 Mil and 3-D Starfire 145 Mil Using Mercury Porosimeter**

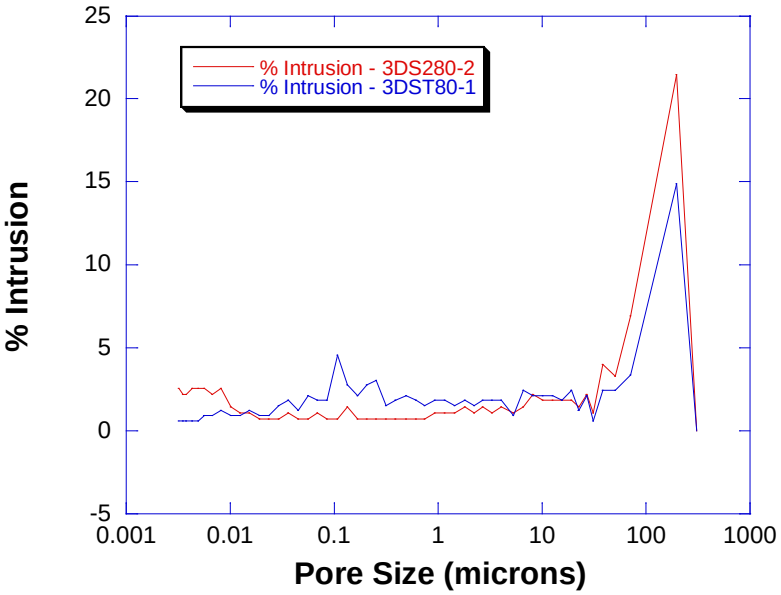


**Figure 37. Porosity Pore Size Measurements for 3-D S200 80 Mil and 3-D Starfire 80 Mil Using Mercury Porosimeter**

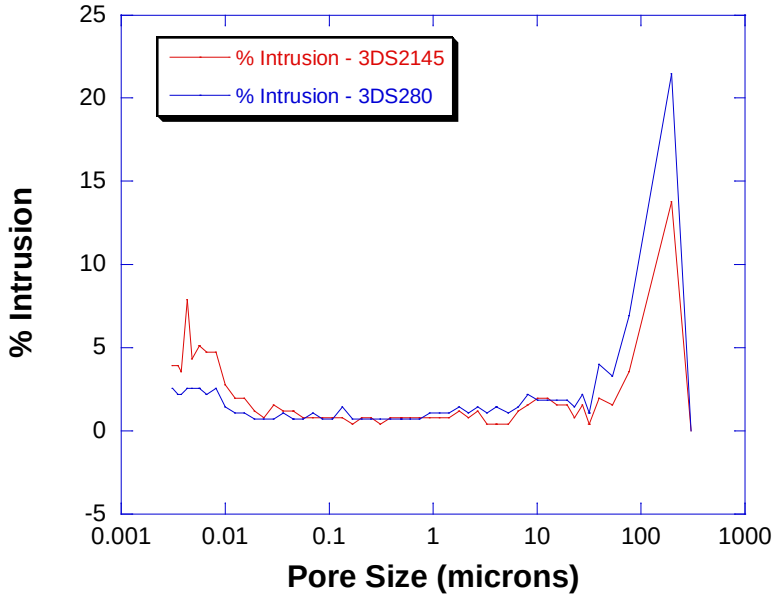


**Figure 38. Porosity Pore Size Measurements for 3-D S200 80 Mil and 3-D S200 145 Mil Using Mercury Porosimeter**

## 4.3 Tension Tests

Tension testing and data analysis was performed in accordance with ASTM C1359. The UTS, PL, and E were obtained from the analysis of the data collected from each tension test. The results are tabulated and presented in Table 6. Several of the specimens failed in the wider radius section or in the tab area. They are included in the report for information purposes only and would normally need to be censored. This issue is associated with intermediate temperature embrittlement and will be discussed later in the Discussion section of this report.

The PL is a very important CMC material property, as it determines when extensive matrix cracking has occurred. PLs were determined using the "10% Method", the first step of which was to plot the data collected from the tension tests. A linear fit was made to the data between 0 MPa and 50 MPa and these values were used to calculate a stress value for each strain measurement. Next, the difference between the actual stress and calculated stress values was determined. The PL was selected to be the stress value where the two values deviated by more than 10%.

From the table, one can observe that the 2-D S200 CMC exhibited good tensile strength at the test temperature of 1000°C. The average UTS was measured to be 262 MPa and the average strain to failure was 0.5%. However, the average PL was not exceptionally high at 83 MPa.

**Table 6. Tension Test Results for 2-D S200 and 3-D SiC/SiNC Manufactured with S200 Resin and Starfire Resin**

| Specimen Number | CMC Material Description | Test Temp. (C) | Net Ultimate Tensile Strength (MPa) | Strain To Failure (%) | Net Modulus (GPa) | Net Prop. Limit (MPa) | Failure Location |
|---|---|---|---|---|---|---|---|
| 2s280-9 | 2D, S200, 80 mils, 6 ply | 1000 | 251 | 0.48 | 97 | N/A | Gauge |
| 2s280-10 | 2D, S200, 80 mils, 6 ply | 1000 | 270 | 0.55 | 100 | 79 | Transition |
| 2s280-15 | 2D, S200, 80 mils, 6 ply | 1000 | 264 | 0.48 | 121 | 86 | Gauge |
| | | | | | | | |
| 3s280-5 | 3D, S200, 80 mil | 1000 | 106* | 0.16* | 163 | 63 | Grips |
| 3s280-6 | 3D, S200, 80 mil | 1000 | 160 | 0.28 | 165 | 84 | Transition |
| 3s280-11 | 3D, S200, 80 mil | 1000 | 176 | 0.34 | 171 | 79 | Radius |
| | | | | | | | |
| 3s2145-1 | 3D, S200, 145 mil | 1000 | 233 | 0.64 | 120 | 76 | Gauge |
| 3s2145-3 | 3D, S200, 145 mil | 1000 | 130***** | 0.22 | 120 | N/A | Center |
| 3s2145-4 | 3D, S200, 145 mil | 1000 | 225* | 0.55* | 116 | 70 | Grips |
| | | | | | | | |
| 3st80-1 | 3D, Starfire, 80 mil | 1000 | 180 | 0.16 | 165 | 140 | Gauge |
| 3st80-3 | 3D, Starfire, 80 mil | 1000 | 86***** | 0.06* | 146 | N/A | Radius |
| 3st80-15 | 3D, Starfire, 80 mil | 1000 | 141* | 0.13* | 164 | 120 | Radius |
| | | | | | | | |
| 3st145-11 | 3D, Starfire, 145 mil | 1000 | 90 | 0.24 | N/A | N/A | Gauge |
| 3st145-14 | 3D, Starfire, 145 mil | 1000 | 182 | 0.38 | N/A | 89 | Gauge |
| 3st145-17 | 3D, Starfire, 145 mil | 1000 | 145* | 0.22* | 162 | 76 | Radius |
| 3st145-18 | 3D, Starfire, 145 mil | 1000 | 122 | 0.22 | 155 | N/A | Gauge |

Note: All stess values calculated using the net corss-section of the test specimen

* These specimens failed in the wider area of the radius or tab area

In studying the four 3-D materials, the test data from the S200 145-mil material performed significantly better than the other three CMCs. Two of the tests were above 225 MPa, which is only 14% below the 2-D material, and strain to failure was also very good. However, the other 3-D CMCs exhibited very low strengths and strain-to-failure values. For several of the tests, the stress-versus-strain traces exhibited significant scatter, so measurement of a precise PL was difficult to achieve. There was also significant scatter in the PL, but the data suggests that all five CMC systems had similar PL values. It was thought that, the much straighter fibers of the 3-D weaves might result in higher PL values, but they did not, though they did exhibit a higher stiffness than the 2-D material. The 2-D material has approximately 20% fibers in each direction, while the 3-D systems had approximately 36% total fiber volume fraction, with 36% in the fill direction. However, it should be noted that, in the fill direction, there was one more ply than in the warp direction. This and the straightness of the fibers may have contributed to the increase in stiffness. However, more analysis is needed to confirm this. It is also worth noting that the 80-mil Starfire CMC exhibited the lowest strain to failure.

To illustrate this difference in the 2-D and 3-D materials, a combination tensile plot was created using a representative stress-versus-strain trace for each material system investigated. Figure 39 clearly shows that the 3-D S200 systems' strength is only slightly lower than the 2-D material, but the other 3-D systems are substantially lower. As mentioned above, the 3-D Starfire systems did exhibit slightly lower strain-to-failure values, as can be observed in the figure.

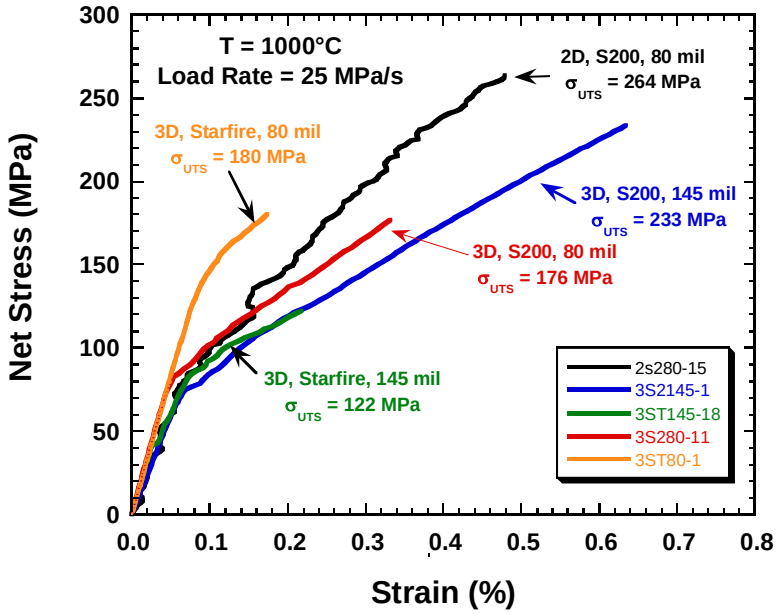


**Figure 39. Tensile Stress-Versus-Strain Behavior for 2-D S200 and 3-D SiC/SiNC Manufactured with S200 Resin and Starfire Resin**

## 4.4 Creep Rupture Tests

The creep/stress rupture testing was conducted at a constant stress at 1000°C for up to 360,000 seconds (100 hours). Stress values were selected based on the tensile stress-versus-strain behavior for each material. Results for all of the creep rupture experiments are tabulated in Table 7 and shown graphically as a plot of net creep rupture stress versus time to failure in Figure 40. The tensile strength of each CMC is plotted as a reference. Clearly. the high-temperature creep durability of the 2-D S200 material system is significantly better than any of the 3-D material systems, and highlights a significant debit in durability in changing the fiber preform architecture from 2-D to 3-D. For the 3-D material, there is a relatively small stress window where the specimens either fail in a short period of time or reach run-out. Thus, it is easy to define a stress limit. It is speculated that the sharp limit is directly related to the microstructure. As soon as the PL is reached, there is extensive opening of existing matrix cracks, as well as formation of specimen-wide matrix cracks. In addition, at fiber cross-over points in the fiber preform, there are large areas void of fibers. Many of these locations also have large cracks from processing, as well as large pores. There is significant data in the literature that suggests these regions experience significant cracking at very low loads and are the primary reason for such low stress values to reach run-out condition.

One interesting observation is that three of the 3-D materials reached run-out at approximately 110-120 MPa. Thus, creep rupture life is controlled by the major defects found in the fiber weave and not the preform thickness or resin material. Even the strongest in tension, the 3-D S200 145-mil material, had the same run-out as the other two systems. The 3-D Starfire 145 material exhibited the lowest tensile strength, which translated directly to the poorest creep performance. Run-out in this material did not occur until the stress was reduced to 76 MPa.

**Table 7. Creep Rupture Results for 2-D S200 and 3-D SiC/SiNC Manufactured with S200 Resin and Starfire Resin**

| Specimen Number | CMC Material Description | Test Temp. (C) | Net Creep Stress (MPa) | Time To Failure (Seconds) | Failure Location (mm) |
|---|---|---|---|---|---|
| 2s280-18 | 2D, S200, 80 mils, 6 ply | 1000 | 60 | 360000 | N/A |
| 2s280-11 | 2D, S200, 80 mils, 6 ply | 1000 | 80 | 360000 | N/A |
| 2s280-12 | 2D, S200, 80 mils, 6 ply | 1000 | 100 | 360000 | N/A |
| 2s280-19 | 2D, S200, 80 mils, 6 ply | 1000 | 140 | 360000 | N/A |
| 2s280-20 | 2D, S200, 80 mils, 6 ply | 1000 | 180 | 279360 | 0 |
| | | | | | |
| 3s280-15 | 3D, S200, 80 mil | 1000 | 115 | 360000 | -31 |
| 3s280-13 | 3D, S200, 80 mil | 1000 | 151 | 7920 | 0 |
| | | | | | |
| 3s2145-17 | 3D, S200, 145 mil | 1000 | 86 | 360000 | N/A |
| 3s2145-2 | 3D, S200, 145 mil | 1000 | 116 | 176760 | -27 |
| 3s2145-19 | 3D, S200, 145 mil | 1000 | 116 | 160920 | 19 |
| | | | | | |
| 3st80-4 | 3D, Starfire, 80 mil | 1000 | 108 | 360000 | N/A |
| 3st80-5 | 3D, Starfire, 80 mil | 1000 | 146 | 360 | 16 |
| | | | | | |
| 3st145-15 | 3D, Starfire, 145 mil | 1000 | 76 | 360000 | N/A |
| 3st145-9 | 3D, Starfire, 145 mil | 1000 | 86 | 360 | 8 |
| 3st145-13 | 3D, Starfire, 145 mil | 1000 | 86 | 94320 | 13 |

Note: All stess values calculated using the net cross-section of the test specimen

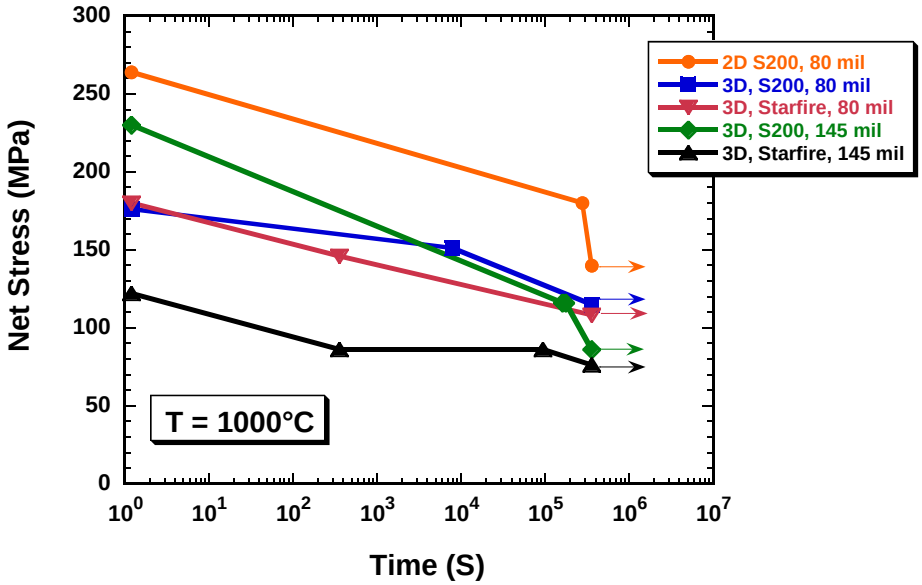


**Figure 40. Creep Rupture Plot Showing Net Stress Versus Time to Failure in Seconds for 2-D S200 and 3-D SiC/SiNC Manufactured with S200 Resin and Starfire Resin**

One can directly compare test data for the 2-D S200 material from this investigation to data generated several years ago (S200-0), as seen in Figure 41. It is worth noting that the current-generation material has an order of magnitude better creep resistance life than similar material manufactured a decade earlier. It is suggested that this improved creep resistance is a result of improved fiber coatings and processing improvements to the S200 matrix.

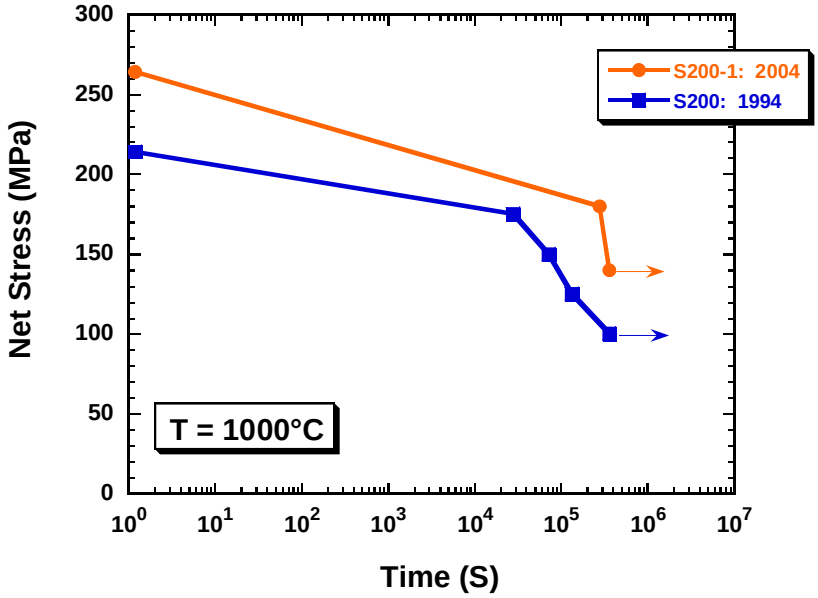


**Figure 41. Creep Rupture Data for 2-D S200 versus S200-1**

One can assess the creep behavior by constructing plots of creep strain versus time for each material system, as well as total strain versus time. Creep strain occurs immediately after reaching the desired stress level for each experiment and total strain includes that which results during the ramp to maximum load. For the higher stress levels, this initial loading strain can be significant.

Figure 42 presents the creep strain-versus-time for five tests conducted on the 2-D S200 baseline material. In all cases, the material exhibits an initial primary creep region that transitions rather quickly to a nearly linear rate of strain accumulation with time. None of the experiments conducted exhibited tertiary creep. Under closer inspection of the data, creep rate continues to slightly decrease with increasing time. The 2-D S200 material performed well in creep, and creep strain had to exceed 0.2% before failure was observed. Figure 43 presents total strain versus time for the same five tests. The results are similar, but it is worth noting that the specimen tested at a creep stress of 180 MPa exceeded 0.4% total strain and ran for almost 300,000 cycles. This is very good creep performance.

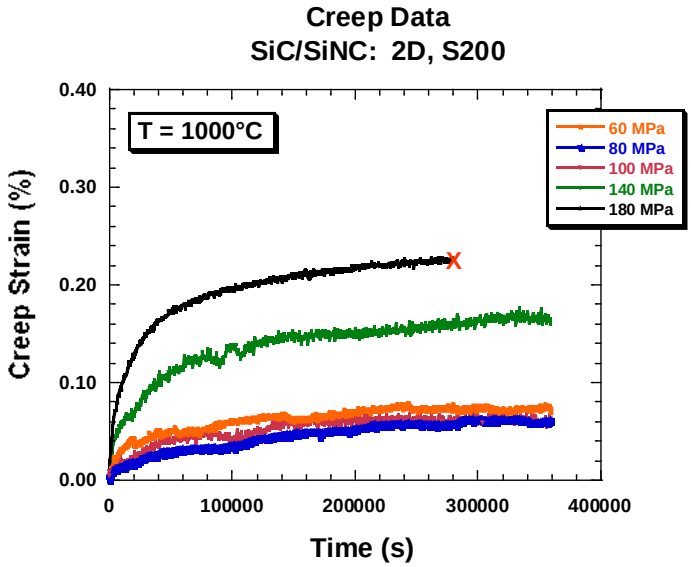


**Figure 42. Creep Strain Versus Time for 2-D S200 Creep Tested at 1000°C**

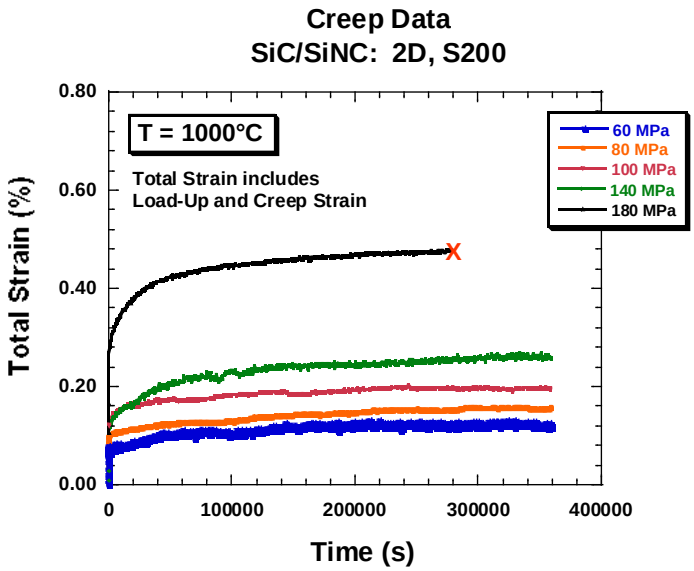


**Figure 43. Total Creep Strain Versus Time for 2-D S200 Creep Tested at 1000°C**

Figure 44 presents creep strain versus time for the 3-D S200 80-mil material, which only reached 0.1% creep strain before failure occurred. Figure 45 presents total strain versus time and, here, the material exceeds 0.3% total strain before failure occurs. This is well below the runout for 2D S200, but still reasonably good total strain to failure.

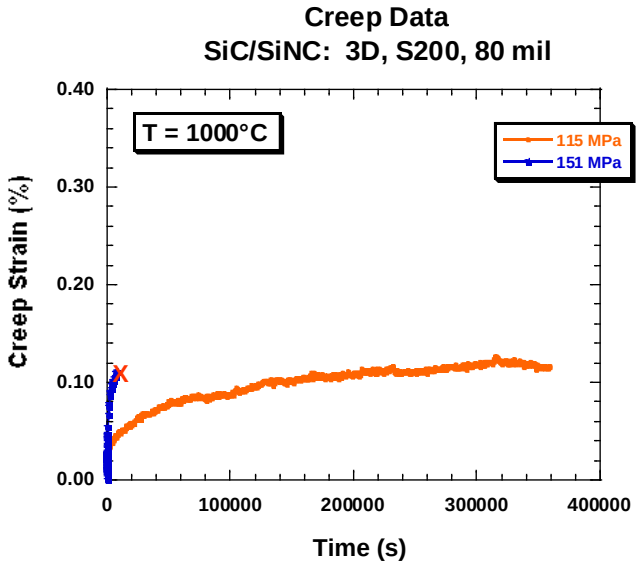


**Figure 44. Creep Strain Versus Time for 3-D S200 80 Mil Creep Tested at 1000°C**

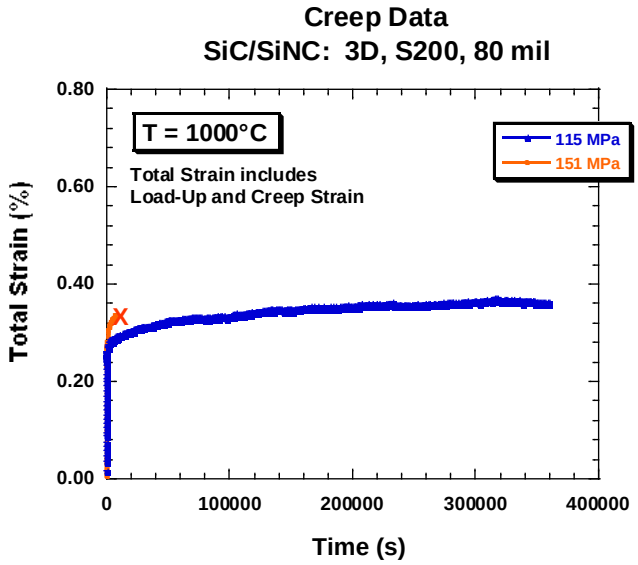


**Figure 45. Total Strain Versus Time for 3-D S200 80 Mil Creep tested at 1000°C**

Figure 46 presents creep strain versus time for the 3-D S200 145-mil material, which exhibited similar behavior to the 3-D S200 80 mill material. This system was the strongest of the 3-D materials and, yet, the creep run-out stress is still limited to under 0.1%. Therefore, tensile strength does not translate to good creep performance. Figure 47 presents total strain versus time and failures occur after reaching 0.2% total strain.

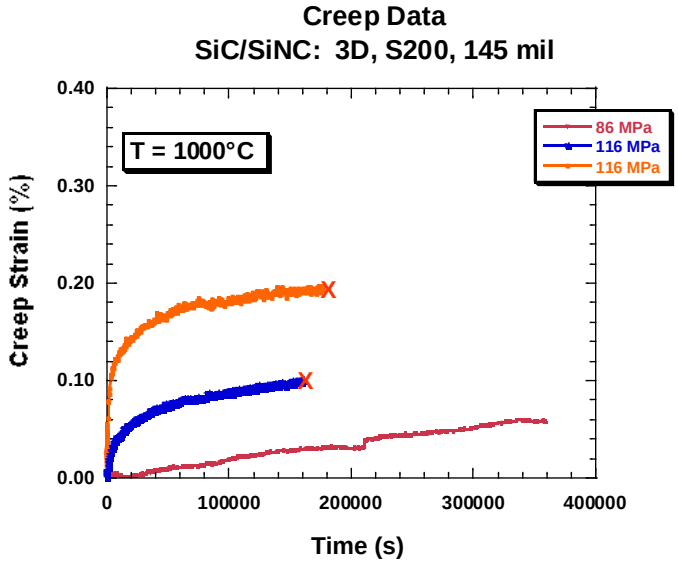


**Figure 46. Creep Strain Versus Time for 3-D S200 145 Mil Creep Tested at 1000°C**

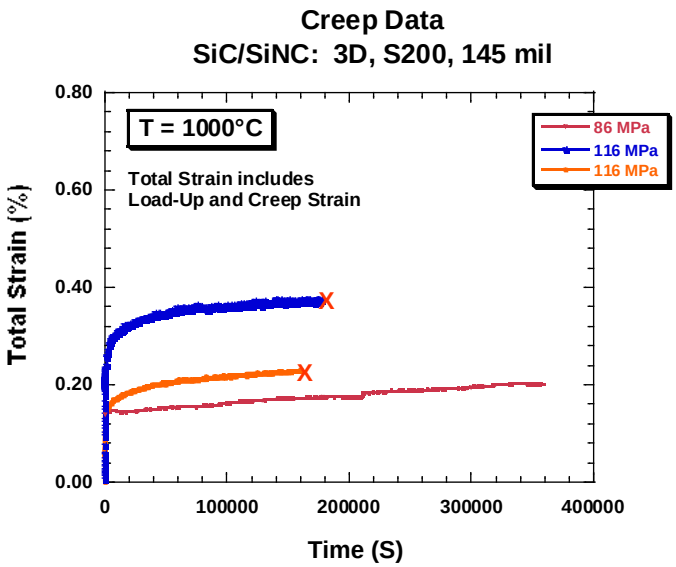


**Figure 47. Total Strain Versus time for 3-D S200 145 mil Creep Tested at 1000°C**

Figure 48 presents creep strain versus time for the 3-D Starfire 80-mil material, which experienced very low strain-to-failure values in both the tension and creep rupture tests. Figure 49 shows the total strain versus time and the maximum strain to reach run-out was only 0.1%.

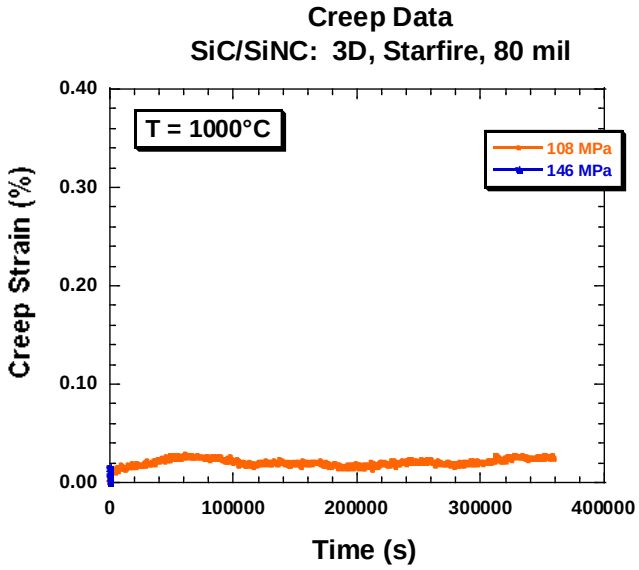


**Figure 48. Creep Strain Versus Time for 3-D Starfire 80 Mil Creep Tested at 1000°C**

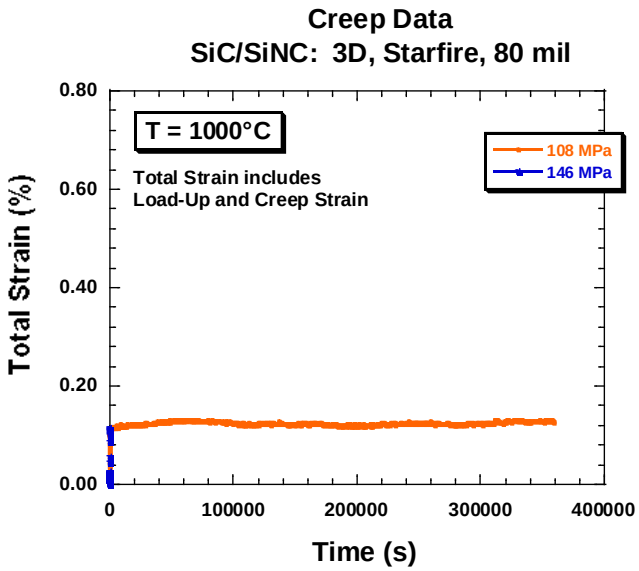


**Figure 49. Total Strain Versus Time for 3-D Starfire 80 Mil Creep Tested at 1000°C**

Figure 50 presents creep strain versus time for the 3-D S200 1450-mil material, which only reached less than 0.1% strain before failure. Figure 51 presents total strain versus time and the highest total strain for a run-out test was 0.2%.

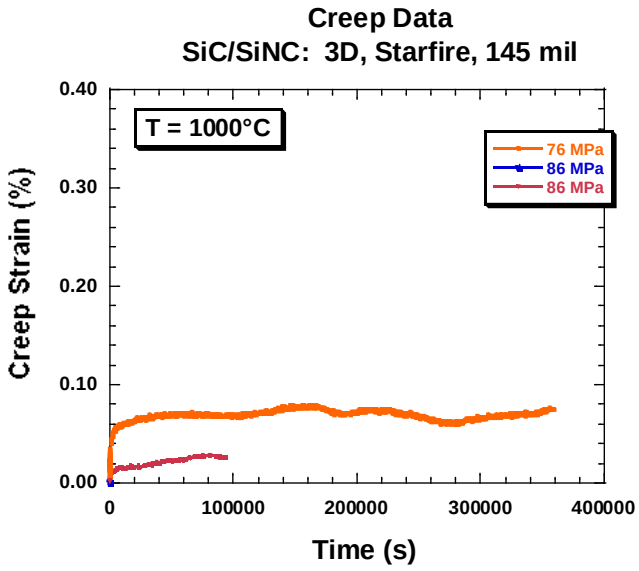


**Figure 50. Creep Strain Versus Time for 3-D Starfire 145 Mil Creep Tested at 1000°C**

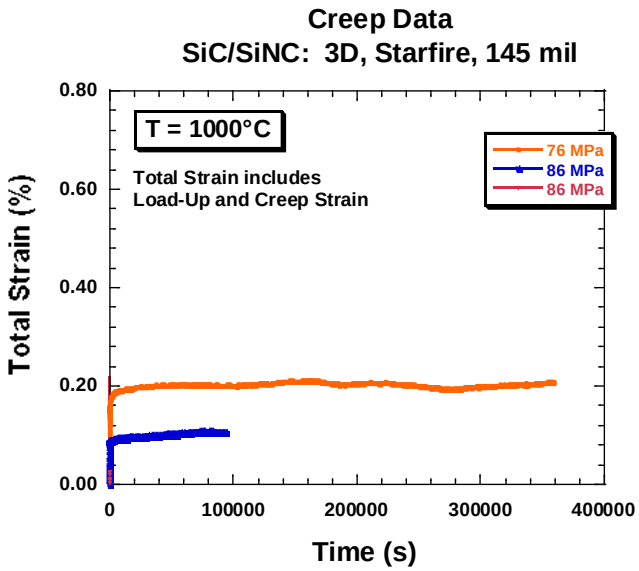


**Figure 51. Total Strain Versus Time for 3-D Starfire 145 Mil Creep Tested at 1000°C**

## 4.5 Fatigue Tests

Results of constant-amplitude fatigue testing at 1000°C are listed in Table 8 and presented in the S-N plot shown in Figure 52 using the adjusted net-section cross-sectional area to calculate stress. Very few tests were conducted, but all five CMC systems exhibited a similar fatigue performance. The run-out stress values may have ranged from 80 MPa to 100 MPa, as shown in the table, but extrapolating the traces in the fatigue S-N plot indicates they all would likely have run-out in a stress range of 75-80 MPa.

Similar to the creep plots previously shown, the tensile strength is included and is plotted versus one fatigue cycle in order to estimate fatigue behavior over a wider range of cyclic life. There are considerable differences in the starting tensile strengths for the five CMCs; however, the fatigue curves for both 2-D and 3-D materials tend to converge at the higher cyclic lives. This is a very dramatic finding, and clearly highlights the importance of studying the fatigue behavior of the material. It also suggests that there is an inherent fatigue life for this class of CMC, which is independent of specimen thickness, type of matrix material, or fiber weave architecture.

To further clarify this statement, the fatigue behavior of the 2-D S200 material was compared to data generated over a decade earlier on 2-D S200-0 material, shown in Figure 53. The fatigue data for both versions of the S200 lay on top of each other. Thus, over the last decade, improvements in the material have improved the creep resistance, but the fatigue durability has remained relatively unchanged and is attributed to the extensively cracked matrix that results from PIP processing these types of SiC/SiNC CMCs.

**Table 8. Fatigue Results for 2-D S200 and 3-D SiC/SiNC Manufactured with S200 Resin and Starfire Resin**

| Specimen Number | CMC Material Description | Test Temp. (C) | Net Fatigue Stress (MPa) | Cycles To Failure (N) | Failure Location (mm) |
|---|---|---|---|---|---|
| 2S280-14 | 2D, S200, 80 mils, 6 ply | 1000 | 140 | 32,760 | 3 |
| 2S280-13 | 2D, S200, 80 mils, 6 ply | 1000 | 120 | 69,820 | -3 |
| 2S280-16 | 2D, S200, 80 mils, 6 ply | 1000 | 80 | 360,000 | N/A |
| | | | | | |
| 3S280-12 | 3D, S200, 80 mil | 1000 | 110.7 | 25,556 | 1 |
| 3S280-10 | 3D, S200, 80 mil | 1000 | 73.8 | 360,000 | N/A |
| | | | | | |
| 3S2145-5 | 3D, S200, 145 mil | 1000 | 85.2 | 125,148 | 9 |
| 3S2145-18 | 3D, S200, 145 mil | 1000 | 57.9 | 360,000 | N/A |
| | | | | | |
| 3ST80-13 | 3D, Starfire, 80 mil | 1000 | 110.5 | 13,554 | -9 |
| 3ST80-19 | 3D, Starfire, 80 mil | 1000 | 72.2 | 360,000 | N/A |
| | | | | | |
| 3ST145-12 | 3D, Starfire, 145 mil | 1000 | 85.2 | 219,566 | -16 |
| 3ST145-16 | 3D, Starfire, 145 mil | 1000 | 57.7 | 360,000 | N/A |

Note: All stess values calculated using the net corss-section of the test specimen

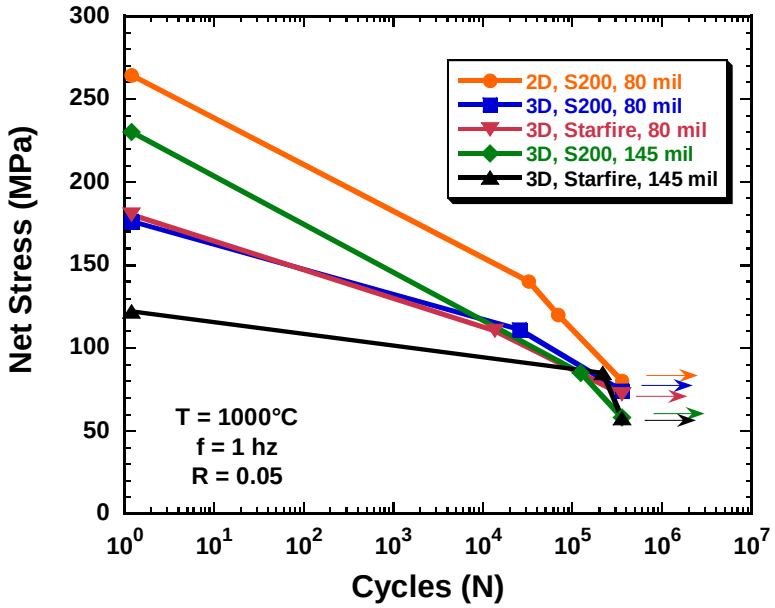


**Figure 52. Fatigue Plot of Net Stress Versus Cycles to Failure for 2-D S200 and 3-D SiC/SiNC Manufactured with S200 Resin and Starfire Resin**

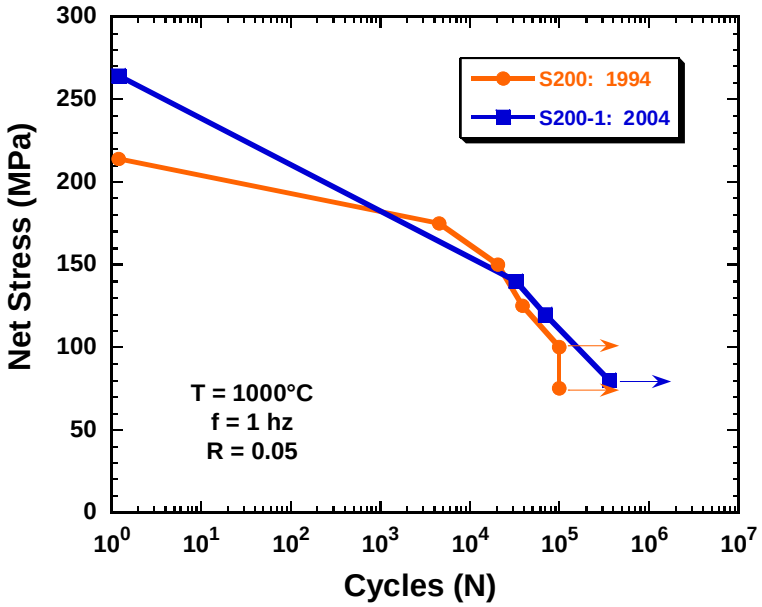


**Figure 53. Fatigue Plot of Net Stress Versus Cycles to Failure for 2-D SiC/SiNC S200-1 Compared to Data Generated on S200-0 Manufactured in 1994**

## 4.6 Shear Testing

The individual results of interlaminar shear tests for both the DNC tested at 21°C and short-beam shear (i.e., 3-point loading) method tested at 21°C and 1000°C are presented in Table 9. The DNC results produced shear strengths of about 30 MPa for the 2-D material and approximately double that for the 3-D materials. There was not much difference in thickness or matrix material. The short-beam shear tests produced similar values for all materials and for both RT tests, while several of the 3-D materials exhibited an increase in strength with increased temperature.

The attempt to obtain interlaminar shear failures under 3-point loading proved futile, with all samples failing as a result of either compression, failure of the top plies, or tensile failure in the bottom plies prior to interlaminar failures. Nonetheless, the data are presented as an estimation of a lower bound or minimum interlaminar shear strength for each architecture and test temperature examined. Worth noting is that, for the elevated-temperature case, nearly all 3-D samples tested at 1000°C failed via tension or compression of the outer plies prior to interlaminar shear failure, up to shear stresses in excess of 40 MPa.

**Table 9. Shear Results for 2-D S200 and 3-D SiC/SiNC Manufactured with S200 Resin and Starfire Resin**

| Specimen Number | CMC Material Description | Test Temp. (C) | Test Method | Max Shear Stress (MPa) | Failure Type |
|---|---|---|---|---|---|
| 2S280-8 | 2D, S200, 80 mil | 21 | Double Notch | 24.5 | ils |
| 2S280-28 | 2D, S200, 80 mil | 21 | Double Notch | 41.3 | ils |
| 2S280-23 | 2D, S200, 80 mil | 21 | Short Beam | ≥44 | comp. |
| 2S280-4 | 2D, S200, 80 mil | 1000 | Short Beam | ≥48 | tensile |
| 2S280-24 | 2D, S200, 80 mil | 1000 | Short Beam | ≥41 | tensile |
| | | | | | |
| 3S280-3 | 3D, S200, 80 mil | 21 | Double Notch | 111 | ils |
| 3S280-4 | 3D, S200, 80 mil | 21 | Double Notch | 104 | ils |
| 3S280-17 | 3D, S200, 80 mil | 21 | Short Beam | ≥41 | tensile |
| 3S280-18 | 3D, S200, 80 mil | 1000 | Short Beam | ≥55 | tensile |
| | | | | | |
| 3S2145-10 | 3D, S200, 145 mil | 21 | Double Notch | 81.1 | ils |
| 3S2145-14 | 3D, S200, 145 mil | 21 | Double Notch | 110 | ils |
| 3S2145-6 | 3D, S200, 145 mil | 21 | Short Beam | ≥38 | tensile |
| 3S2145-7 | 3D, S200, 145 mil | 1000 | Short Beam | ≥52 | tensile |
| 3S2145-8 | 3D, S200, 145 mil | 1000 | Short Beam | ≥47 | tensile |
| 3S2145-9 | 3D, S200, 145 mil | 1000 | Short Beam | ≥52 | tensile |
| | | | | | |
| 3ST80-13 | 3D, Starfire, 80 mil | 21 | Double Notch | 91.7 | ils |
| 3ST80-20 | 3D, Starfire, 80 mil | 21 | Double Notch | 69.7 | ils |
| 3ST80-9 | 3D, Starfire, 80 mil | 21 | Short Beam | ≥21 | tensile |
| 3ST80-8 | 3D, Starfire, 80 mil | 1000 | Short Beam | ≥46 | tensile |
| 3ST80-10 | 3D, Starfire, 80 mil | 1000 | Short Beam | ≥56 | tensile |
| 3ST80-11 | 3D, Starfire, 80 mil | 1000 | Short Beam | ≥36 | tensile |
| | | | | | |
| 3ST145-8 | 3D, Starfire, 145 mil | 21 | Double Notch | 86.9 | ils |
| 3ST145-20 | 3D, Starfire, 145 mil | 21 | Double Notch | 77 | ils |
| 3ST145-1 | 3D, Starfire, 145 mil | 21 | Short Beam | ≥29 | tensile |
| 3ST145-2 | 3D, Starfire, 145 mil | 1000 | Short Beam | ≥42 | tensile |
| 3ST145-3 | 3D, Starfire, 145 mil | 1000 | Short Beam | ≥40 | tensile |
| 3ST145-4 | 3D, Starfire, 145 mil | 1000 | Short Beam | ≥50 | tensile |

ils: interlaminar shear

comp: compression in top plies (under load point) prior to interlaminar shear failure

tensile: tensile failure in outermost fibers prior to interlaminar shear failure

Figure 54 presents the DNC data in the form of a bar chart where one can easily see that the 3-D architecture more than doubles the shear strength of S200. There appears to be little difference between the 80-mil and 145-mil materials; however, the S200-matrix materials appear to be slightly stronger than the Starfire-matrix materials.

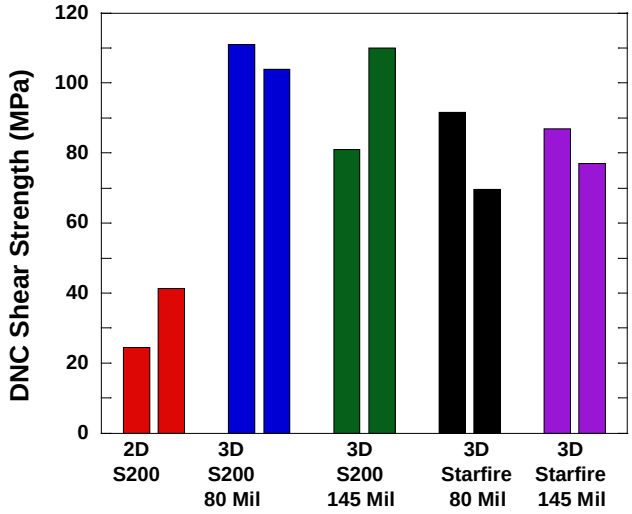


**Figure 54. Double-Notch Compression Shear Stress Values for 2-D S200 and 3-D SiC/SiNC Manufactured with S200 Resin and Starfire Resin**

Figure 55 presents the short-beam shear results in the form of a bar chart for each CMC material. For the tests at RT, the 2-D and 3-D S200 systems appear to be stronger than the Starfire systems. At 1000°C, all of the 3-D systems exhibited significantly higher shear stress values than the 2-D S200 CMC, but there is little difference between the four 3-D systems.

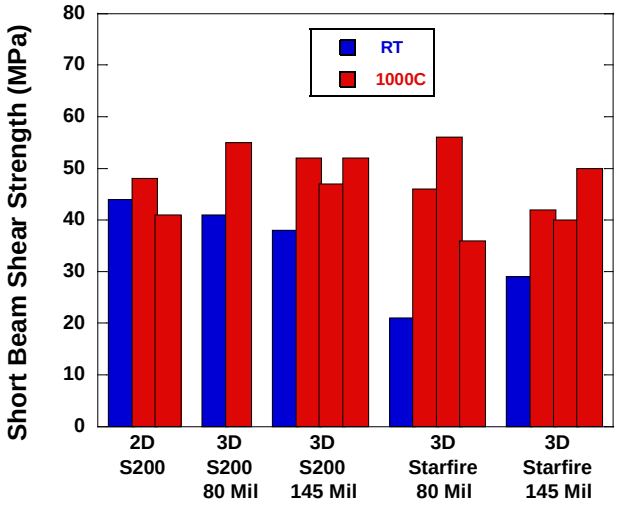


**Figure 55. Short-Beam Shear Stress Values for 2-D S200 and 3-D SiC/SiNC Manufactured with S200 Resin and Starfire Resin**

## 4.7 Transthickness Tension Tests

The test matrix called for testing five specimens for each material configuration. However, during testing, there were issues with the adhesive. Therefore, no results are reported.

## 5.0 DISCUSSION

### 5.1 Tensile Results

The 3-D S200 145-mil material was much stronger than the other three 3-D CMCs. This was a bit surprising, given that they all received the same initial prepreg of S200 plus filler infiltration. Therefore, it is suggested that the likely cause in this strength difference is the fiber coating. Each of the preforms were coated separately. It appears the 3D S200 145-mil fiber preform may have a much better fiber coating. However, COIC requested that no analytical studies be performed on the fiber coatings, and that request was honored. The 3-D Starfire 80-mil CMC exhibited the lowest strain to failure, and that may also be indicative more of the fiber coating quality than the Starfire resin itself. The impact of the fiber coating quality will be discussed in a following section.

### 5.2 Residual Strength of Test Specimens Reaching Run-Out

Tensile and creep test specimens that reached 360,000 seconds of test time were considered run-outs. These specimens were cooled to RT and tension tests were conducted. Table 10 presents the results from the creep rupture run-out tests testing, while Table 11 presents the residual strength results for the fatigue run-out specimens.

**Table 10. Residual Strength Tension Test Results for Creep Rupture Specimens Reaching Run-Out**

| Specimen Number | CMC Material Description | Test Temp. (C) | Net Creep Stress (MPa) | Time To Failure (Seconds) | Net Residual Tensile Strength (MPa) | Strain To Failure (%) | Failure Location (mm) |
|---|---|---|---|---|---|---|---|
| 2s280-18 | 2D, S200, 80 mils, 6 ply | 1000 | 60 | 360000 | 212* | 0.32* | -30 |
| 2s280-11 | 2D, S200, 80 mils, 6 ply | 1000 | 80 | 360000 | 145 | 0.18 | -6 |
| 2s280-12 | 2D, S200, 80 mils, 6 ply | 1000 | 100 | 360000 | 208 | 0.24 | 8 |
| 2s280-19 | 2D, S200, 80 mils, 6 ply | 1000 | 140 | 360000 | 258* | 0.33* | 11 |
| 2s280-20 | 2D, S200, 80 mils, 6 ply | 1000 | 180 | 279360 | N/A | N/A | 0 |
| 3s280-15 | 3D, S200, 80 mil | 1000 | 115 | 360000 | 99* | 0.13* | -31 |
| 3s280-13 | 3D, S200, 80 mil | 1000 | 151 | 7920 | N/A | N/A | 0 |
| 3s2145-17 | 3D, S200, 145 mil | 1000 | 86 | 360000 | 68* | 0.08* | -32 |
| 3s2145-2 | 3D, S200, 145 mil | 1000 | 116 | 176760 | N/A | N/A | -27 |
| 3s2145-19 | 3D, S200, 145 mil | 1000 | 116 | 160920 | N/A | N/A | 19 |
| 3st80-4 | 3D, Starfire, 80 mil | 1000 | 108 | 360000 | 97 | 0.08 | 6 |
| 3st80-5 | 3D, Starfire, 80 mil | 1000 | 146 | 360 | N/A | N/A | 16 |
| 3st145-15 | 3D, Starfire, 145 mil | 1000 | 76 | 360000 | 92 | 0.13 | 3 |
| 3st145-9 | 3D, Starfire, 145 mil | 1000 | 86 | 360 | N/A | N/A | 8 |
| 3st145-13 | 3D, Starfire, 145 mil | 1000 | 86 | 94320 | N/A | N/A | 13 |

Note: All stess values calculated using the net cross-section of the test specimen

* These test specimens failed in the wider radius or tab area of the specimen

**Table 11. Residual Strength Tension Test Results for Fatigue Specimens Reaching Run-Out**

| Specimen Number | CMC Material Description | Test Temp. (C) | Net Fatigue Stress (MPa) | Cycles To Failure (N) | Net Residual Tensile Strength (MPa) |
|---|---|---|---|---|---|
| 2S280-14 | 2D, S200, 80 mils, 6 ply | 1000 | 140 | 32,760 | N/A |
| 2S280-13 | 2D, S200, 80 mils, 6 ply | 1000 | 120 | 69,820 | N/A |
| 2S280-16 | 2D, S200, 80 mils, 6 ply | 1000 | 80 | 360,000 | 190* |
| 3S280-12 | 3D, S200, 80 mil | 1000 | 110.7 | 25,556 | N/A |
| 3S280-10 | 3D, S200, 80 mil | 1000 | 73.8 | 360,000 | 146 |
| 3S2145-5 | 3D, S200, 145 mil | 1000 | 85.2 | 125,148 | N/A |
| 3S2145-18 | 3D, S200, 145 mil | 1000 | 57.9 | 360,000 | 147 |
| 3ST80-13 | 3D, Starfire, 80 mil | 1000 | 110.5 | 13,554 | N/A |
| 3ST80-19 | 3D, Starfire, 80 mil | 1000 | 72.2 | 360,000 | 79* |
| 3ST145-12 | 3D, Starfire, 145 mil | 1000 | 85.2 | 219,566 | N/A |
| 3ST145-16 | 3D, Starfire, 145 mil | 1000 | 57.7 | 360,000 | 125 |

Note: All stess values calculated using the net corss-section of the test specimen

* These specimens failed in the wider radius and tab area of test specimen

In creep rupture testing, none of the 2-D S200 specimens failed outside of the gage section, but the same is not true for the 3-D materials. The majority of these specimens failed outside of the machined gauge section, making the reporting of a residual tensile strength meaningless. Typically. the failure locations were in the wider tab region very near the radius and a significant distance away from the grips. This is a result of intermediate temperature embrittlement and there is significant documentation of this phenomenon in the literature. In essence, at intermediate temperatures (typically 900°C and below), oxidation can occur faster than the formation of sealing phases. Those regions of the CMC that are at 1000°C develop sealing phases that inhibit the ingress of oxygen into the CMC. Those areas at or below 900°C do not get this protection, resulting in faster oxygen ingress into the CMC and faster embrittlement.

What is interesting is that many of these creep rupture run-out specimens were at loads above the PL during the creep or fatigue tests at 1000°C, but during the RT residual strength tension tests, they often failed at lower stress values. Even more concerning is the issue that, at the failure locations, the cross-section is approximately 60% wider than in the gage section. In several cases, the specimens failed at a calculated stress value of approximately 40 MPa. It is suggested that, on cooling, glassy phases solidify and act to bond the fibers and matrix within the CMC. Such bonding makes the CMC significantly more susceptible to crack growth and greatly decreases the fracture toughness behavior of the material. Instead of exhibiting non-linear stress-strain behavior during tension testing, it now exhibits linear stress versus strain to failure that is akin to monolithic ceramics.

The residual strength tests for the fatigue specimens that reached run-out did not fail below the stress value they were fatigued at, but all exhibited a significant decrease in tensile strength compared to the as-manufactured strengths. This clearly indicates the CMCs were significantly degrading during the fatigue tests.

### 5.3 Fracture Surface Studies and Microstructural Analysis

It is suggested that the observed degradation that occurs in these PIP-processed materials can be traced back to the early stage of processing of these CMCs. There is a big strength difference between the 2-D S200 and the 3-D systems. All have similar amounts of fibers in the loading direction; therefore, the differences are attributed to the fiber coatings. Detailed microscopy was performed on 2-D and 3-D S200 80-mil material. Both microstructure and fracture surfaces were studied.

Figure 56 is a high-resolution (1000×) SEM micrograph of a polished cross-section of 2-D S200. In this image, there appears to be very little touching of fibers, as they are spaced out nicely, with only a few instances where two are touching. Even where they do touch, it appears there is a fine fiber-matrix interphase between them and very few look to be bonded together. It was estimated that only approximately 10-15% of the fibers might be slightly bonded together.

Figure 57 is a high-resolution (1000×) SEM image of the fracture surface of a tension-tested specimen at 1000°Cshowing that the fibers are well spread out and there is good fiber pull-out length. All fibers appear to have failed randomly and not as a group, suggesting a very good fiber coating. Figure 58 is an even-higher resolution (5000×) image of the fracture surface, showing excellent separation of the matrix from the fibers – none have bonded either to the matrix or to another fiber. This is excellent fracture morphology for a CMC and can likely be attributed to the good tensile strengths recorded.

Figure 59 is a high-resolution (1000×) SEM micrograph of a polished cross-section of 3-D S200 145-mil material. In this polished cross-section, surface bonding between adjacent fibers was observed in more than 50% of the material (in some cases as high as 70-80%). It is speculated that this fiber-to-fiber bonding leads to the low strength in the 3-D materials and greatly reduced strain to failure.

Figure 60 is a high-resolution (1000×) SEM image of the fracture surface of a tensile-tested 3-D S200 145-mil specimen that was the highest strength of the four 3-D systems. In the image, there are clear indicators that surface bonding was significant and there are groupings of fractured fibers that failed together in the same plane. Many of these failures originate from the location where the fibers were touching and have, subsequently, bonded together. This is indicated by the presence of river patterns that clearly point back to the fracture-origination site. These microstructural studies suggest that this bonding occurred during the processing of the CMC and appears to be even more severe in the other three 3-D material. Such fracture surfaces are a clear indicator that the fiber coating was inferior.

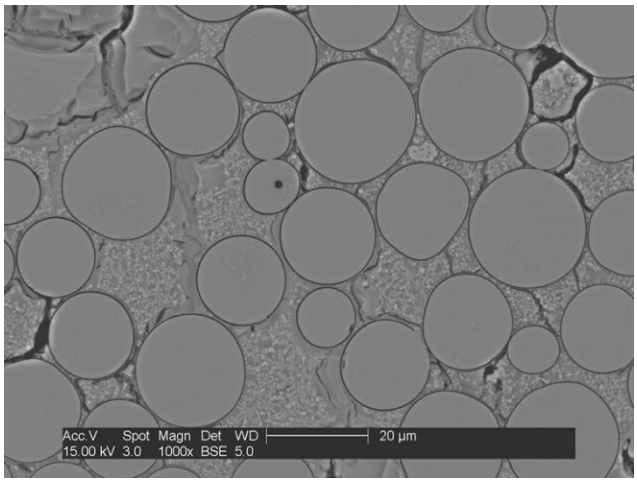


**Figure 56. SEM Image of Polished 2-D S200-1, 80 mil @ 1000×**

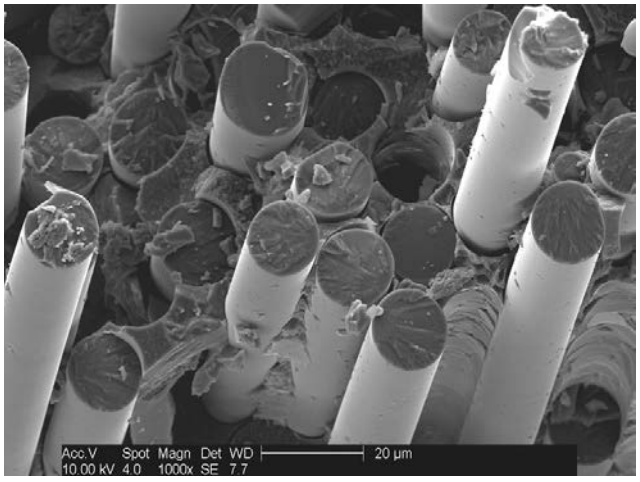


**Figure 57. SEM Image of Fractured 2-D S200-1, 80 mil @ 1000×**

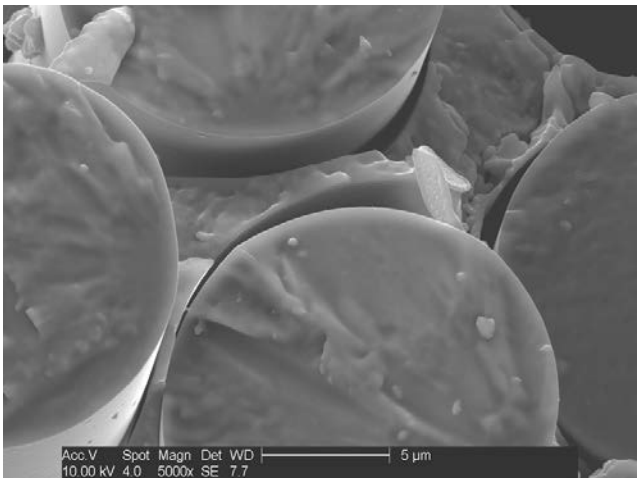


**Figure 58. SEM Image of Fractured 2-D S200, 80 mil @ 5000×**

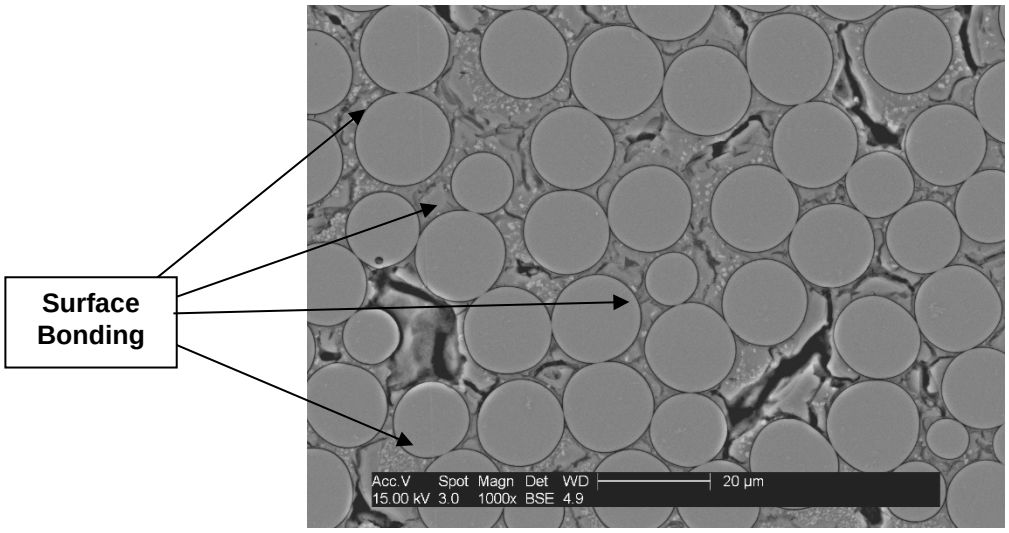


**Figure 59. SEM Image of Polished 3-D S200-1, 145 mil @ 1000×**

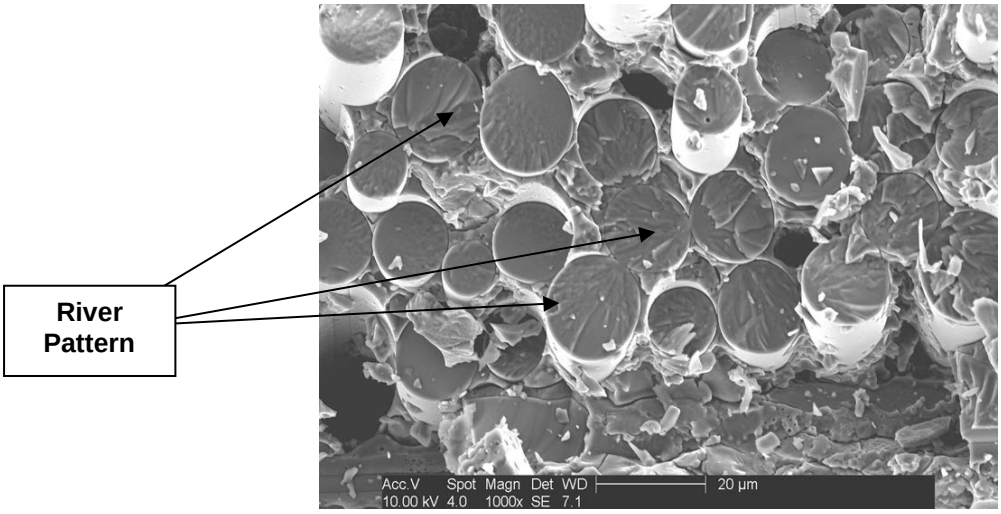


**Figure 60. SEM Image of Fractured 3-D S200, 145 mil @ 1000×**

## 6.0 CONCLUSIONS

The 2-D S200 CMC performed well and appears to have a good fiber coating. Tensile strength was far superior to any of the 3-D systems. Fiber volumes in the loading direction were similar, so the difference is attributed to the quality of the fiber coatings.

The S200 resin resulted in slightly better-performing 3-D CMCs than the Starfire resin. However, this is somewhat compromised by the fact that they all were first infiltrated with a S200 resin plus filler. Changing the fiber preform from 8HSW 2-D to 3-D produces a significant decrease in the in-plane properties. However, even with the poor in-plane properties, the in-plane shear strength increased by approximately 200 percent.

The 2-D S200 performed much better in creep rupture than the 3-D CMCs. The investigation into the two different thicknesses was inconclusive. The 3-D S200 145-mil material had the highest tensile strength of the four 3-D materials, so it appears there is no issue in coating fiber preforms up to 145 mils thick. The 2-D S200 material creep performance was superior to that of the four 3-D systems. However, the four 3-D systems exhibited nearly the same stress level to reach run-out.

All five CMC systems exhibited nearly the same stress level to reach fatigue run-out. In addition, S200 and S200-0 both exhibited the same run-out stress level in fatigue. This indicates that PIP-processed CMCs like these may have an inherent fatigue limit and it is suggested that it is a result of all the matrix cracks that form during processing.

The 3-D fiber preforms needed better fiber coatings. Microstructural analysis clearly showed that fibers were touching each other and there was no matrix and/or coating between a significant number of them. During the high-temperature processing, many of these touching fibers bond together and result in lower-strength composites.

Microstructural studies of polished cross-sections and fracture surfaces confirmed that the 3-D systems had poor-quality coatings. Many of the fibers were bonded together during processing and resulted in brittle-looking fracture surfaces and lower performance in tensile, creep, and fatigue.

All of the 3-D specimens showed a significant decrease in tensile strength and creep rupture behavior compared to 2-D material. However, the fatigue behavior was unaffected by changes in the preform, suggesting the first-order fatigue behavior is governed by the matrix processing that produces extensive cracks which allow ingress of oxygen and environmentally driven degradation. The fiber weave had, essentially, no effect.

Many of the run-out specimens exhibited failures outside of the machined gauge section when tension tested at RT to measure retained tensile strength. This indicates that intermediate temperature embrittlement severely affects this material in the same manner that has been reported in the literature.

## 7.0 RECOMMENDATIONS

It is recommended that tension and shear tests be conducted in both the warp and fill directions for 3-D fiber architectures.

The effect of machining off the loops at the surface of the preforms should be investigated.

Weaves that do not cause such large loops at the surface, such as 2.5-D angle interlock weaves, should be investigated.

The investigation into the S200 and Starfire resins was inconclusive. CMCs could be made with the starting resin being either S200 or Starfire.

Z weaver tows that are much smaller than what is currently used should be investigated. This will require the fiber manufacturers to spin the fiber tows with a smaller number of fibers to decrease the denier of the tow.

The material could most certainly utilize an exterior surface coating to slow down environmental attack and possibly address the intermediate temperature issue.

## 8.0 REFERENCES


[1] ASTM Alignment Bouillon, E.P., Lamouroux, F., Baroumes, L., Cavalier, J.C., Spriet, P.C. and Habarou, G., "An Improved Long Life Duration CMC for Jet Aircraft Engine Applications", ASME paper No. GT-2002-30625 (2002).

[2] Staehler, J.M. and Zawada, L.P., "Performance of Four Ceramic-Matrix Composite Divergent Flap Inserts Following Ground Testing on an F100 Turbofan Engine", *Journal of the American Ceramic Society*, 83, [7], pp 1727-17-38 (2000).

[3] ASTM C1275-00, Standard Test Method for Monotonic Tensile Behavior of Continuous Fiber-Reinforced Advanced Ceramics with Solid Rectangular Cross-Section Test Specimens at Ambient Temperatures", ASTM, 100 Barr Harbor Drive, West Conshohocken, PA, USA, June 10, 2000.

[4] ASTM 1359-96, "Standard Test Method for Monotonic Tensile Behavior of Continuous Fiber-Reinforced Advanced Ceramics with Solid Rectangular Cross-Section Test Specimens at Elevated Temperatures", ASTM, 100 Barr Harbor Drive, West Conshohocken, PA, USA, December, 1997

[5] ASTM C1360-96, Standard Practice for Constant-Amplitude, Axial, Tension-Tension Cyclic Fatigue of Continuous Fiber-Reinforced Advanced Ceramics at Ambient Temperatures", ASTM, 100 Barr Harbor Drive, West Conshohocken, PA, USA, December 10, 1996.

[6] ASTM C1337-96, "Standard Test Method for Creep and Creep Rupture of Continuous Fiber-Reinforced Advance Ceramics with Solid Rectangular Cross-Section Test Specimens at Elevated Temperatures", ASTM, 100 Barr Harbor Drive, West Conshohocken, PA, USA, June 10, 1996.

[7] ASTM C1292-0, Standard Test Method for Shear Strength of Continuous Fiber-Reinforced Advanced Ceramics at Ambient Temperatures", ASTM, 100 Barr Harbor Drive, West Conshohocken, PA, USA, July 2000.

[8] ASTM C2344-16, "Standard Test Method for Short-Beam Shear of Polymer Matrix Composite Materials and Their Laminates", ASTM, 100 Barr Harbor Drive, West Conshohocken, PA, USA, 2016.

[9] ASTM E1012-14, "Standard practice For Verification of Testing Frame and Specimen Alignment Under Tensile and Compressive Axial Force Application", ASTM, 100 Barr Harbor Drive, West Conshohocken, PA, USA, July 21, 2014.

# APPENDIX A

## A-1 MICROGRAPH IMAGES

### A-1.1 2-D, S200-1, 80 MIL

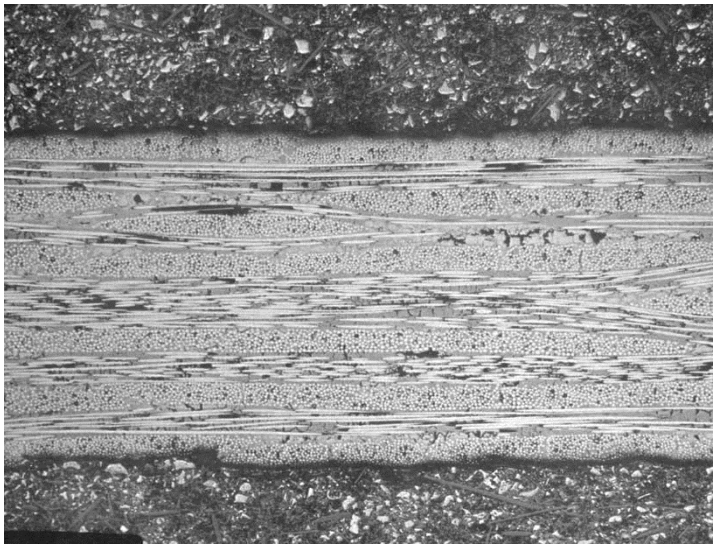

**Figure A-1.1.1: Micrograph of 2-D S200, 80 mil @ 25x, AB.** Image illustrate the standard 2-D, S200-1 with a thickness of 80 mil.

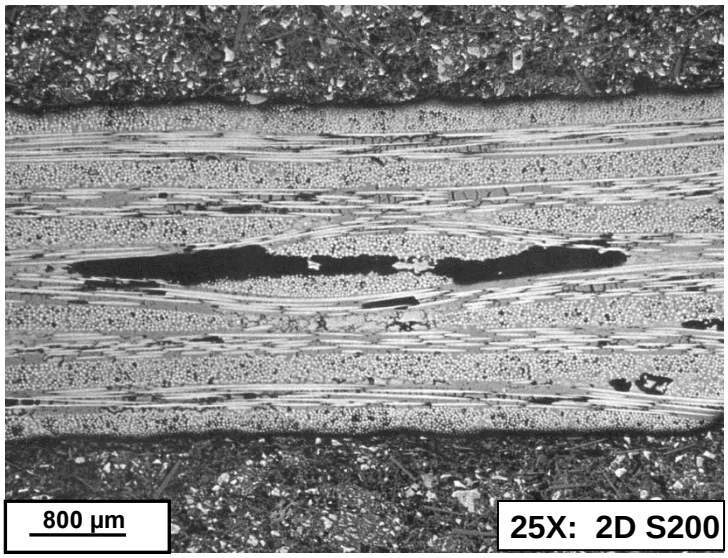


**Figure A-1.1.2: Micrograph of 2-D S200, 80 mil @ 25x, AB.** 2-D material system with Stringer type porosity.

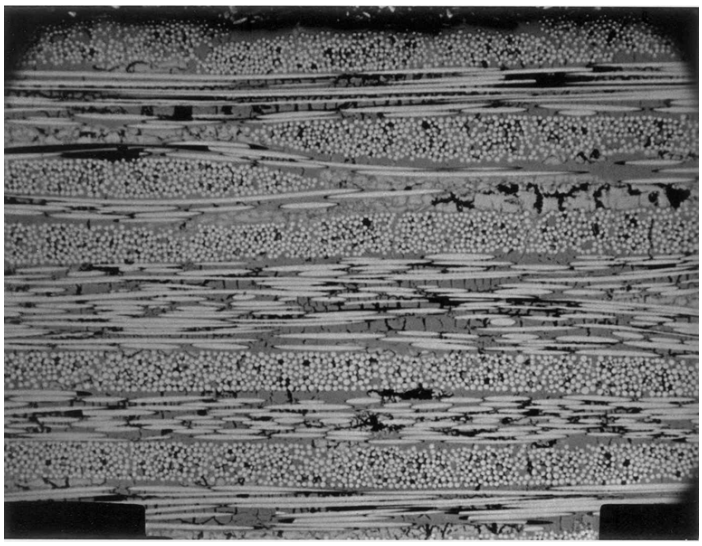

**Figure A-1.1.3: Micrograph of 2-D S200, 80 mil @ 50x, AB**. This figure illustrates the excellent infiltration of fiber tows in the 2-D material.

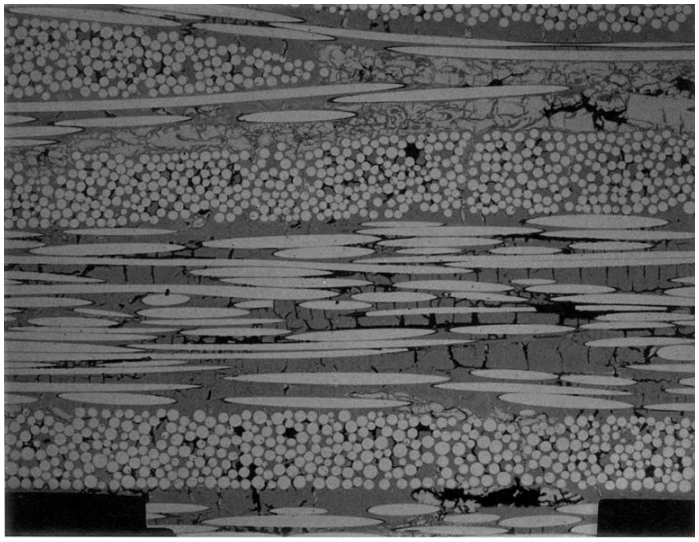

**Figure A-1.1.4: Micrograph of 2-D S200, 80 mil @ 100x, AB**

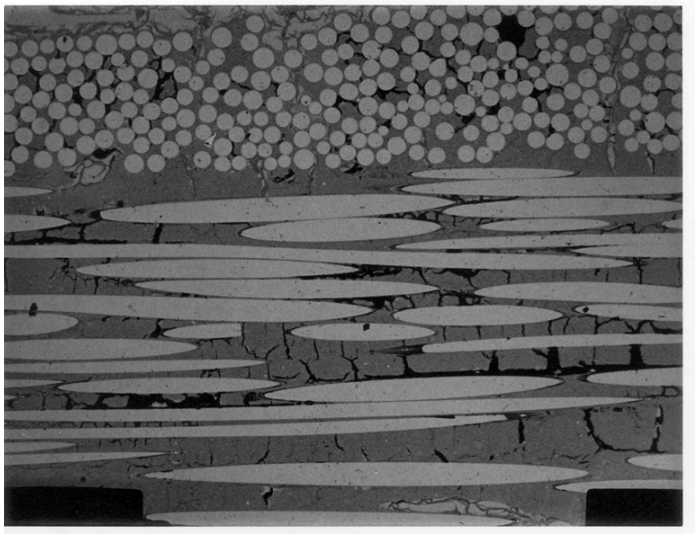

**Figure A-1.1.5: Micrograph of 2-D S200, 80 mil @ 200x, AB**

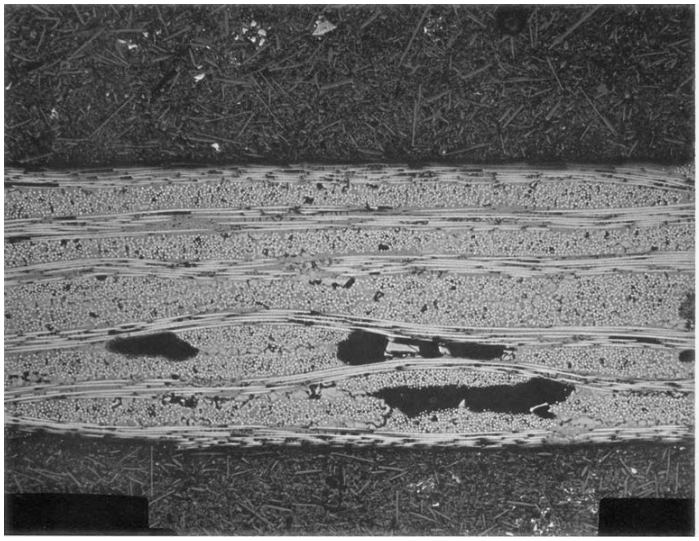

**Figure A-1.1.6: Micrograph of 2-D S200, 80 mil @ 25x, CD cut**

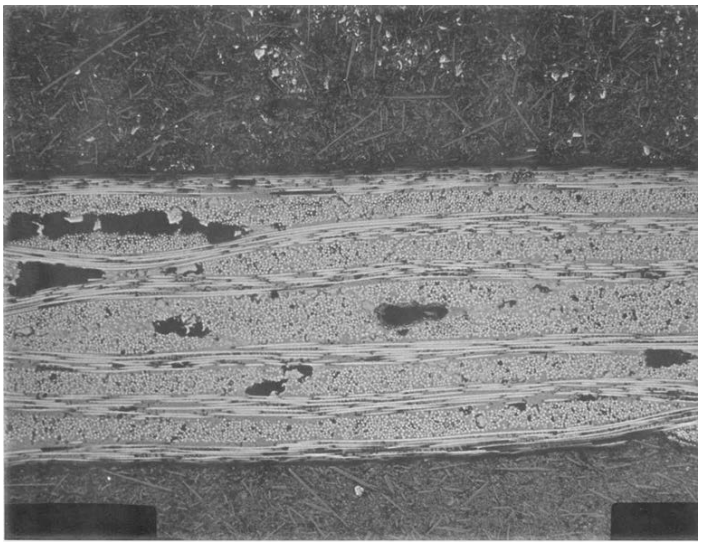

**Figure A-1.1.7: Micrograph of 2-D S200, 80 mil @ 25x, CD**

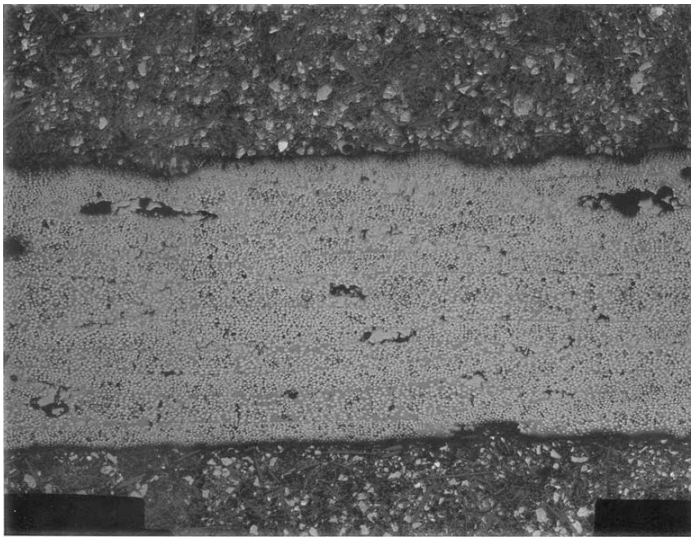

**Figure A-1.1.8: Micrograph of 2-D S200, 80 mil @ 25x, EF**

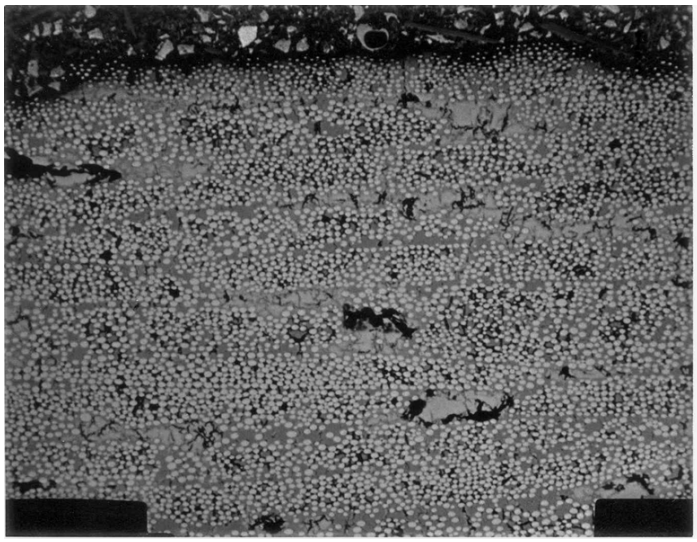

**Figure A-1.1.9: Micrograph of 2-D S200, 80 mil @ 50x, EF**

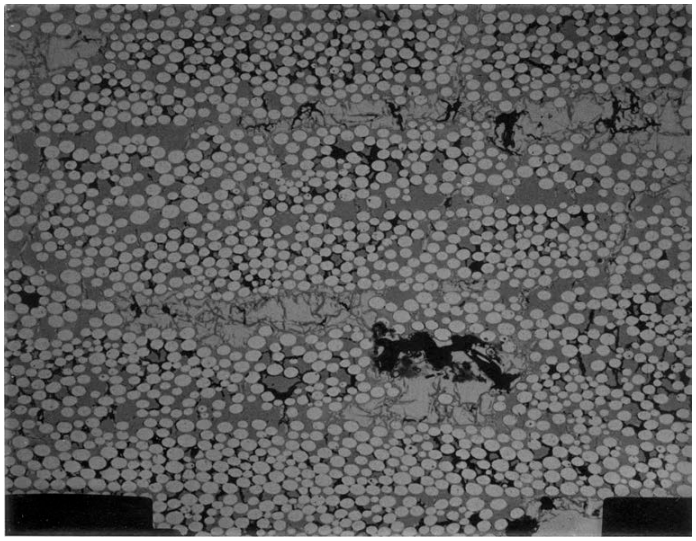

**Figure A-1.1.10: Micrograph of 2-D S200, 80 mil @ 100x, EF**

## A-2 3-D, S200-1, 80 MIL

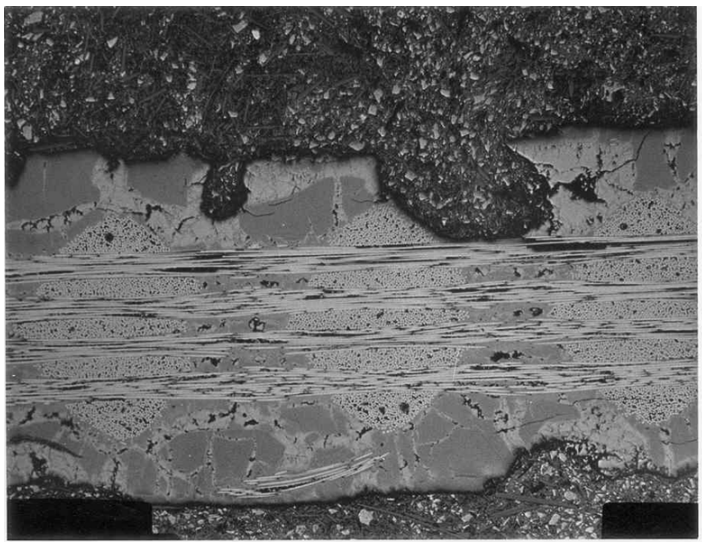

**Figure A-2.1.1: Micrograph of 3-D S200, 80 mil @ 25x, AB**

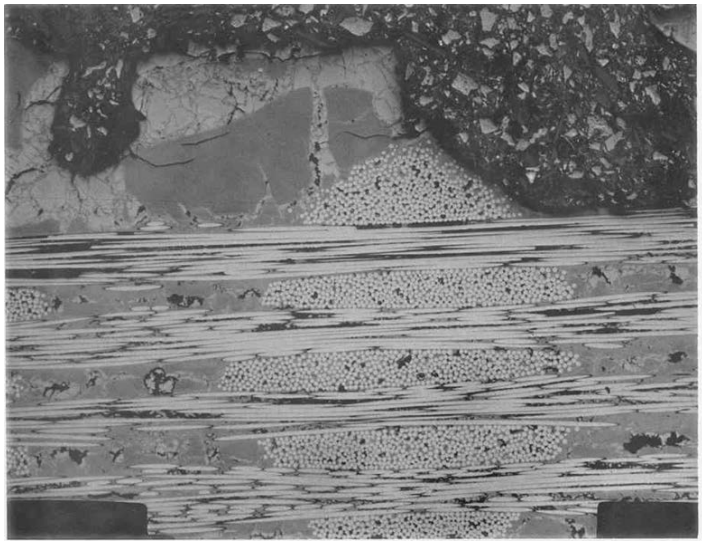

**Figure A-2.1.2: Micrograph of 3-D S200, 80 mil @ 50x, AB**

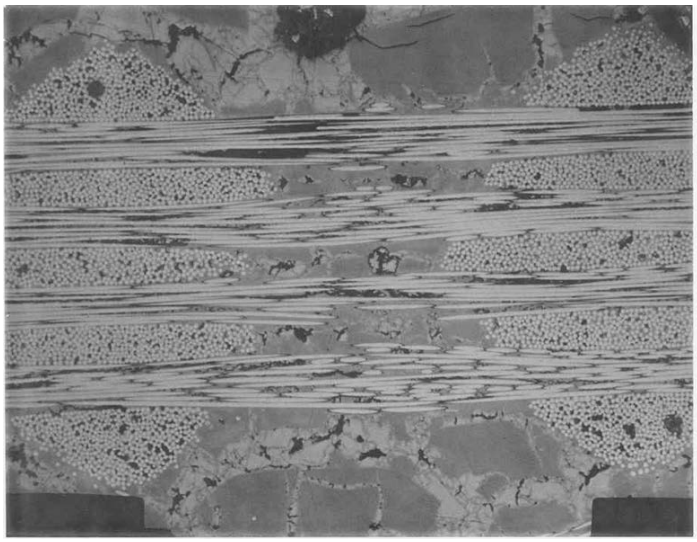

**Figure A-2.1.3: Micrograph of 3-D S200, 80 mil @ 50x, AB**

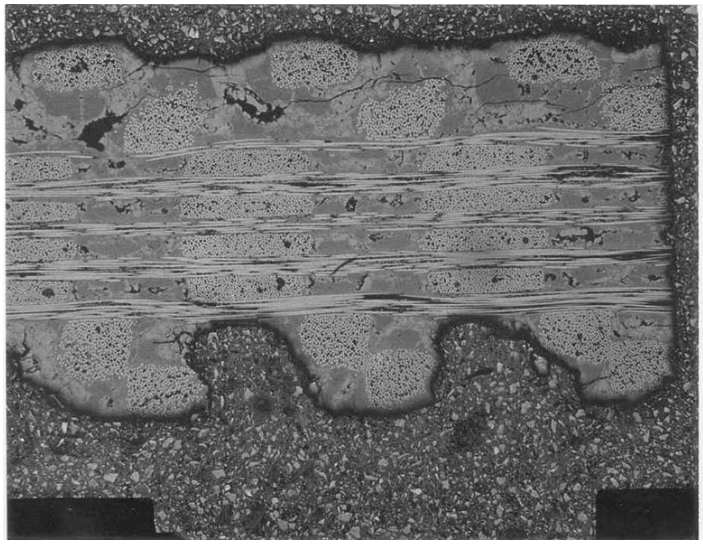

**Figure A-2.1.4: Micrograph of 3-D S200, 80 mil @ 25x, CD**

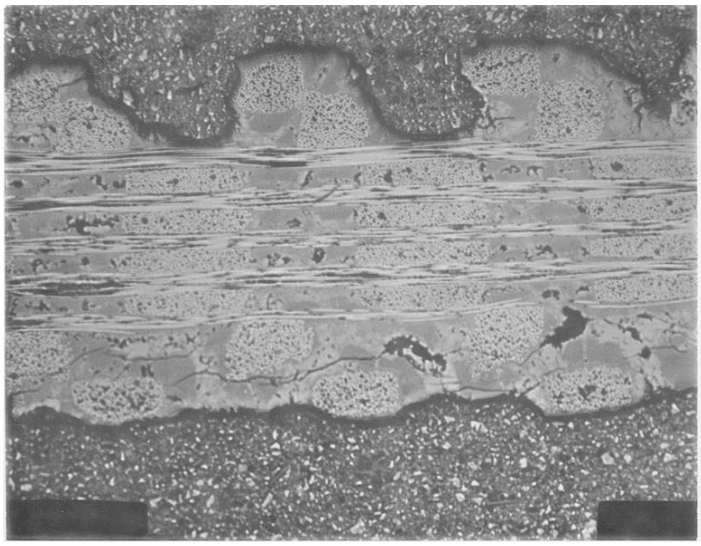

**Figure A-2.1.5: Micrograph of 3-D S200, 80 mil @ 25x, CD**

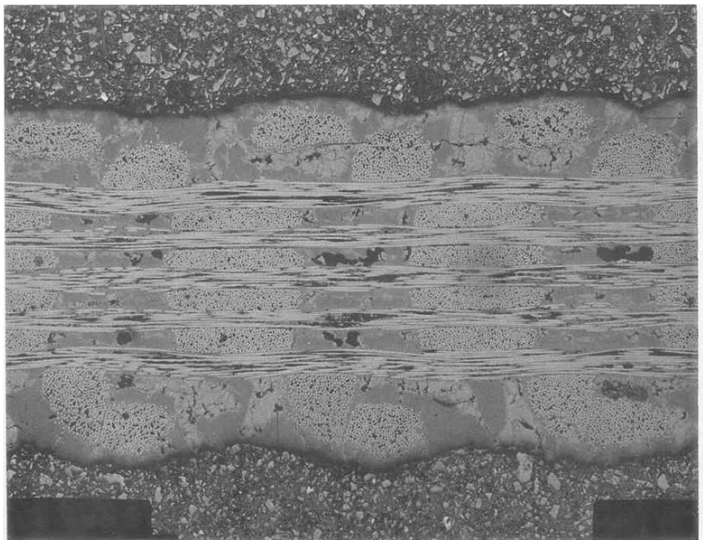

**Figure A-2.1.6: Micrograph of 3-D S200, 80 mil @ 25x, CD**

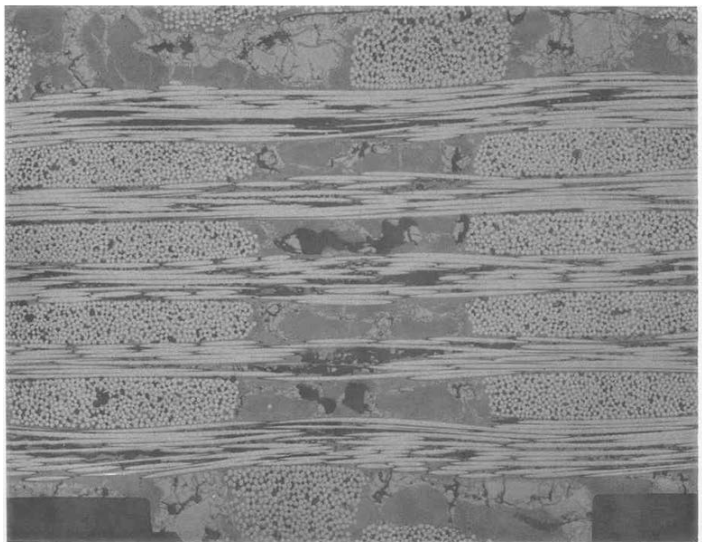

**Figure A-2.1.7: Micrograph of 3-D S200, 80 mil @ 50x, CD**

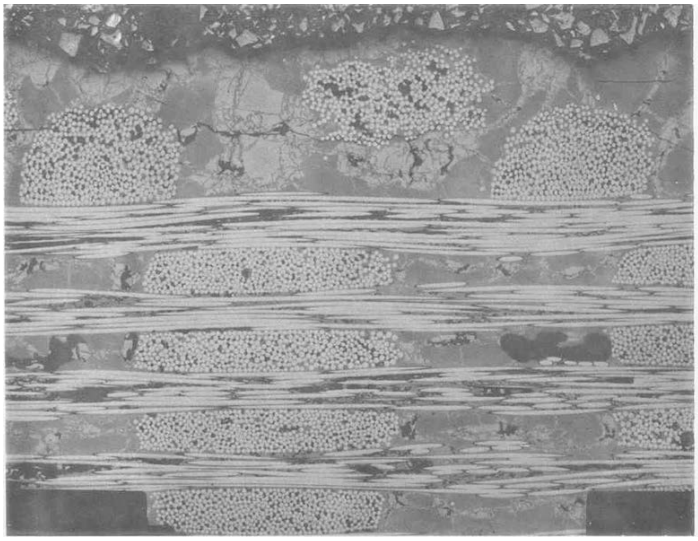

**Figure A-2.1.8: Micrograph of 3-D S200, 80 mil @ 50x, CD**

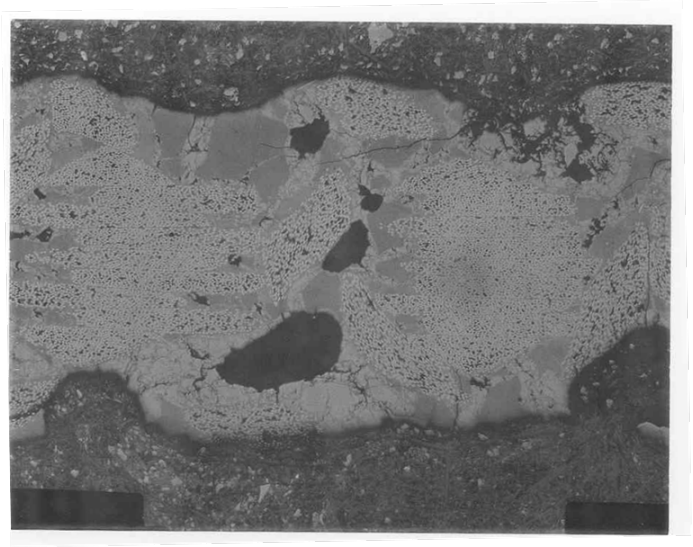

**Figure A-2.1.9: Micrograph of 3-D S200, 80 mil @ 25x, EF**

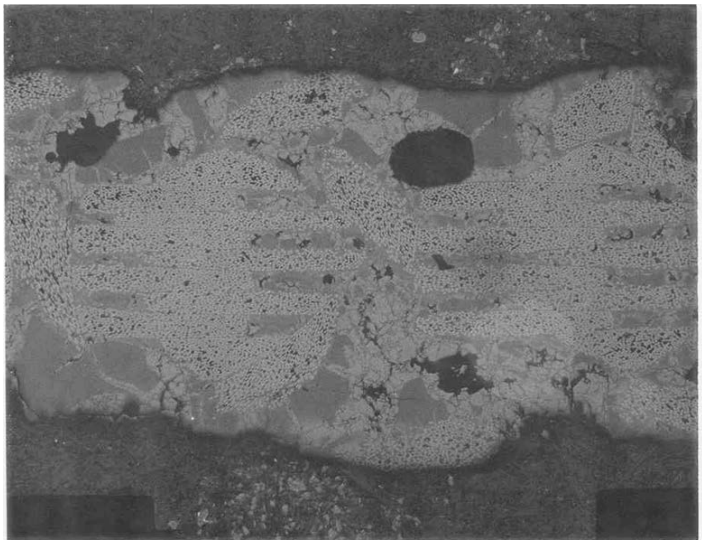

**Figure A-2.1.10: Micrograph of 3-D S200, 80 mil @ 25x, EF**

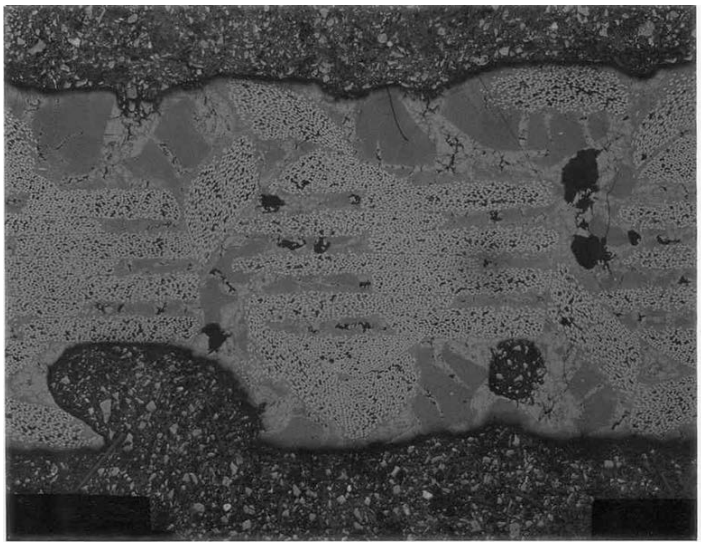

**Figure A-2.1.11: Micrograph of 3-D S200, 80 mil @ 25x, EF**

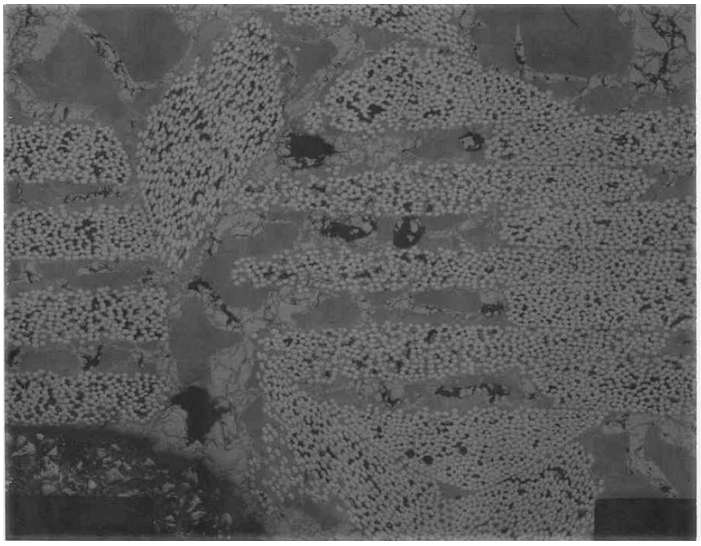

**Figure A-2.1.11: Micrograph of 3-D S200, 80 mil @ 50x, CD**

## A-3 3-D, S200-1, 145 MIL

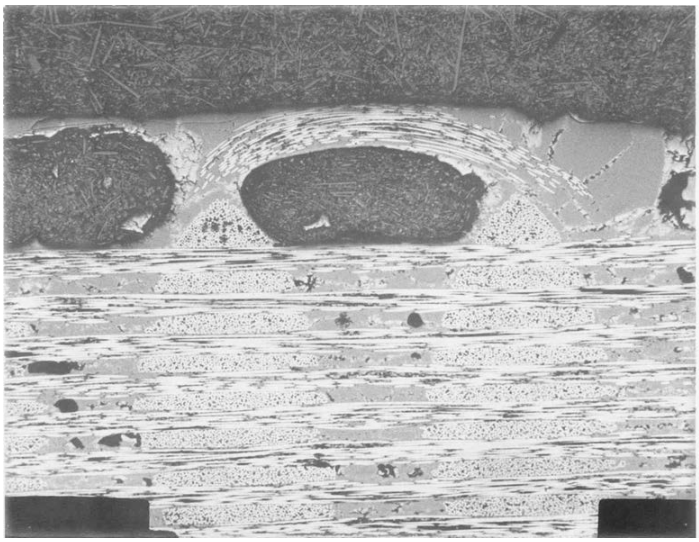

**Figure A-3.1.1: Micrograph of 3-D S200, 145 mil @ 25x, AB**

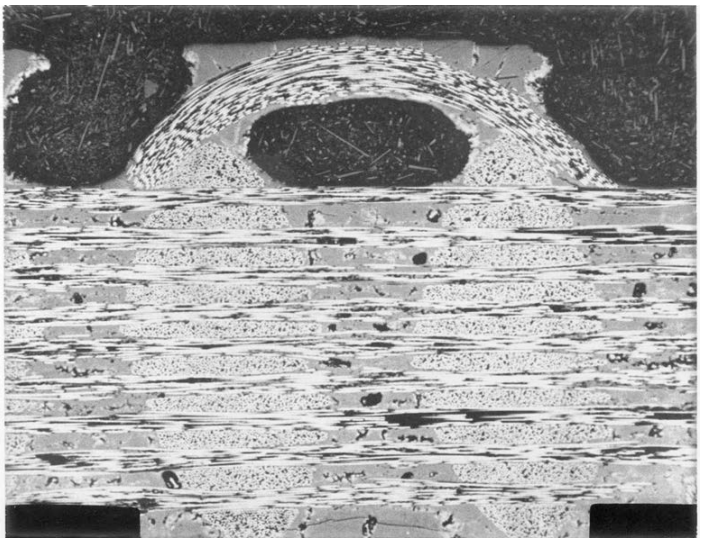

**Figure A-3.1.2: Micrograph of 3-D S200, 145 mil @ 25x, AB**

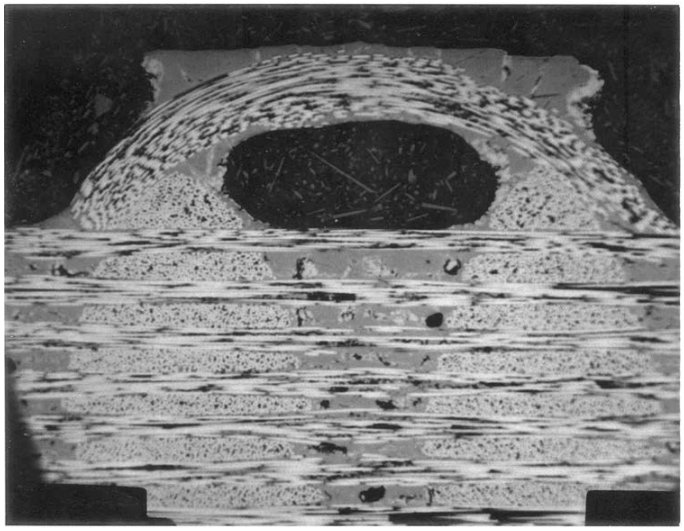

**Figure A-3.1.3: Micrograph of 3-D S200, 145 mil @ 50x, AB**

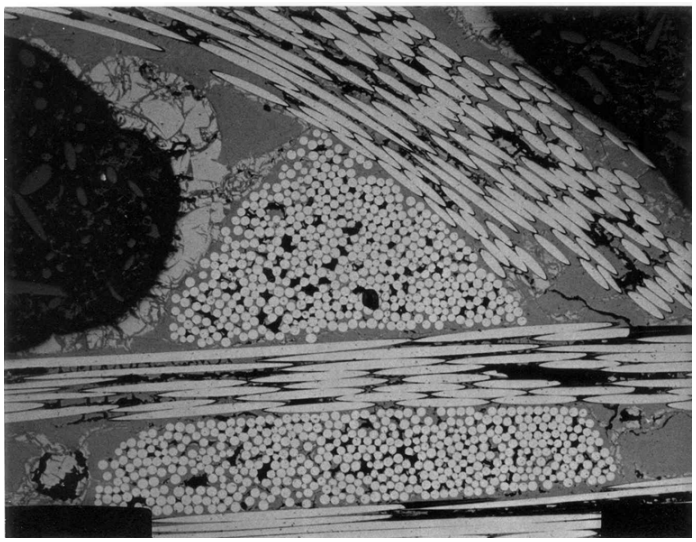

**Figure A-3.1.4: Micrograph of 3-D S200, 145 mil @ 100x, AB**

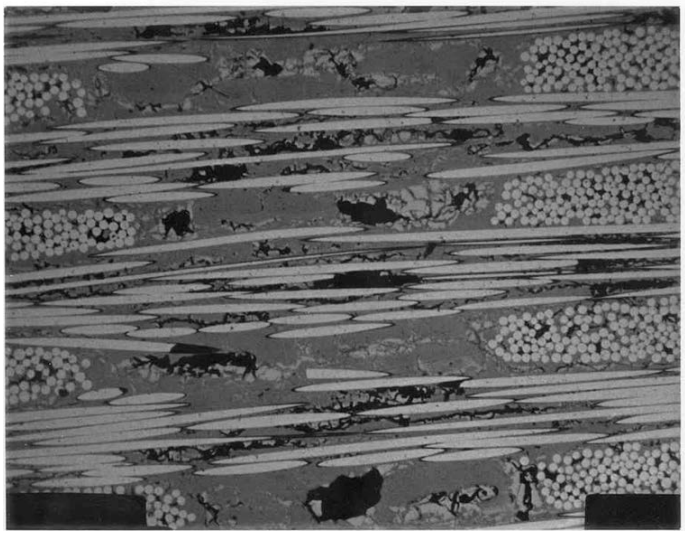

**Figure A-3.1.5: Micrograph of 3-D S200, 145 mil @ 100x, AB**

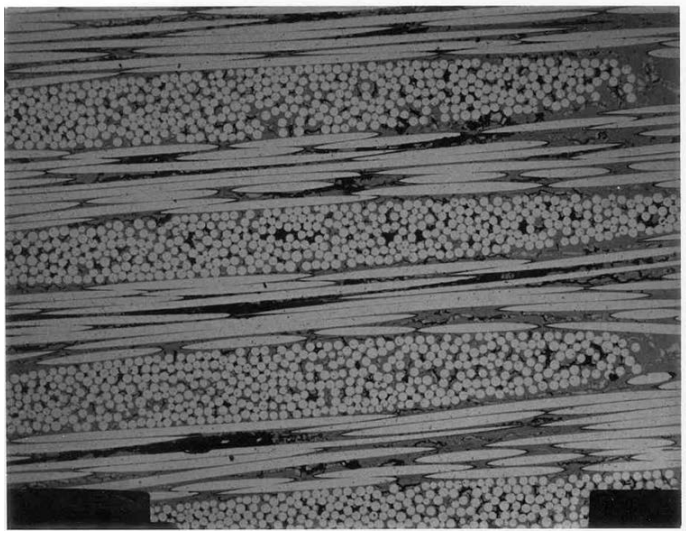

**Figure A-3.1.6: Micrograph of 3-D S200, 145 mil @ 100x, AB**

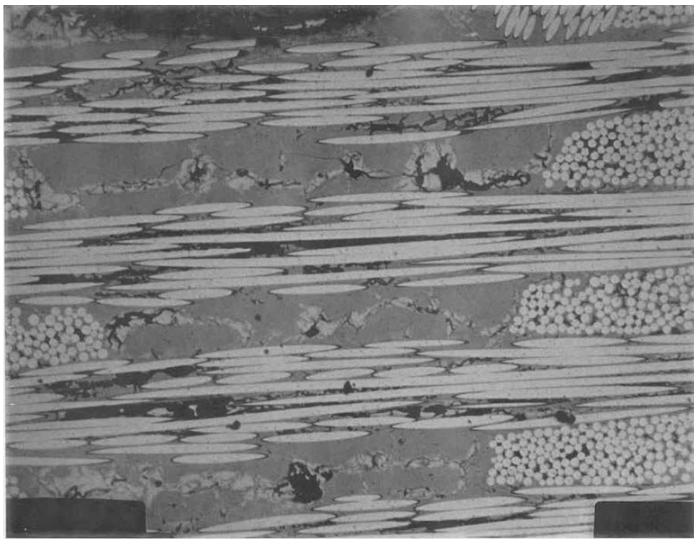

**Figure A-3.1.7: Micrograph of 3-D S200, 145 mil @ 100x, AB**

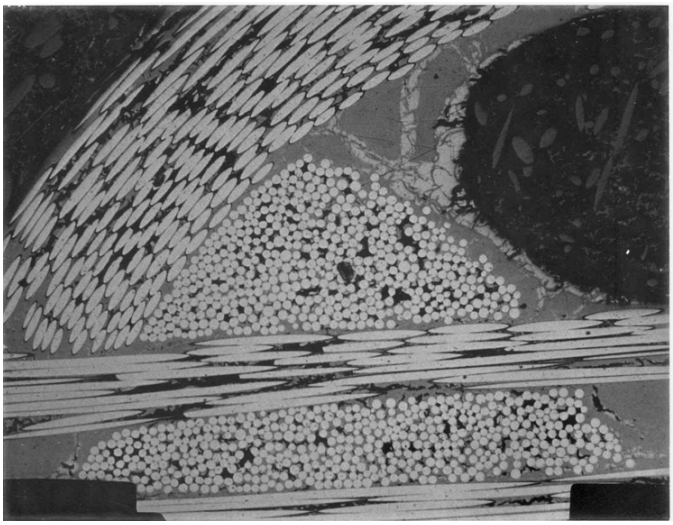

**Figure A-3.1.8: Micrograph of 3-D S200, 145 mil @ 100x, AB**

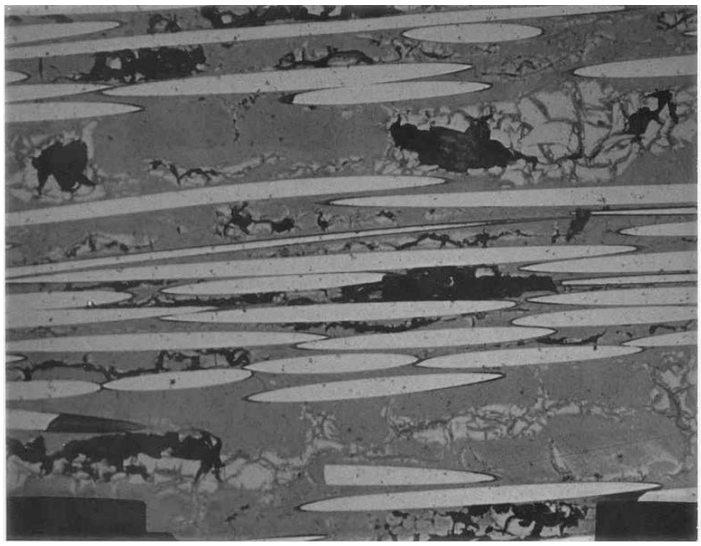

**Figure A-3.1.9: Micrograph of 3-D S200, 145 mil @ 200x, AB**

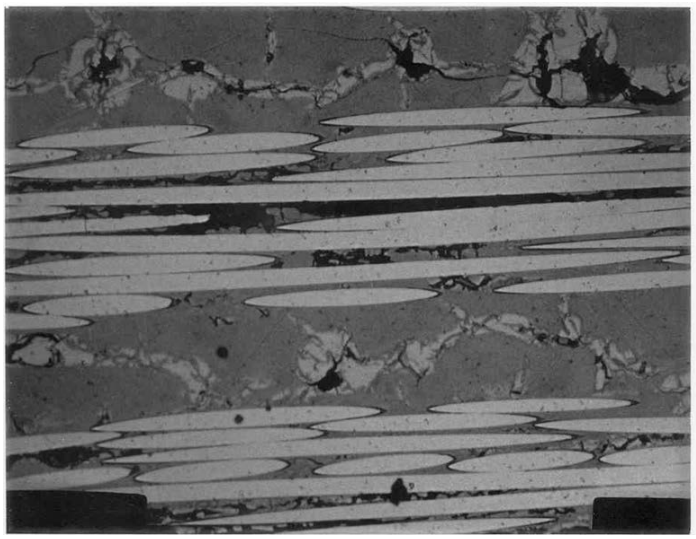

**Figure A-3.1.10: Micrograph of 3-D S200, 145 mil @ 200x, AB**

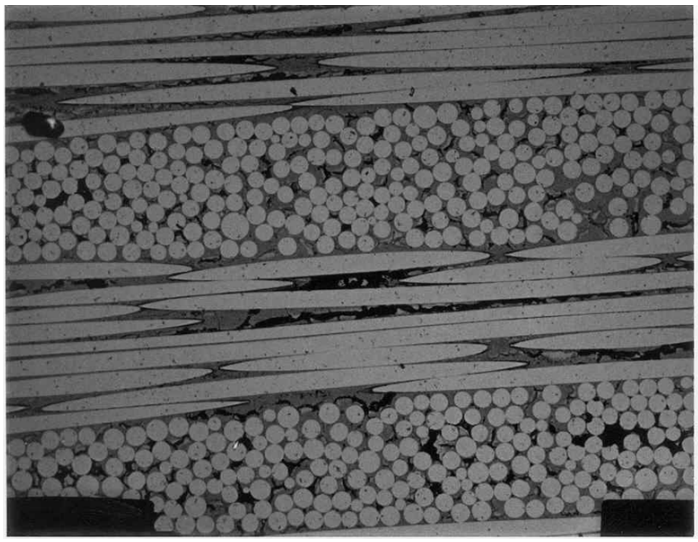

**Figure A-3.1.11: Micrograph of 3-D S200, 145 mil @ 200x, AB**

**Figure A-3.1.12: Micrograph of 3-D S200, 145 mil @ 20x, EF**

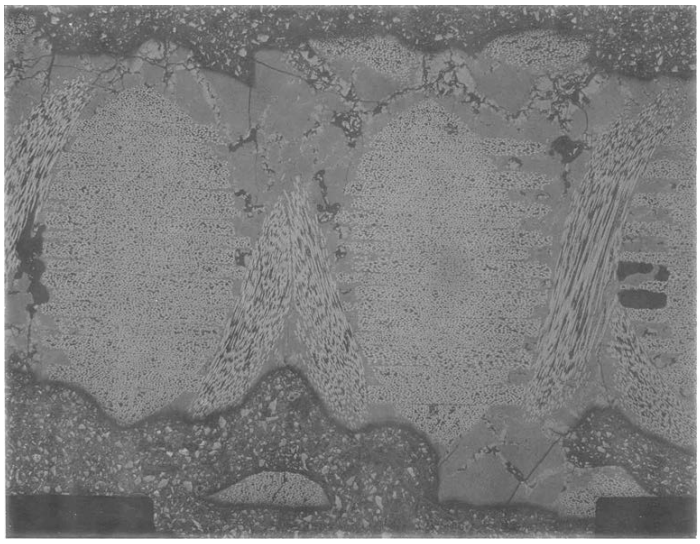

**Figure A-3.1.13: Micrograph of 3-D S200, 145 mil @ 20x, EF**

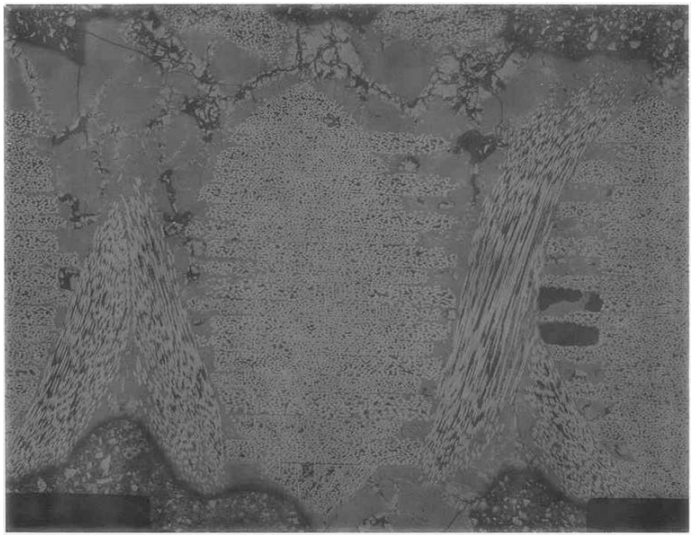

**Figure A-3.1.14: Micrograph of 3-D S200, 145 mil @ 25x, EF**

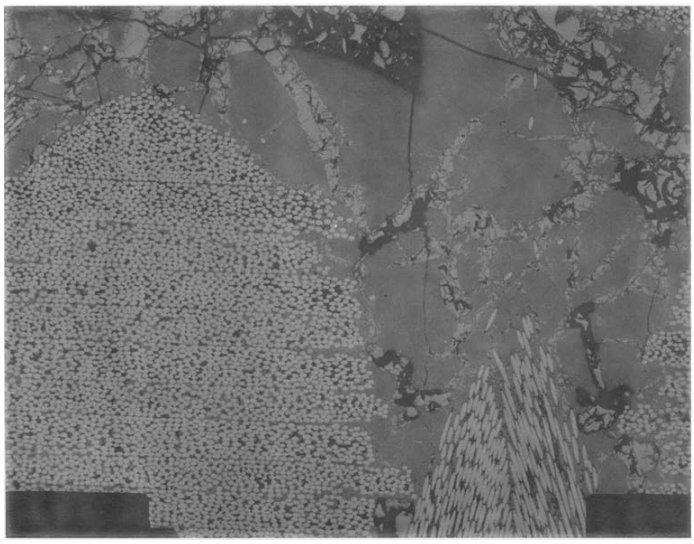

**Figure A-3.1.15: Micrograph of 3-D S200, 145 mil @ 50x, EF**

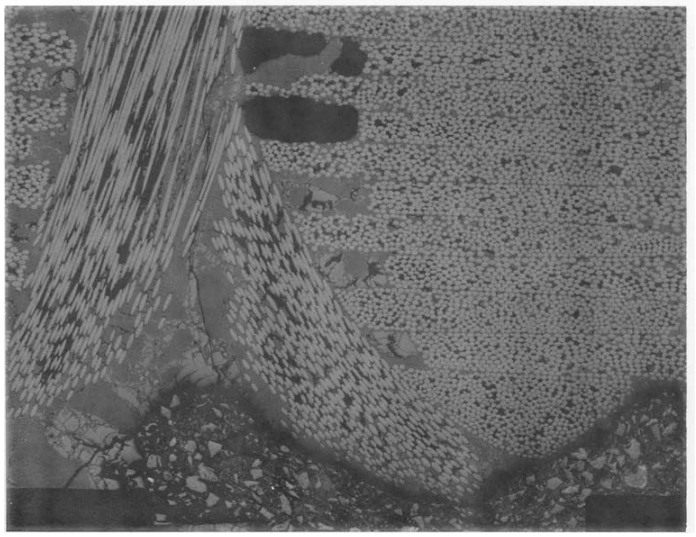

**Figure A-3.1.16: Micrograph of 3-D S200, 145 mil @ 20x, EF**

## A-4 3-D, STARFIRE, 80 MIL

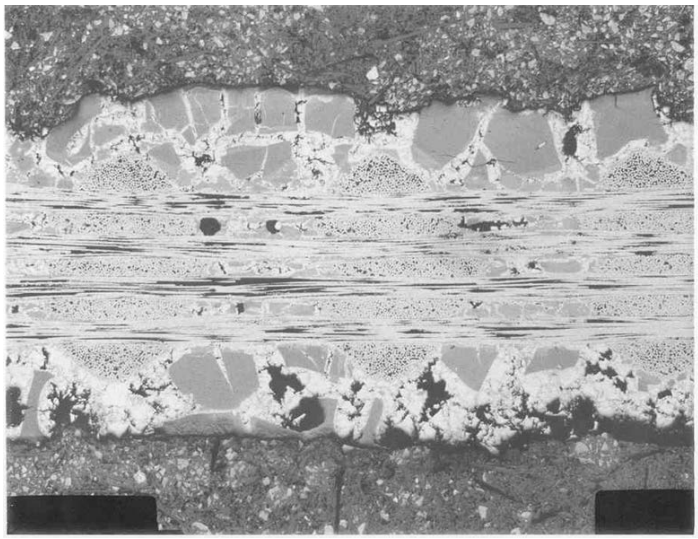

**Figure A-4.1.1: Micrograph of 3-D Starfire, 80 mil @ 25x, AB**

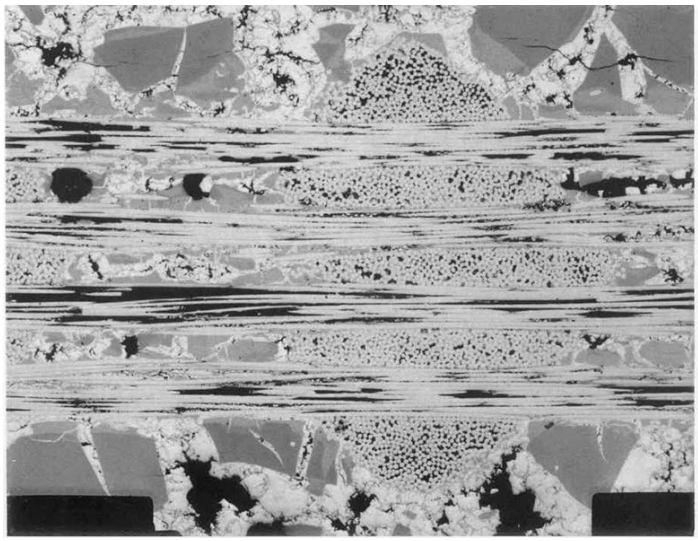

**Figure A-4.1.2: Micrograph of 3-D Starfire, 80 mil @ 50x, AB**

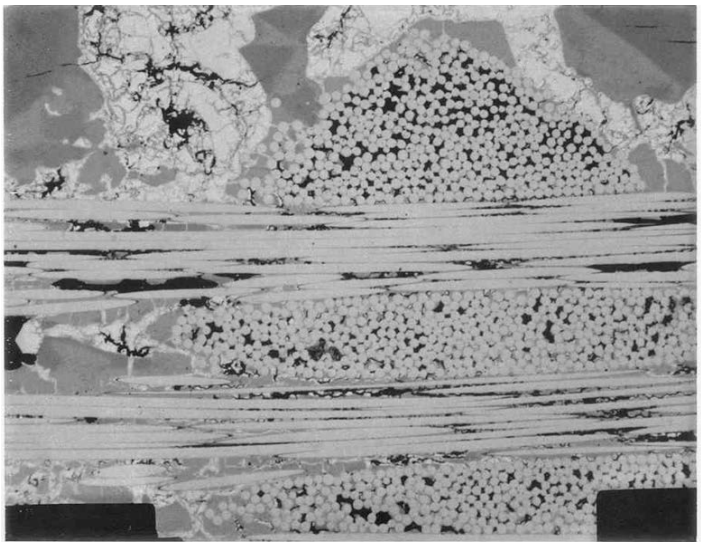

**Figure A-4.1.3: Micrograph of 3-D Starfire, 80 mil @ 100x, AB**

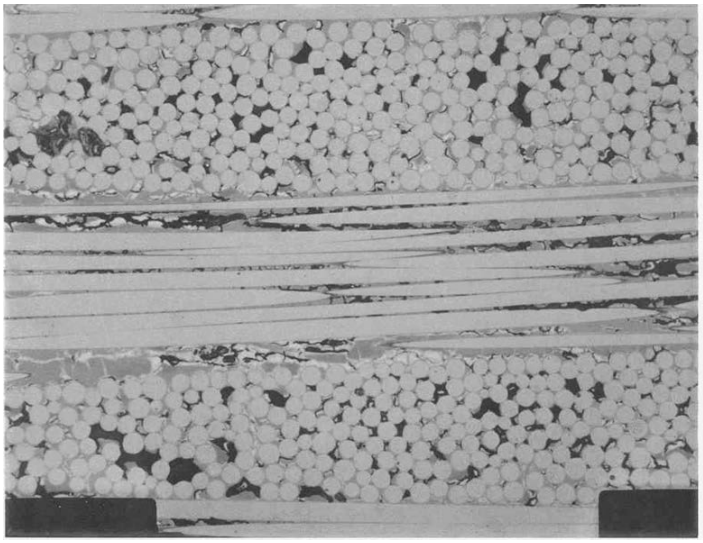

**Figure A-4.1.4: Micrograph of 3-D Starfire, 80 mil @ 200x, AB**

## A-5 3-D, STARFIRE, 80 MIL

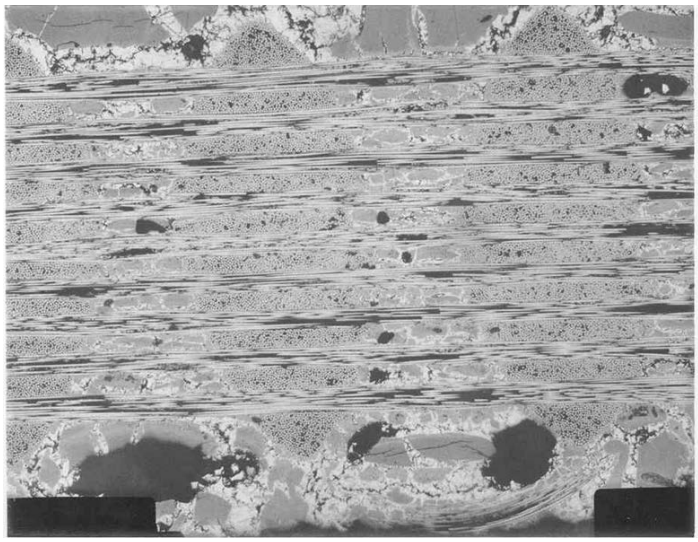

**Figure A-5.1.1: Micrograph of 3-D Starfire, 145 mil @ 25x, AB**

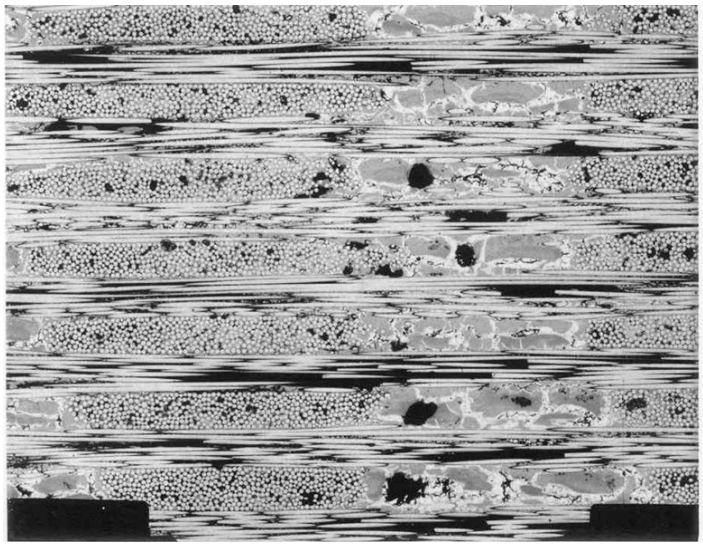

**Figure A-5.1.2: Micrograph of 3-D Starfire, 145 mil @ 50x, AB**

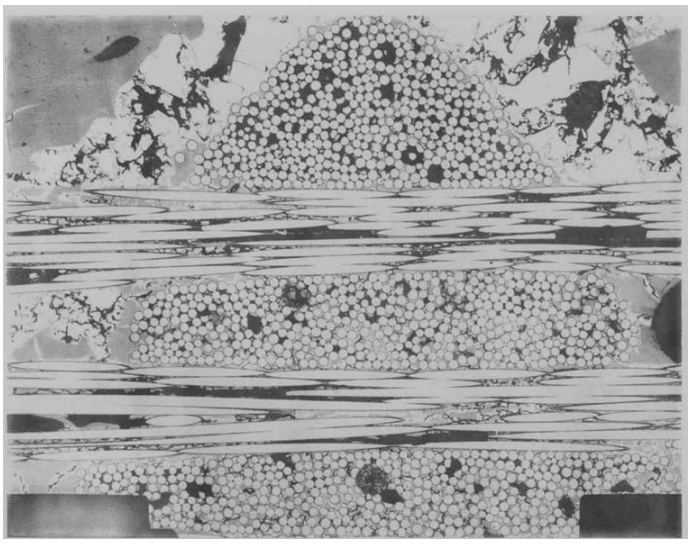

**Figure A-5.1.3: Micrograph of 3-D Starfire, 145 mil @ 100x, AB**

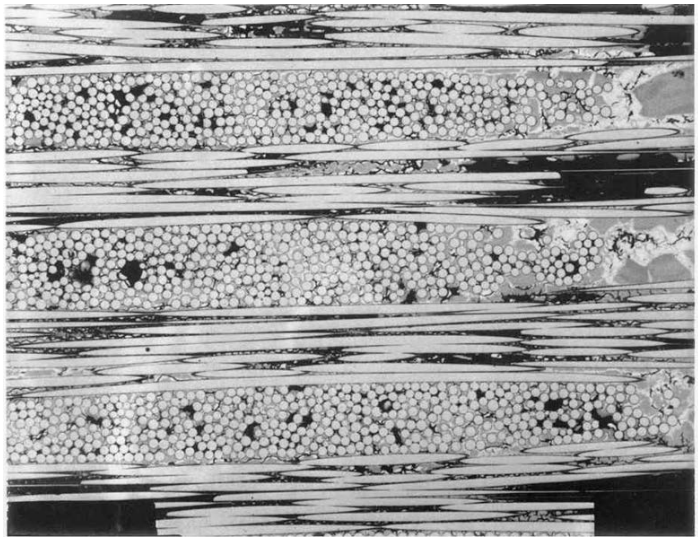

**Figure A-5.1.4: Micrograph of 3-D Starfire, 145 mil @ 100x, AB**

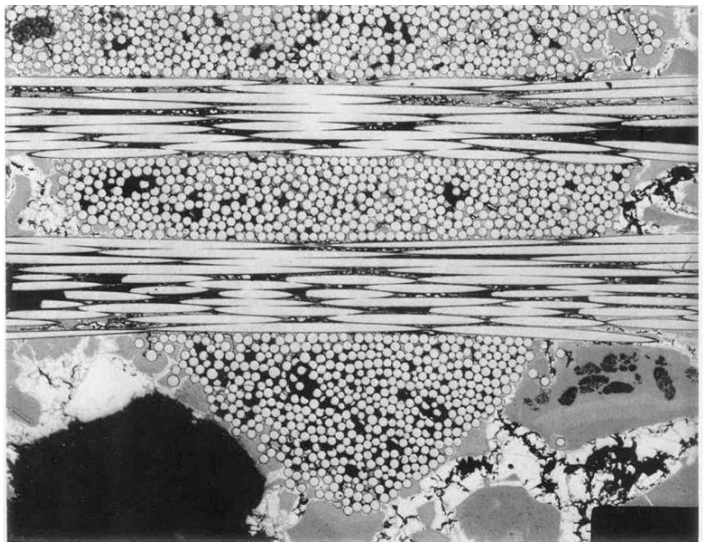

**Figure A-5.1.5: Micrograph of 3-D Starfire, 145 mil @ 100x, AB**

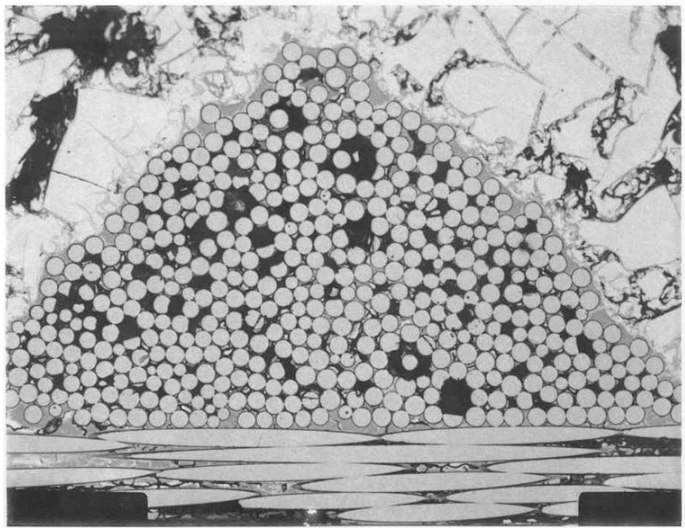

**Figure A-5.1.6: Micrograph of 3-D Starfire, 145 mil @ 200x, AB**

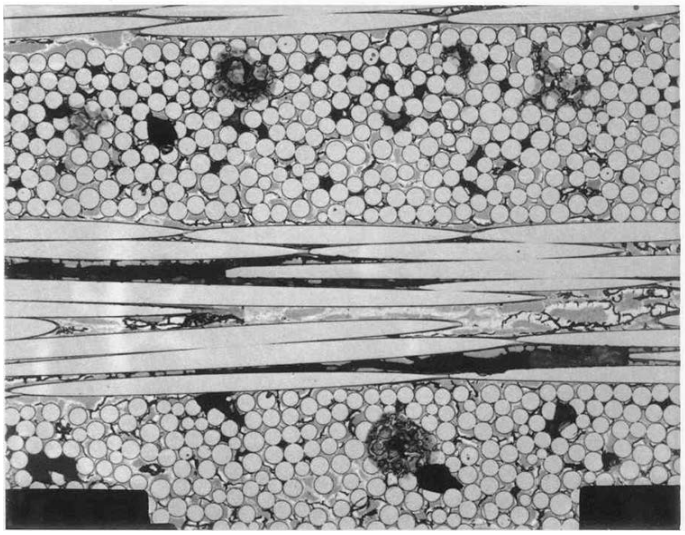

**Figure A-5.1.7: Micrograph of 3-D Starfire, 145 mil @ 200x, AB**

# APPENDIX B

## B-1 FRACTURED SURFACE

### B-1.1 2-D S200-1

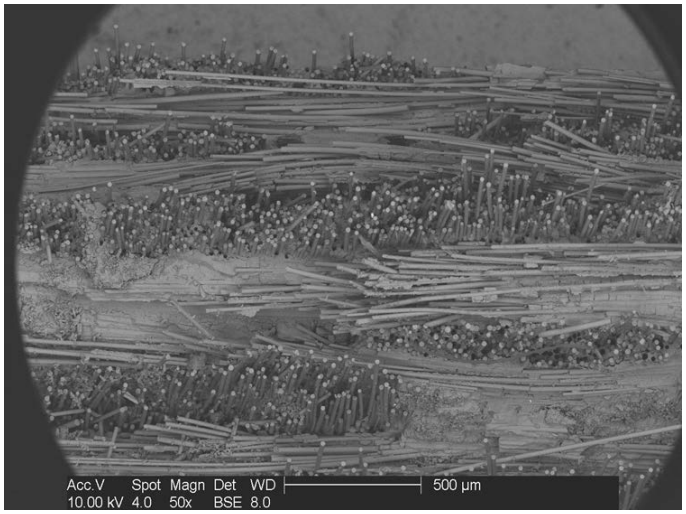


**Figure B-1.1.1: SEM Image of 2-D S200, 80 mil @ 50x**. This image shows excellent fiber pullout which attest to its strength.

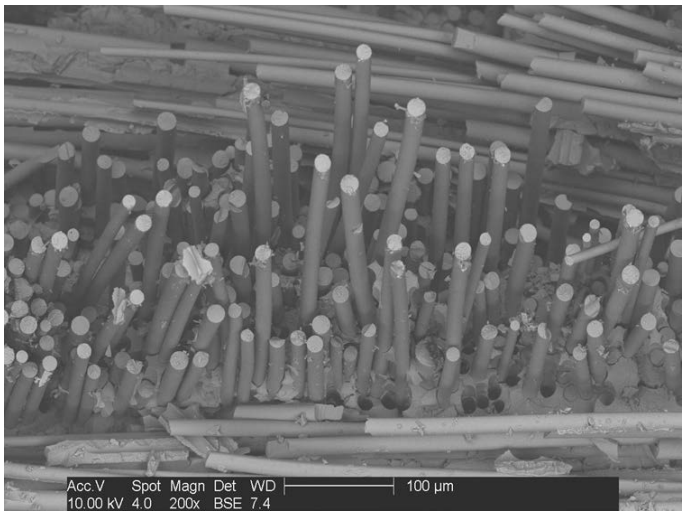


**Figure B-1.1.2: SEM Image of 2-D S200, 80 mil @ 200x**. A closer look at the fiber pullout in both the fill and tow fibers.

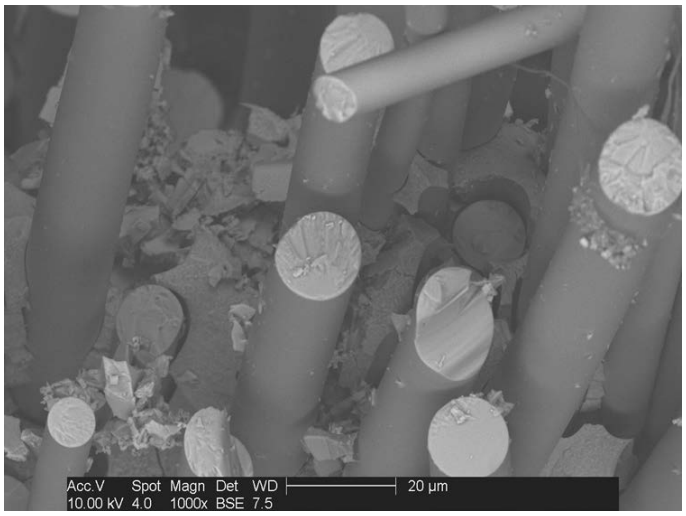


**Figure B-1.1.3: SEM Image of 2-D S200, 80 mil @ 1000x**. Nice, smooth fractured surface with good separation.

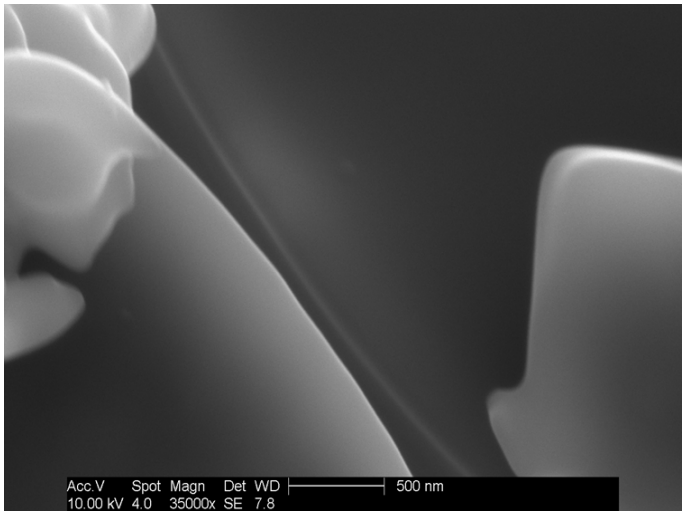


**Figure B-1.1.4: SEM Image of 2-D S200, 80 mil @ 35kx**. Shows that the fibers are not bonded together.

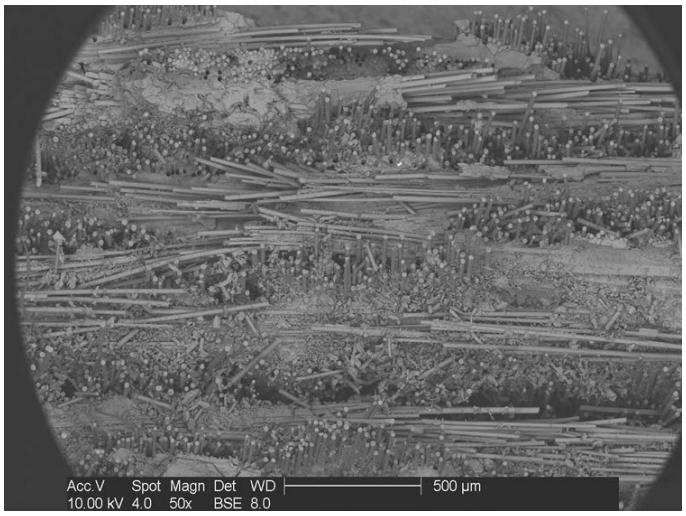


**Figure B-1.1.5: SEM Image of 2-D S200, 80 mil @ 50x.** Good fiber pull out.

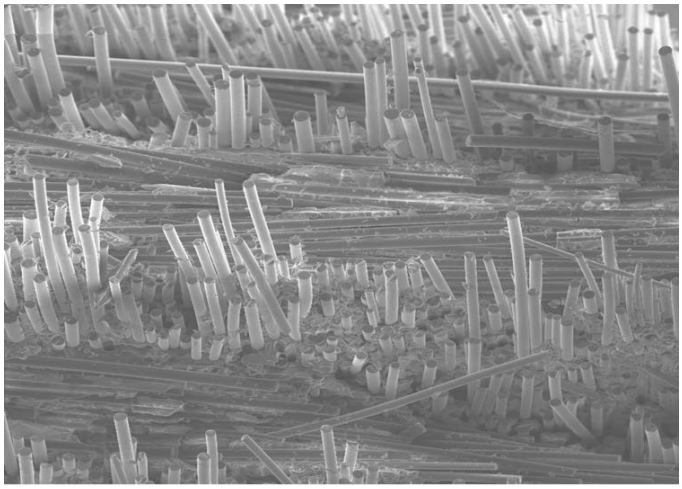

**Figure B-1.1.6: SEM Image of 2-D S200, 80 mil @ 150x**. Good fiber pullout.

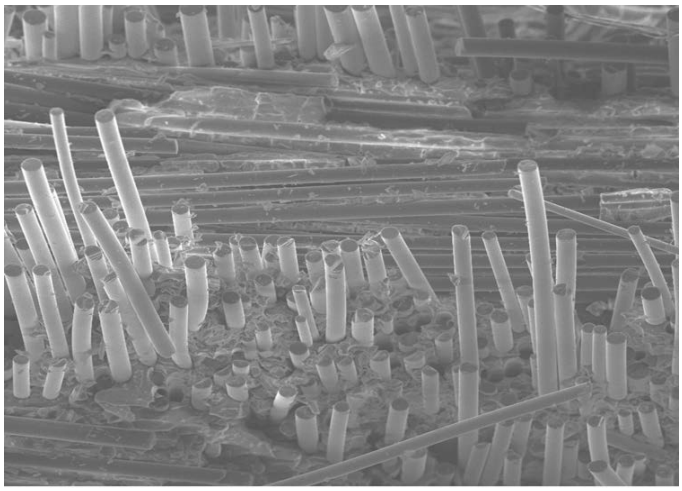

**Figure B-1.1.7: SEM Image of 2-D S200, 80 mil @ 240x**

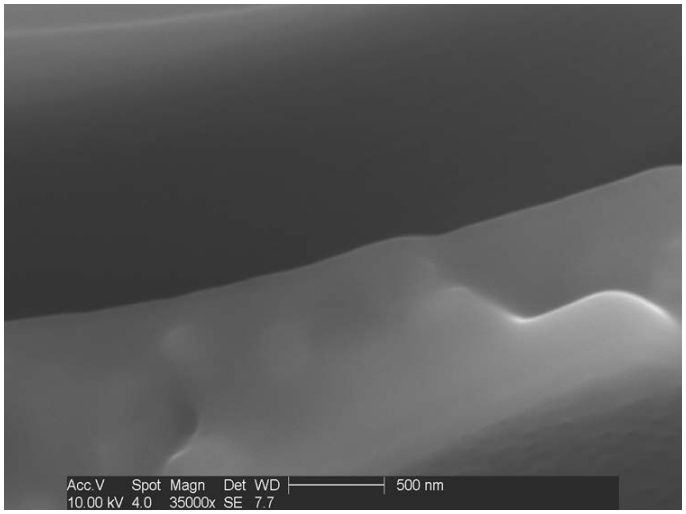


**Figure B-1.1.8: SEM Image of 2-D S200, 80 mil @ 35kx**. This image shows some spacing between the fiber and the matrix.

## B-1.2 3-D S200-1, 80 MIL

## B-1.3 3-D S200-1, 145 MIL

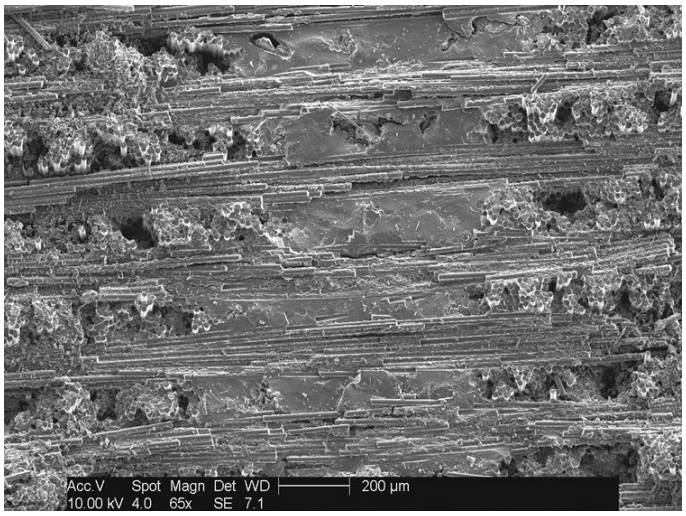


**Figure B-1.3.1: SEM Image of 3-D S200, 145 mil @ 50x**. This image shows that the fibers failed in same plane.

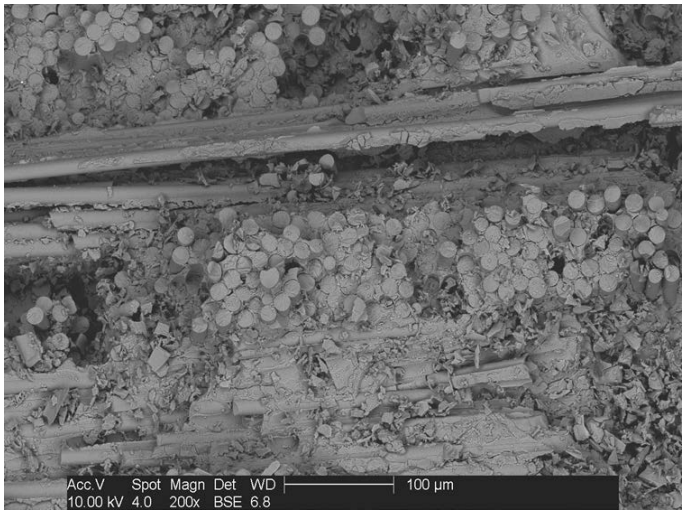


**Figure B-1.3.2: SEM Image of 3-D S200, 145 mil @ 200x**. Very poor fracture pullout; all fibers failed in same plane.

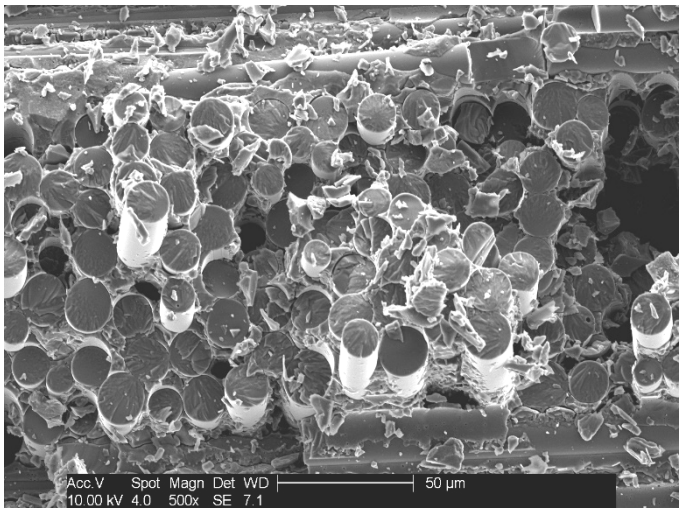


**Figure B-1.3.3: SEM Image of 3-D S200, 145 mil @ 500x**. Failure seem to be a step function…fibers failed in groups in the same plane.

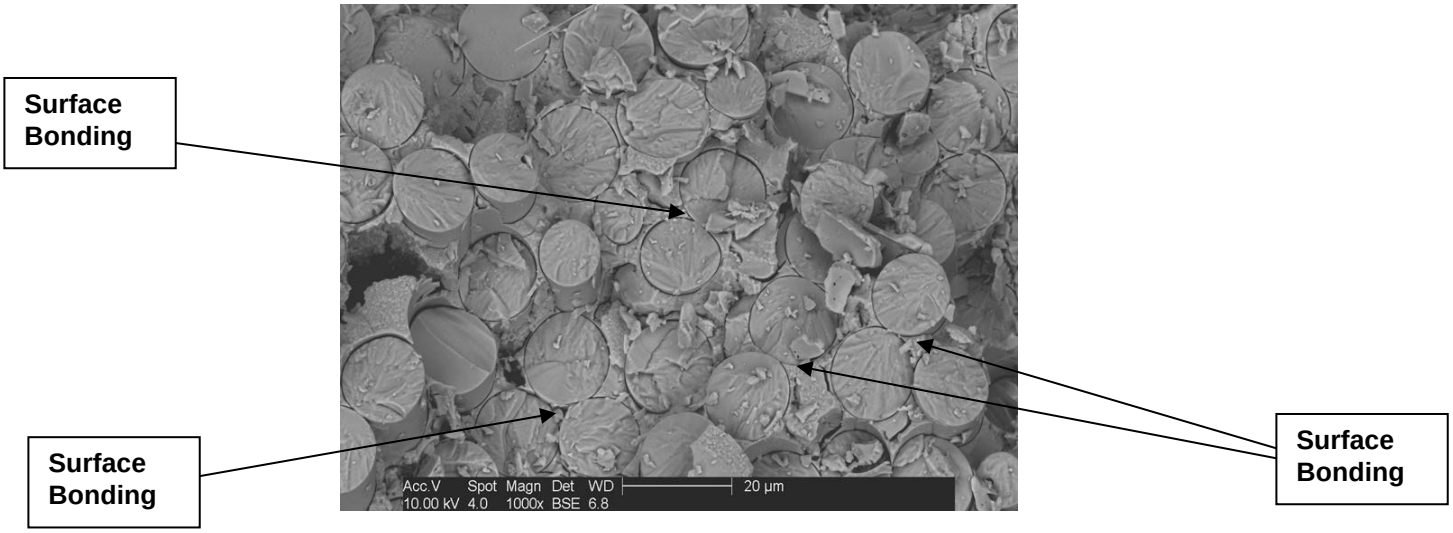


**Figure B-1.3.4: SEM Image of 3-D S200, 145 mil @ 1000x**. This image illustrate the surface bonding between fibers, which is one of the factors leading to low strength values for this material.

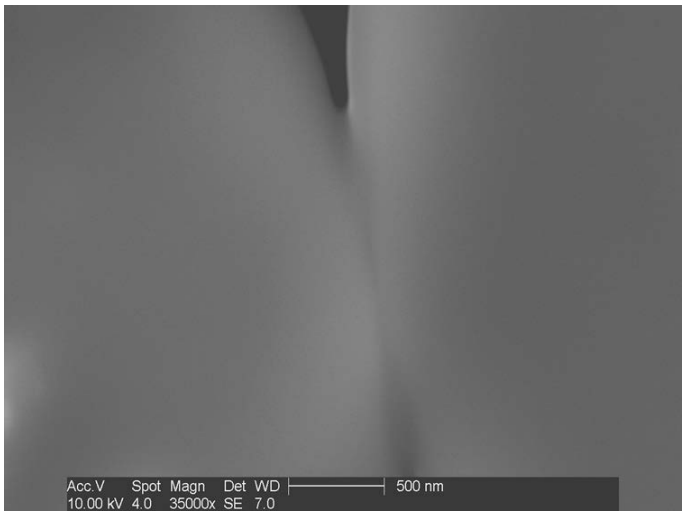


**Figure B-1.3.5: SEM Image of 3-D S200, 145 mil @ 35kx**. This image shows the surface bonding between the fibers.

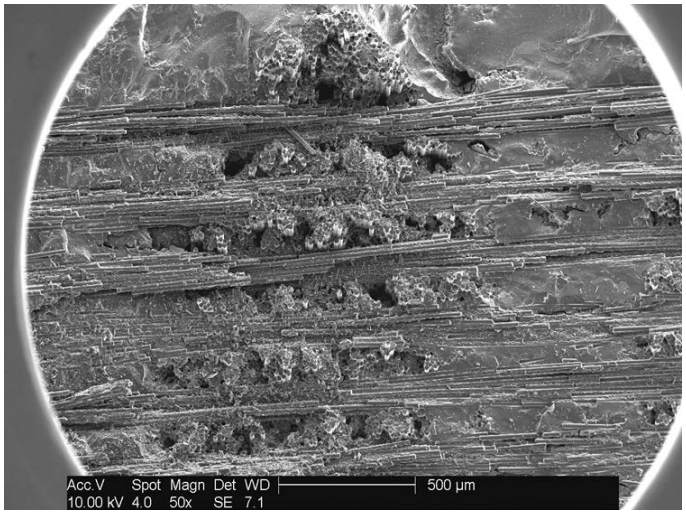


**Figure B-1.3.6: SEM Image of 3-D S200, 145 mil @ 50x**. Step function of fractured fibers gives the illusion of porosity in fill fibers.

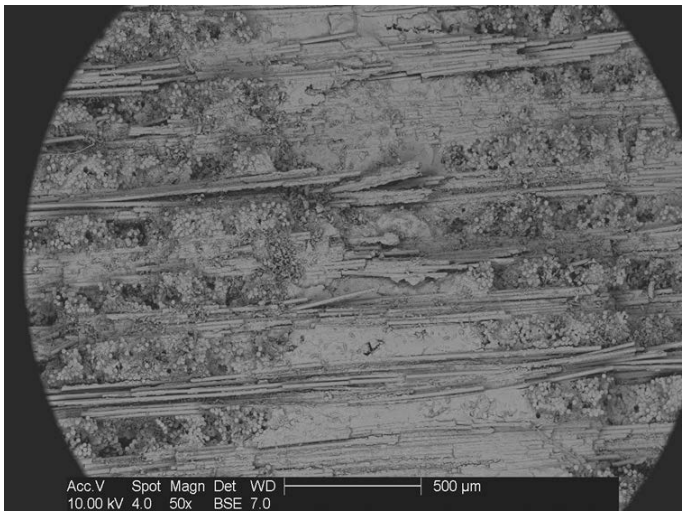


**Figure B-1.3.7: SEM Image of 3-D S200, 145 mil @ 50x**. Image of fractured surface showing both the fill and tow fibers.

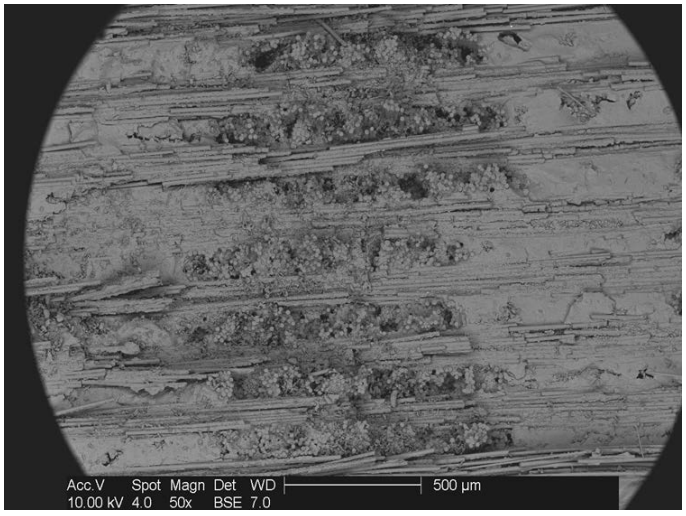


**Figure B-1.3.8: SEM Image of 3-D S200, 145 mil @ 50x**. Additional image of fractured surface showing fill and tow fibers.

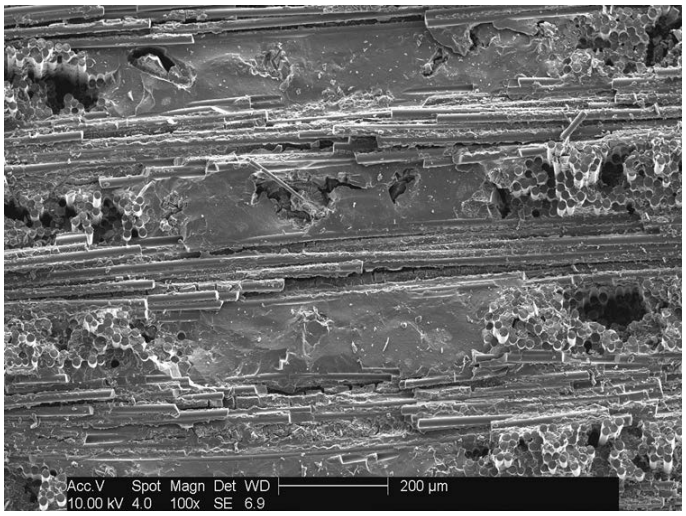


**Figure B-1.3.9: SEM Image of 3-D S200, 145 mil @ 100x**. Image illustrate step function of tensile failure exist in this material.

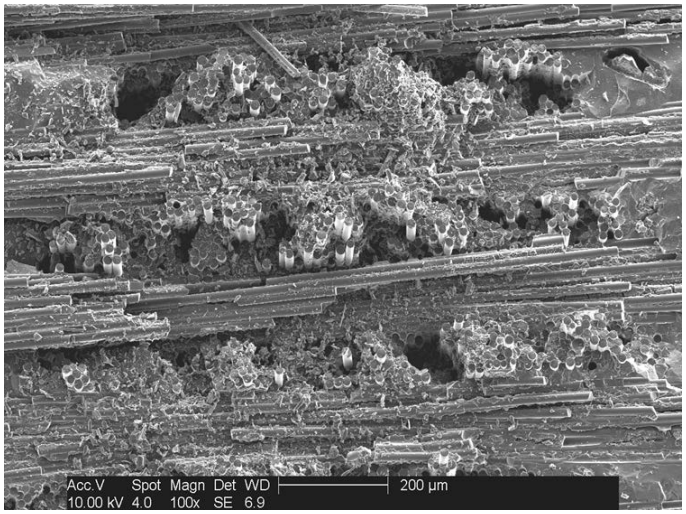


**Figure B-1.3.10: SEM Image of 3-D S200, 145 mil @ 100x**. Very little fiber pullout…fibers fractured in groups (step function). This characteristics contributes to its poor strength values.

## B-1.4 3-D STARFIRE, 80 MIL

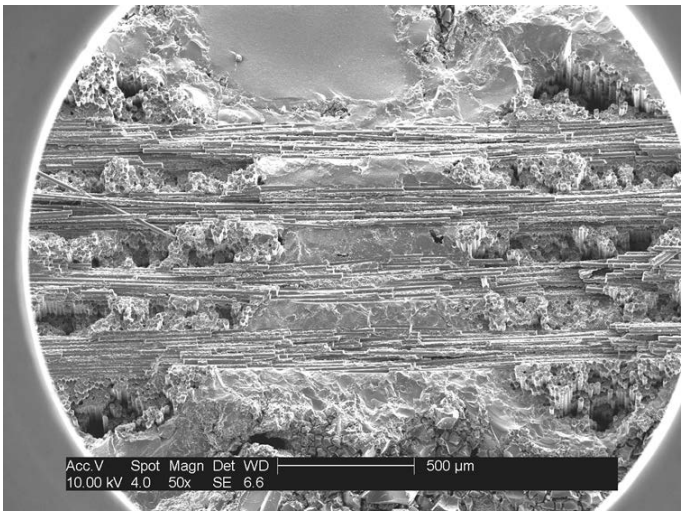


**Figure B-1.4.1: SEM Image of 3-D Starfire, 80 mil @ 50x**. Image of fractured surface showing fill and tow fibers.

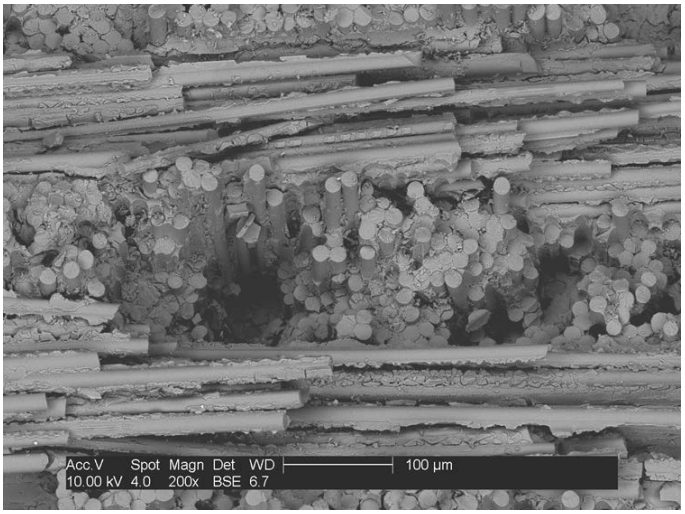


**Figure B-1.4.2: SEM Image of 3-D Starfire, 80 mil @ 200x**. Poor fiber pull out.

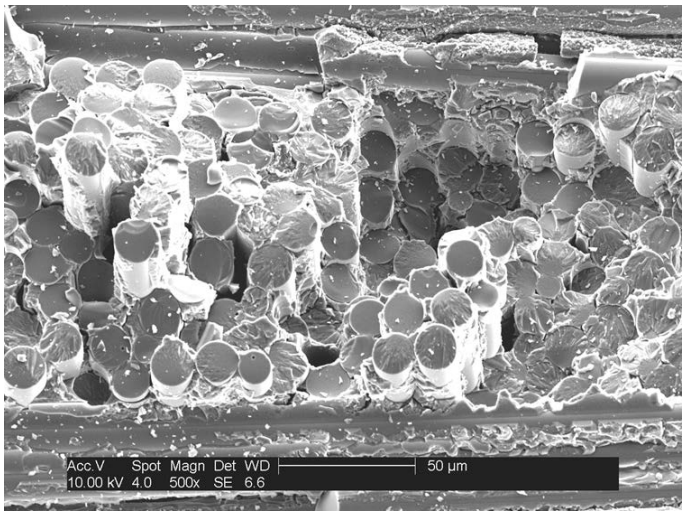


**Figure B-1.4.3: SEM Image of 3-D Starfire, 80 mil @ 500x.** Image shows the step function in the fractured surface.

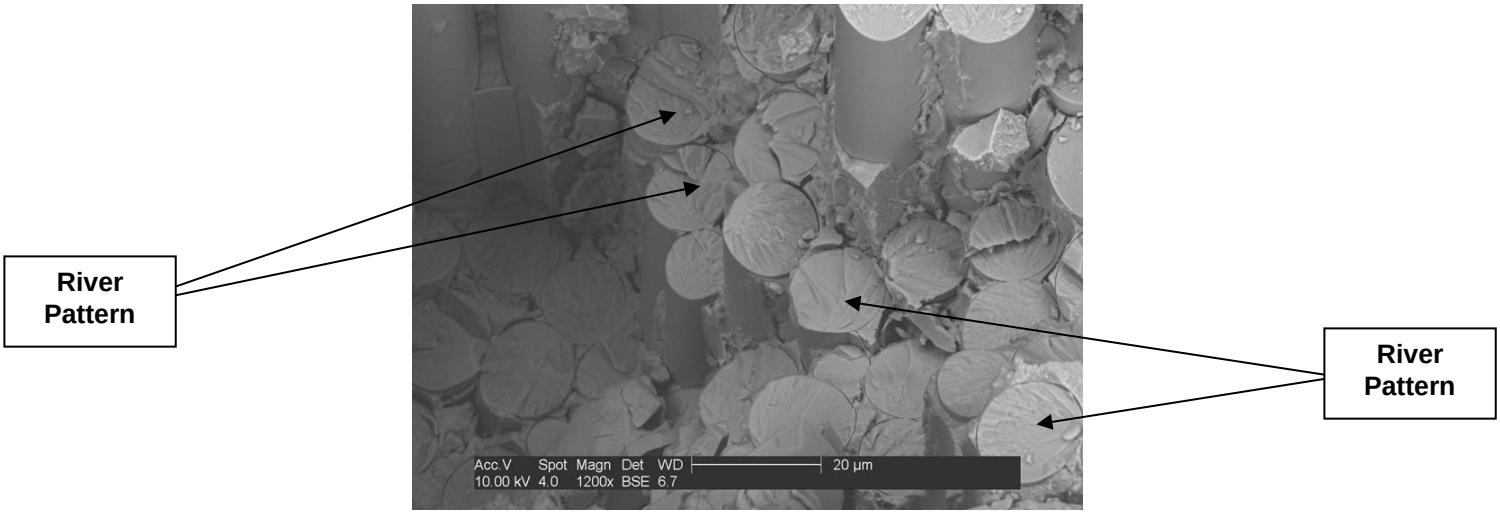


**Figure B-1.4.4: SEM Image of 3-D Starfire, 80 mil @ 1200x**. This image illustrates the "River Pattern" on the fractured surface indicative of surface bonding prior to tensile failure and the step function of the fractured surface exhibited by all 3-D material.

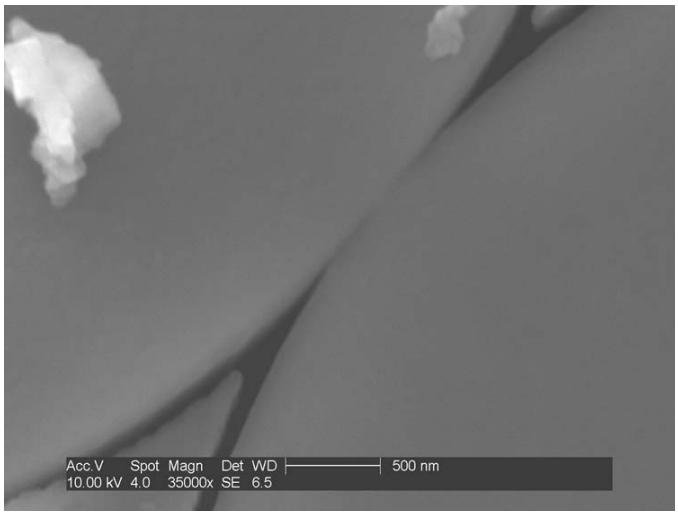


**Figure B-1.4.5: SEM Image of 3-D Starfire, 80 mil @ 35kx.** Surface bonded leading to low fiber strength.

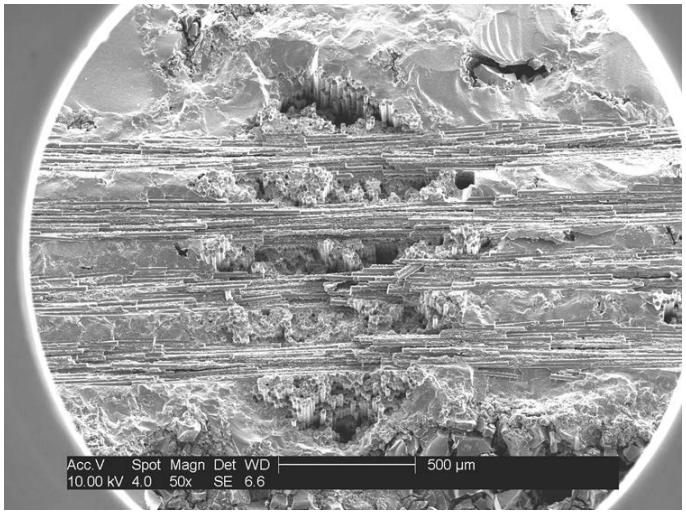


**Figure B-1.4.6: SEM Image of 3-D Starfire, 80 mil @ 50x**. Additional image of fractured surface.

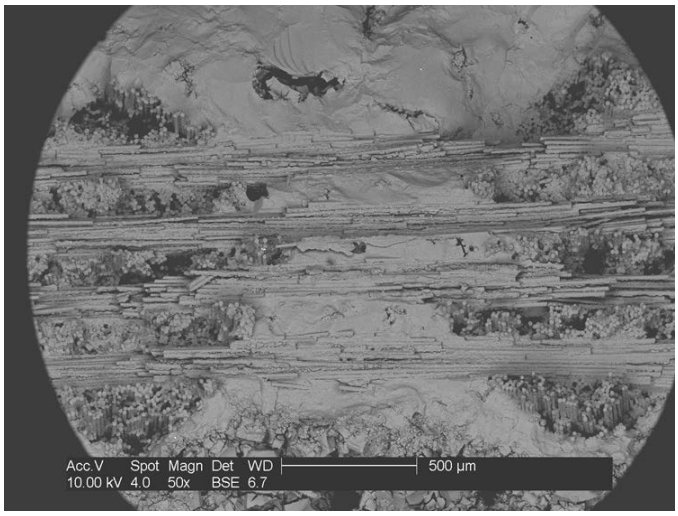


**Figure B-1.4.7: SEM Image of 3-D Starfire, 80 mil @ 50x**. Step function more pronounced in top and bottom plies of the fill fibers because the warp fibers squeeze these fibers into a wedge shape.

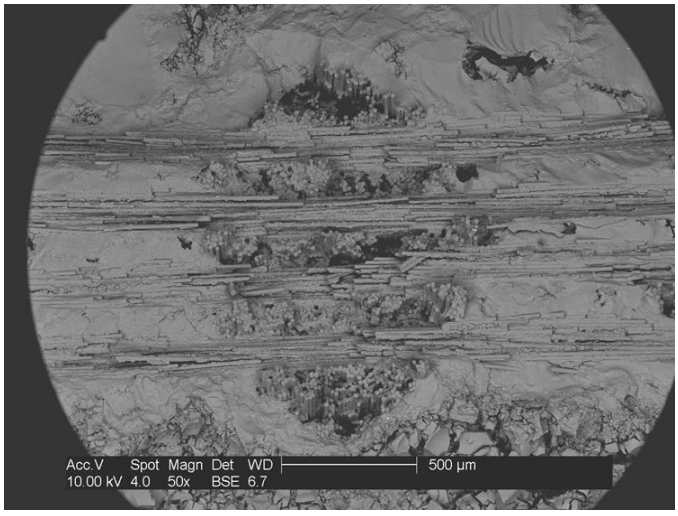


**Figure B-1.4.8: SEM Image of 3-D Starfire, 80 mil @ 50x**. Good image of fill fibers and some porosity in the matrix.

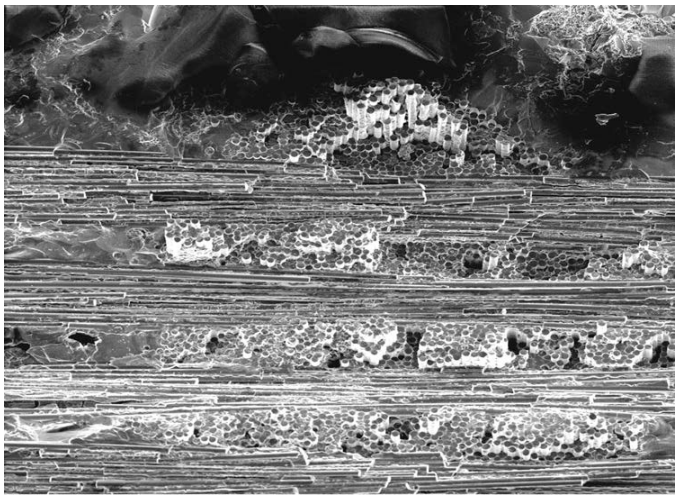

**Figure B-1.4.9: SEM Image of 3-D Starfire, 80 mil @ 100x**

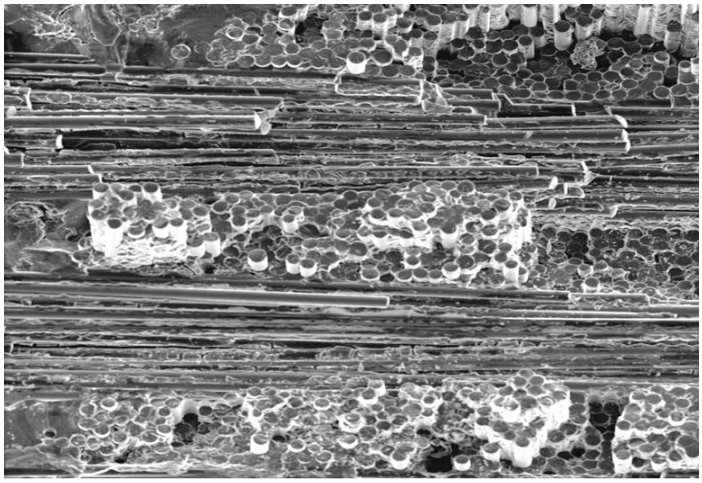

**Figure B-1.4.10: SEM Image of 3-D Starfire, 80 mil @ 200x**

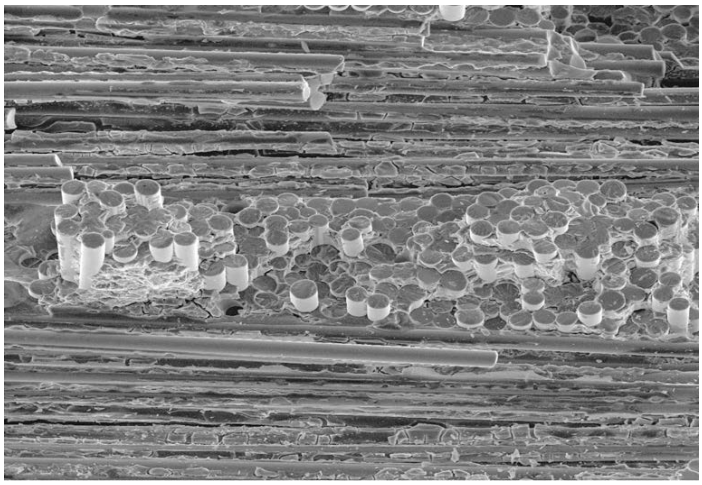

**Figure B-1.4.11: SEM Image of 3-D Starfire, 80 mil @ 300x**

## B-1.5 3-D STARFIRE, 145 MIL

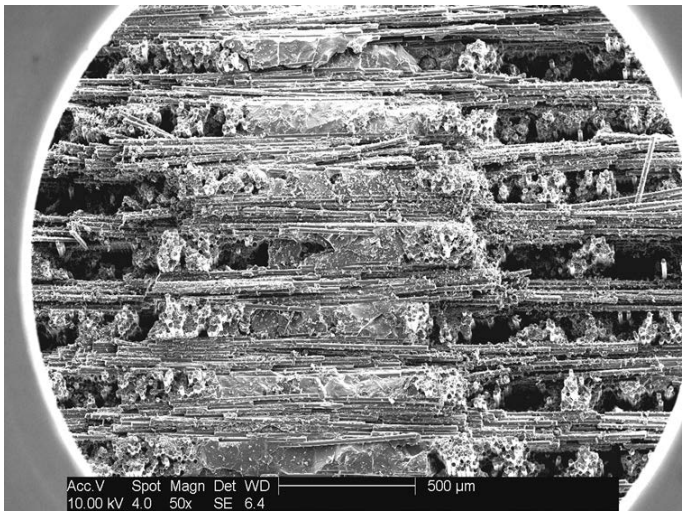


**Figure B-1.5.1: SEM Image of 3-D Starfire, 145 mil @ 50x**. Image of fill and tow fibers.

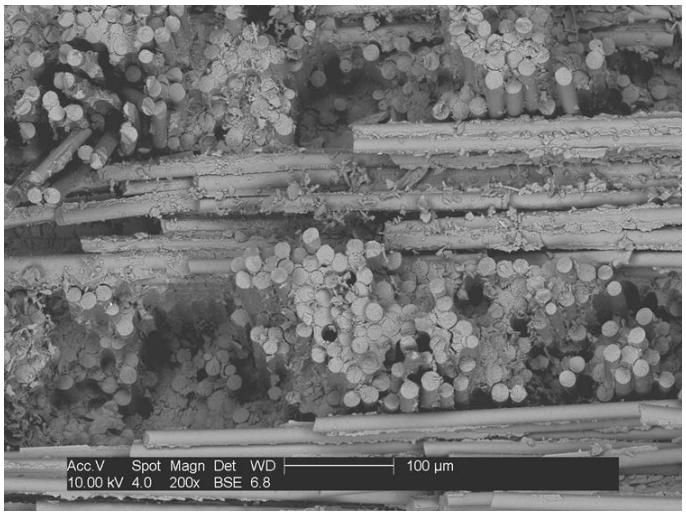


**Figure B-1.5.2: SEM Image of 3-D Starfire, 145 mil @ 200x.** Good illustration of the step function in the failed fibers and poor fiber poor fiber pull out.

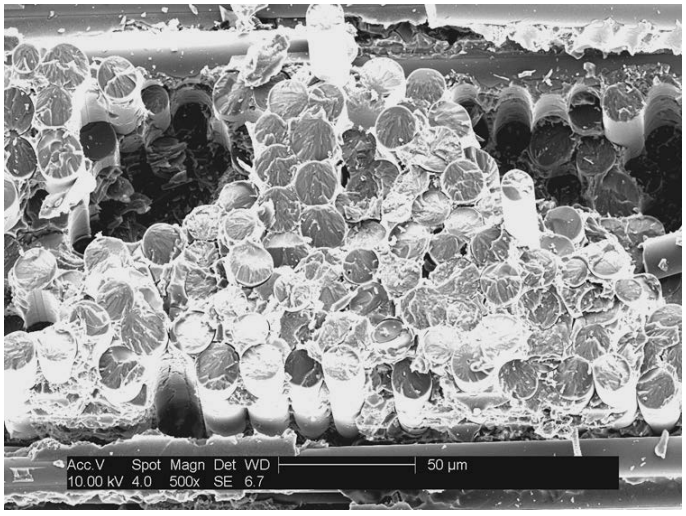


**Figure B-1.5.3: SEM Image of 3-D Starfire, 145 mil @ 500x**. This image illustrates the "River Pattern" that is indicative of surface bonding leading to low fiber strength and poor fiber pull out.

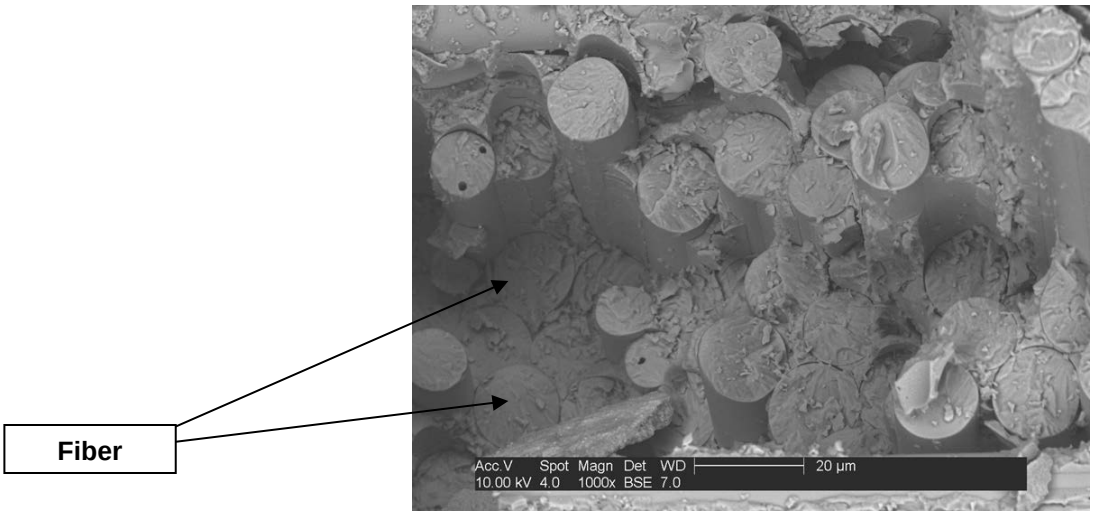


**Figure B-1.5.4: SEM Image of 3-D Starfire, 145 mil @ 1000x**. Good illustration of the step function.

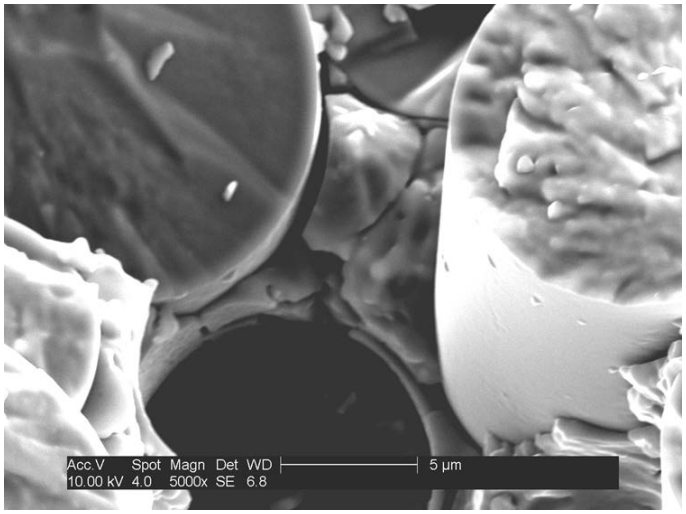


**Figure B-1.5.6: SEM Image of 3-D Starfire, 145 mil @ 5000x**

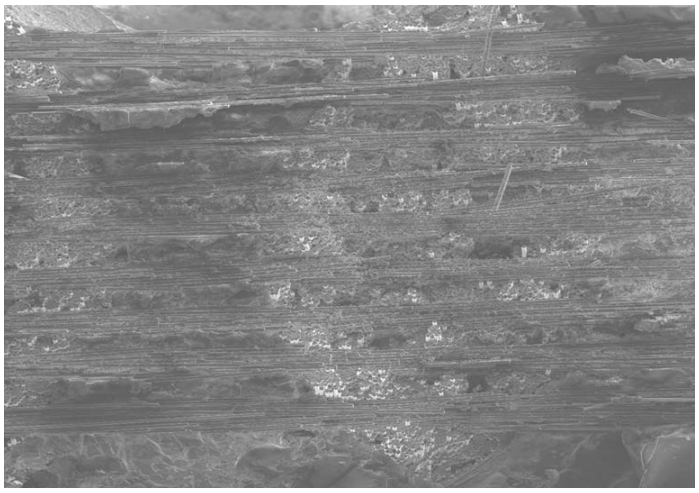

**Figure B-1.5.7: SEM Image of 3-D Starfire, 145 mil @ 25x**

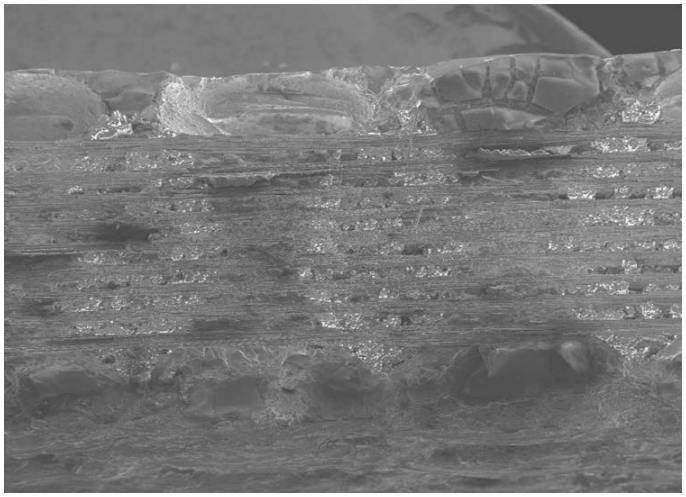

**Figure B-1.5.8: SEM Image of 3-D Starfire, 145 mil @ 26x**

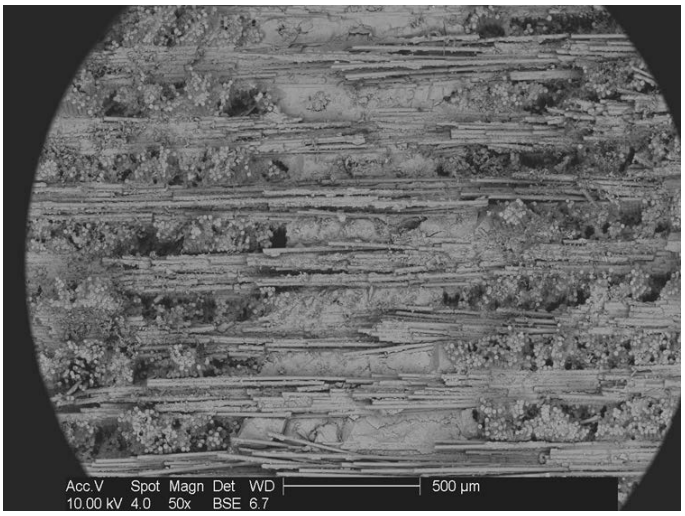


**Figure B-1.5.9: SEM Image of 3-D Starfire, 145 mil @ 50x**

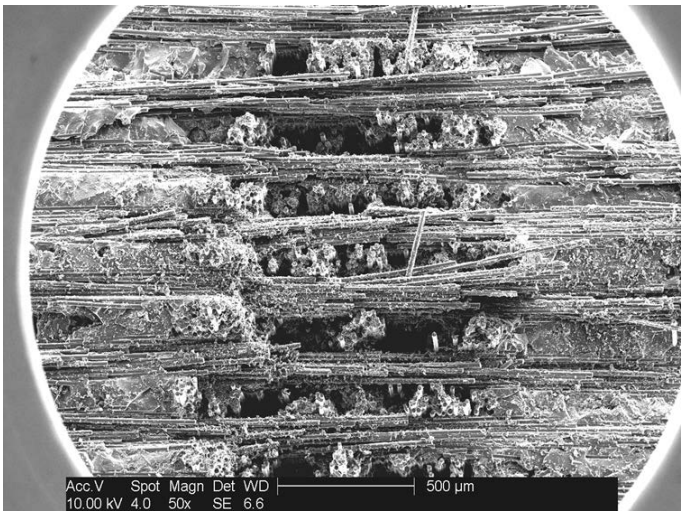


**Figure B-1.5.10: SEM Image of 3-D Starfire, 145 mil @ 50x**

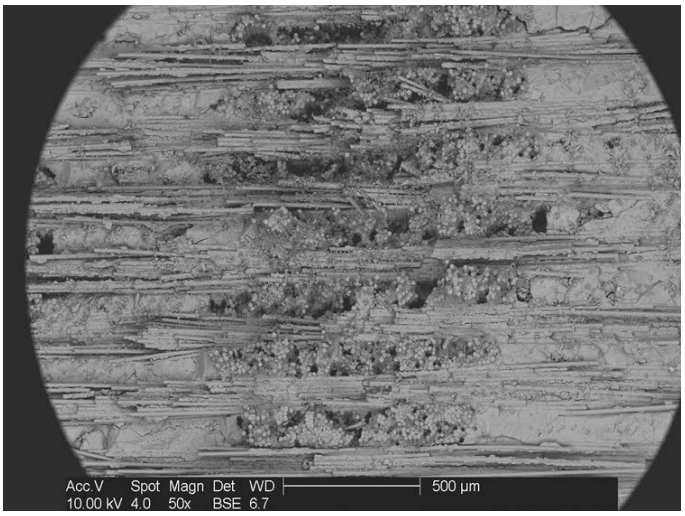


**Figure B-1.5.11: SEM Image of 3-D Starfire, 145 mil @ 50x**

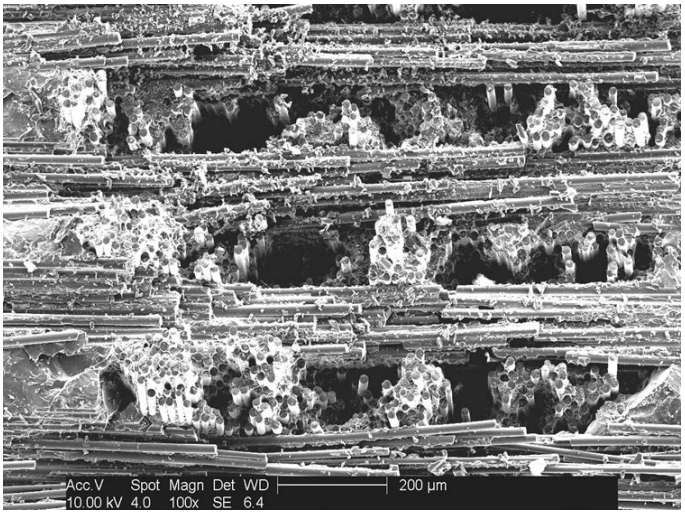


**Figure B-1.5.12: SEM Image of 3-D Starfire, 145 mil @ 100x**

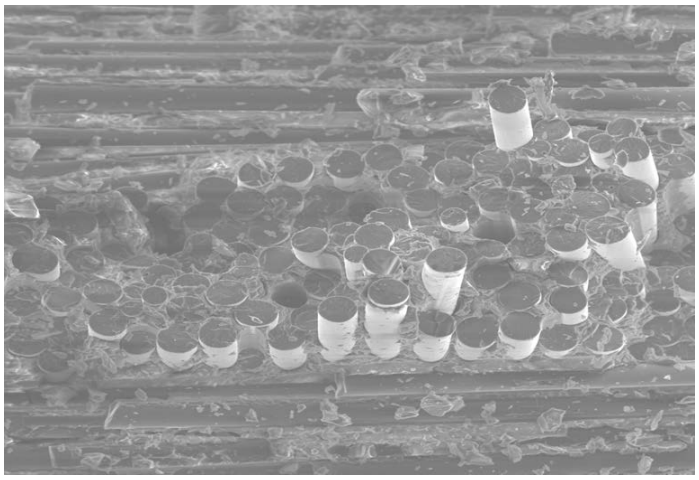

**Figure B-1.5.13: SEM Image of 3-D Starfire, 145 mil @ 150x**

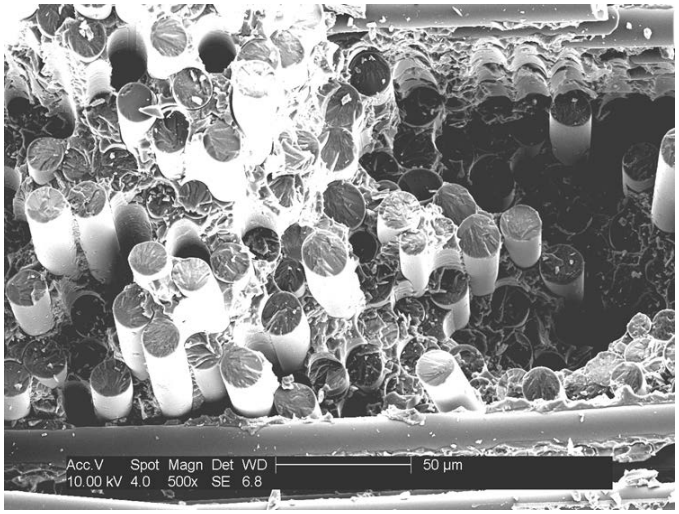


**Figure B-1.5.14: SEM Image of 3-D Starfire, 145 mil @ 500x**

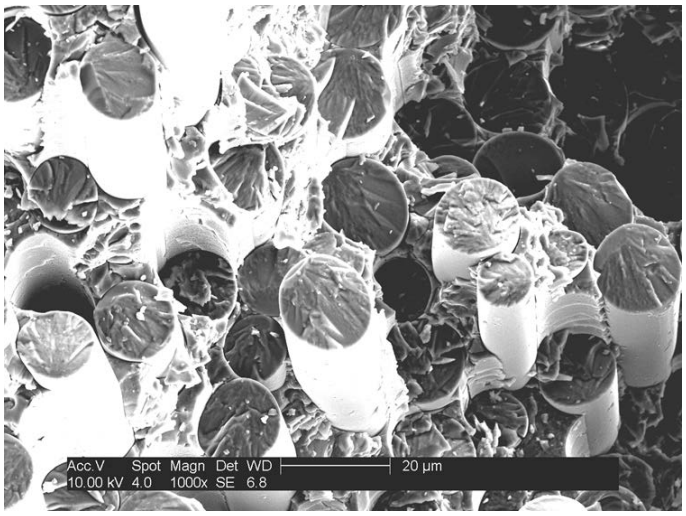


**Figure B-1.5.15: SEM Image of 3-D Starfire, 145 mil @ 1000x**

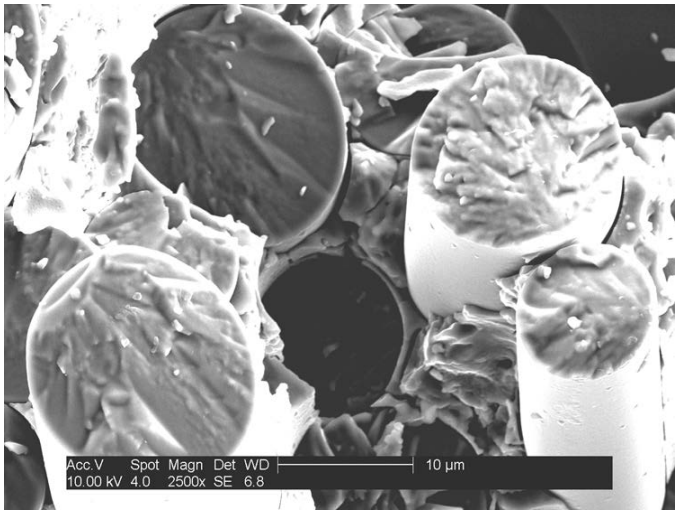


**Figure B-1.5.16: SEM Image of 3-D Starfire, 145 mil @ 2500x**

## B-2 POLISHED SURFACE

### B-2.1 2-D S200-1, 80 MIL

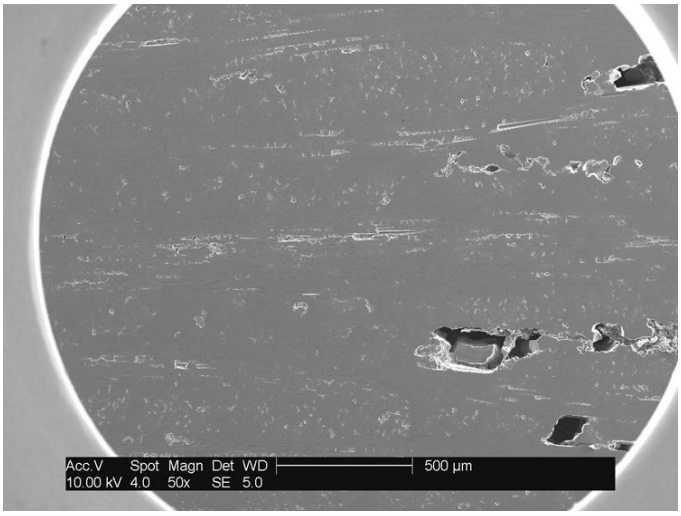


**Figure B-2.1.1: SEM Image of Polished 2-D S200-1, 80 mil @ 50x**.
Some porosity but not much compared to 3-D.

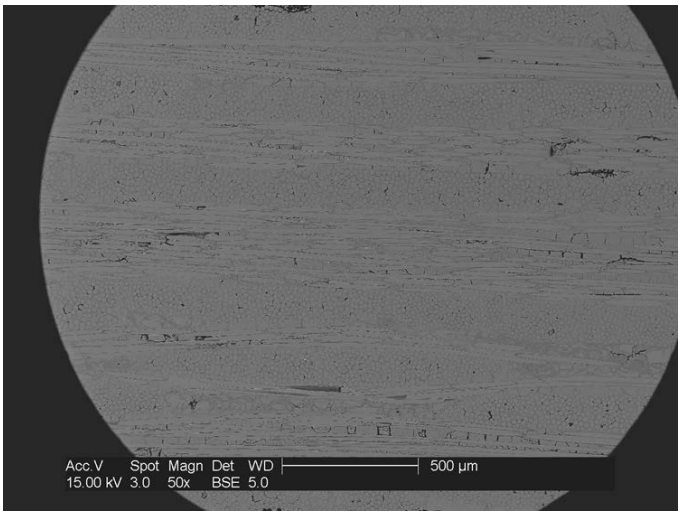


**Figure B-2.1.2: SEM Image of Polished 2-D S200-1, 80 mil @ 50x**.
Typical image of 2-D material.

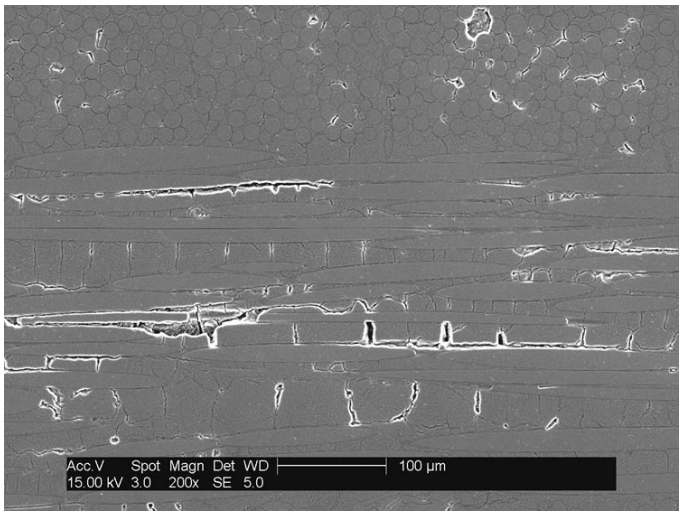


**Figure B-2.1.3: SEM Image of Polished 2-D S200-1, 80 mil @ 200x**.
Image of the fill and tow fibers…very little porosity.

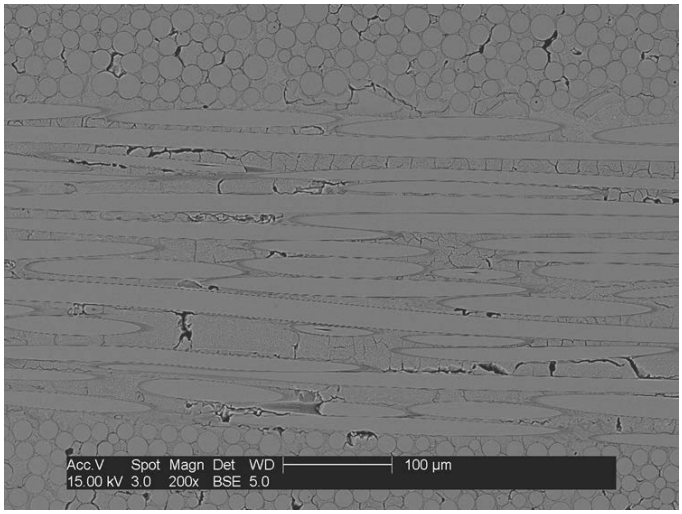


**Figure B-2.1.4: SEM Image of Polished 2-D S200-1, 80 mil @ 200x**.
Additional image of the fill and tow fibers.

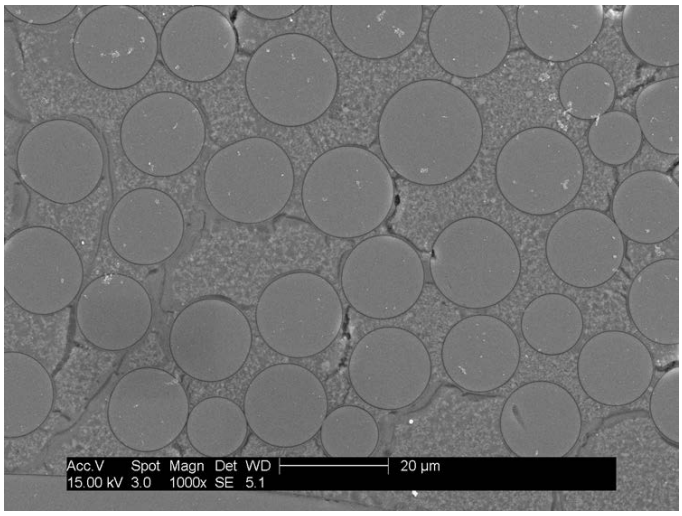


**Figure B-2.1.5: SEM Image of Polished 2-D S200-1, 80 mil @ 1000x**.
Very little to no surface bonding in the 2-D material.

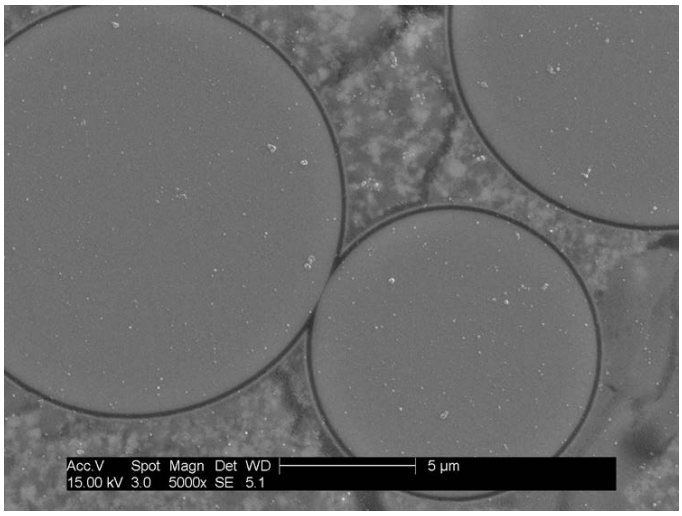


**Figure B-2.1.6: SEM Image of Polished 2-D S200-1, 80 mil @ 5000x**.
Very little surface bonding.

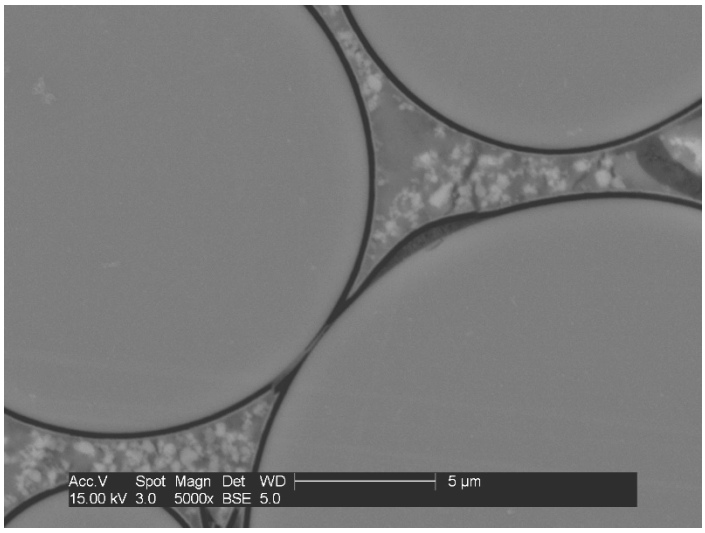


**Figure B-2.1.7: SEM Image of Polished 2-D S200-1, 80 mil @ 5000x.**
Most of what appeared to be surface bonding in 2-D material was not.

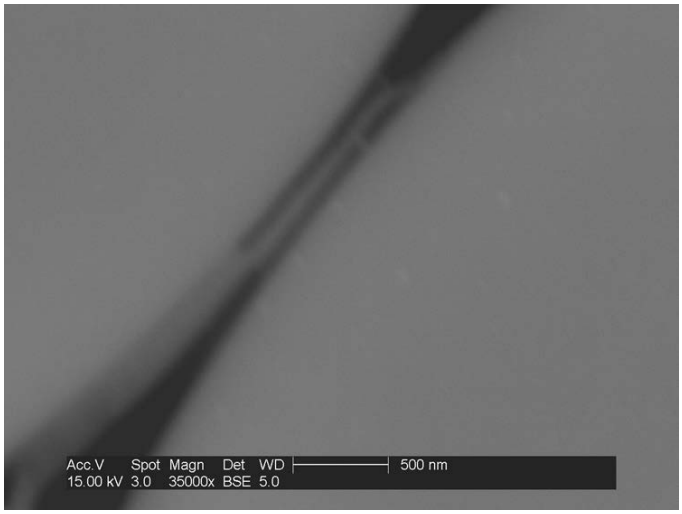


**Figure B-2.1.8: SEM Image of Polished 2-D S200-1, 80 mil @ 35kx**.
Most of what appeared to be surface bonding in 2-D material was not.

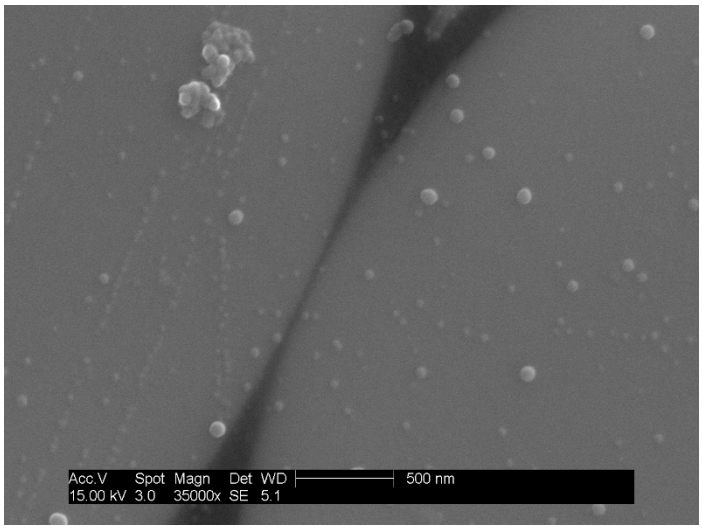


**Figure B-2.1.9: SEM Image of Polished 2-D S200-1, 80 mil @ 35kx.**
Additional image faux surface bonding in 2-D material was not.

## B-2.2 3-D S200-1, 80 MIL

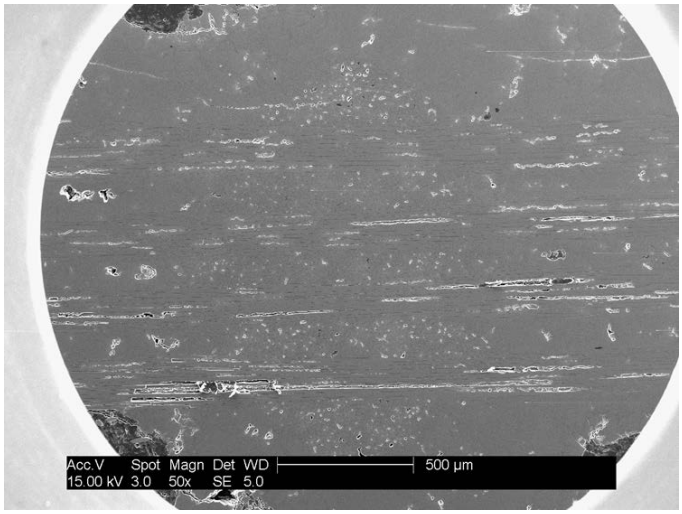


**Figure B-2.2.1: SEM Image of Polished 3-D S200-1, 80 mil @ 50x**

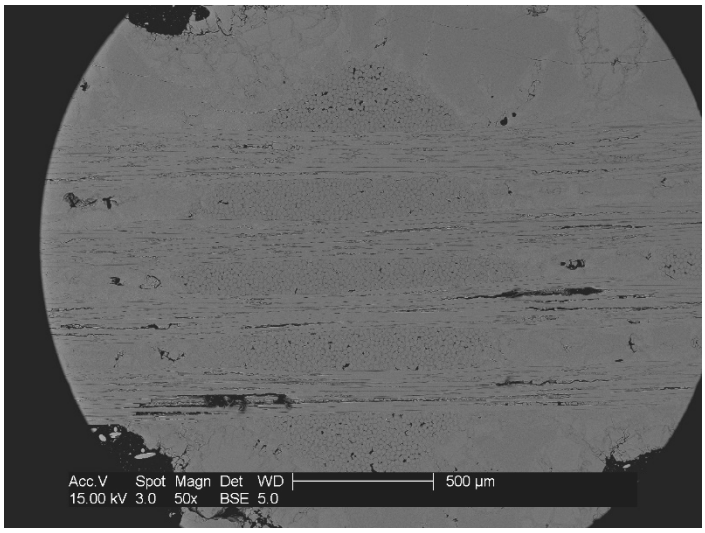


**Figure B-2.2.2: SEM Image of Polished 3-D S200-1, 80 mil @ 50x**.
Some porosity...more than 2-D material.

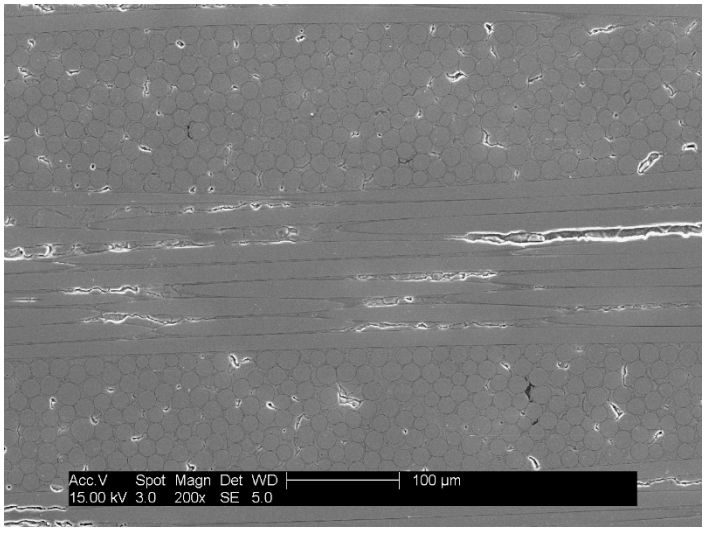


**Figure B-2.2.3: SEM Image of Polished 3-D S200-1, 80 mil @ 200x**.
Image of the fill and tow fibers.

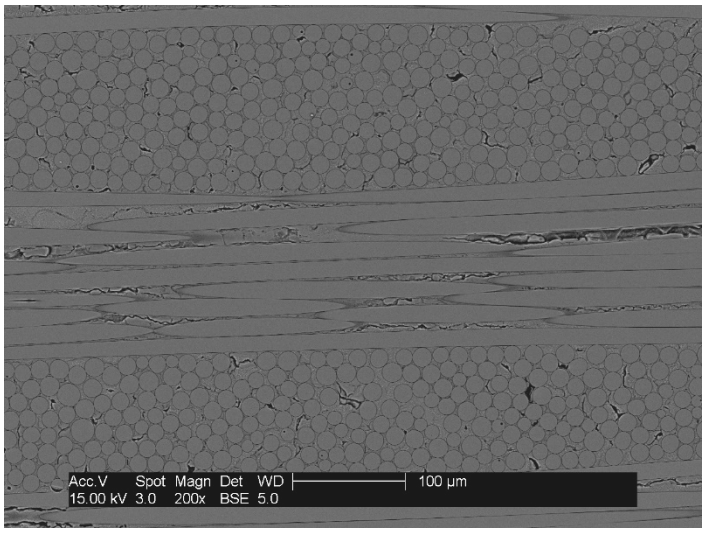


**Figure B-2.2.4: SEM Image of Polished 3-D S200-1, 80 mil @ 200x**

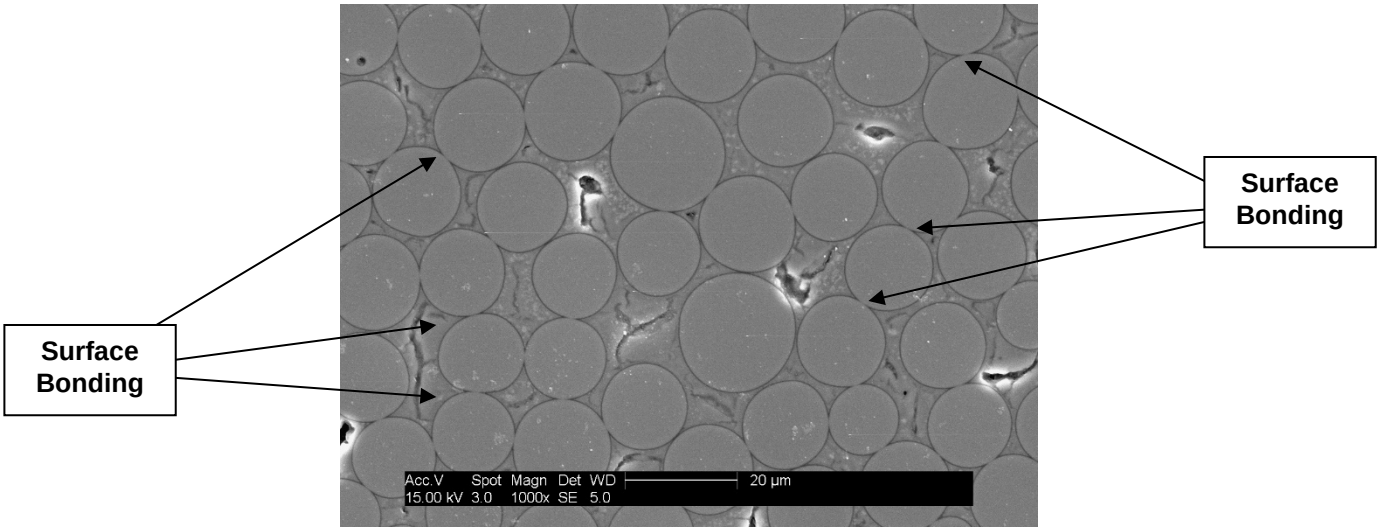


**Figure B-2.2.5: SEM Image of Polished 3-D S200-1, 80 mil @ 1000x**.
Excellent illustration of surface bonding.

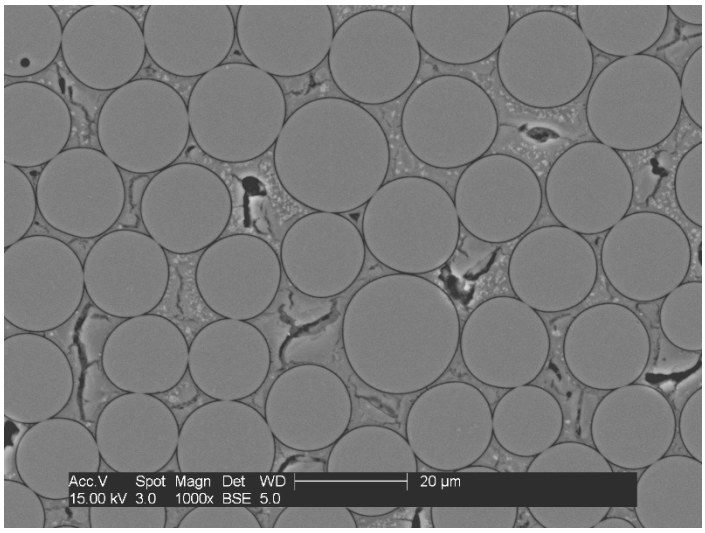


**Figure B-2.2.6: SEM Image of Polished 3-D S200-1, 80 mil @ 1000x.**
Excellent illustration of surface bonding.

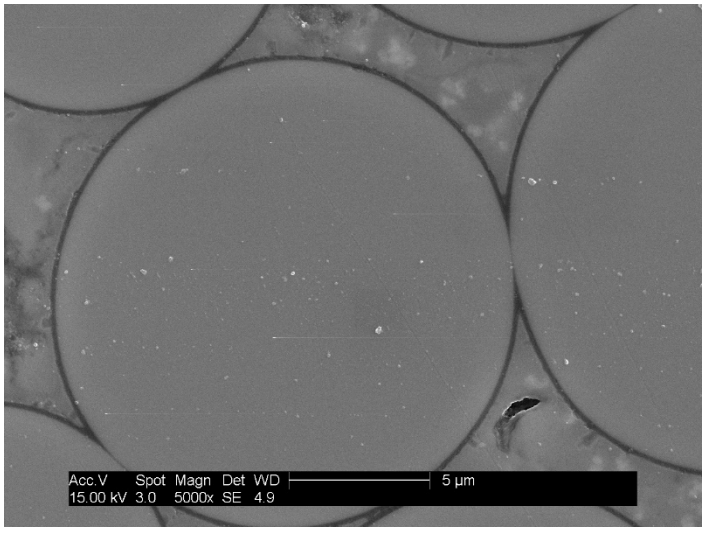


**Figure B-2.2.7: SEM Image of Polished 3-D S200-1, 80 mil @ 5000x**

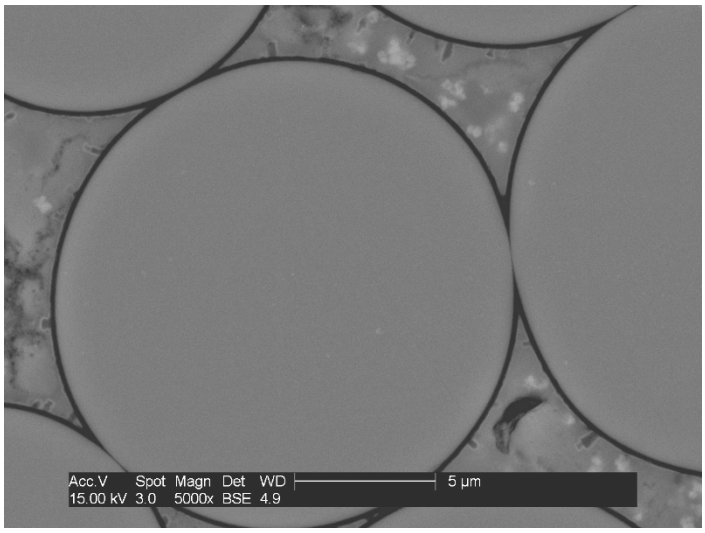


**Figure B-2.2.8: SEM Image of Polished 3-D S200-1, 80 mil @ 5000x.**
At the same magnification as 2-D, more fibers are captured showing surface bonding.

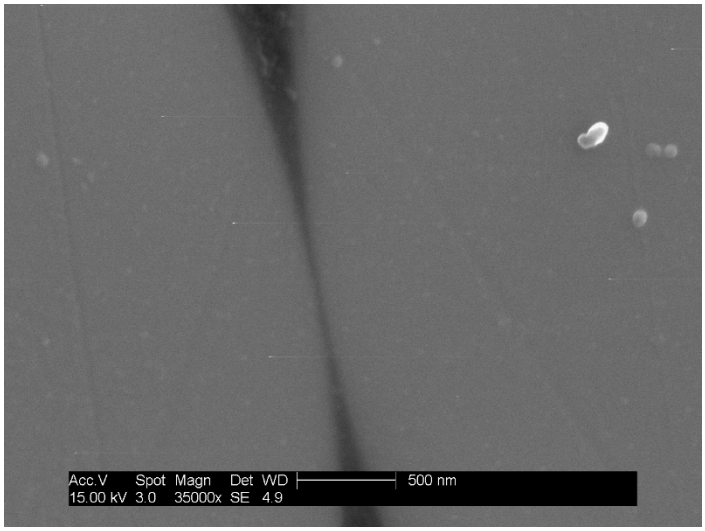


**Figure B-2.2.9: SEM Image of Polished 3-D S200-1, 80 mil @ 35kx**.
Illustration of surface bonding.

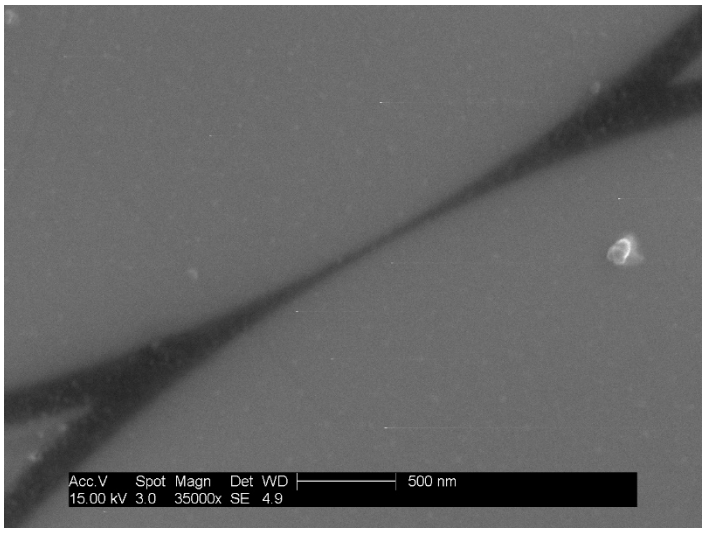


**Figure B-2.2.10: SEM Image of Polished 3-D S200-1, 80 mil @ 35kx**.
Surface bonding.

## B-2.3 3-D S200-1, 145 MIL

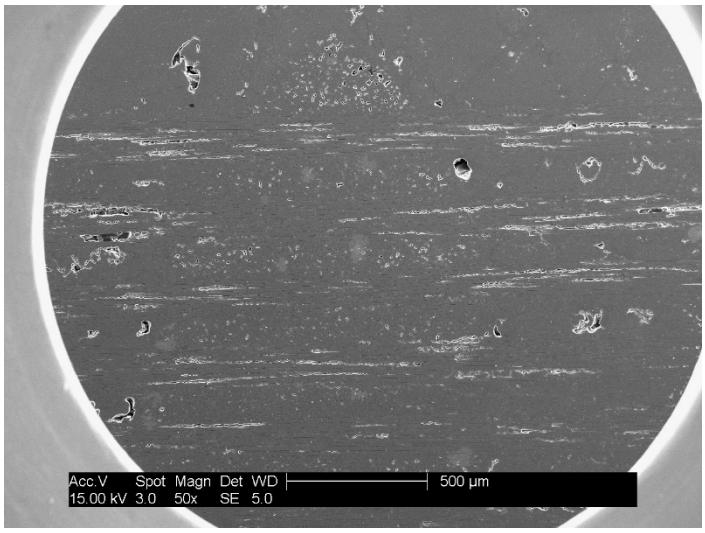


**Figure B-2.3.1: SEM Image of Polished 3-D S200-1, 145 mil @ 50x**

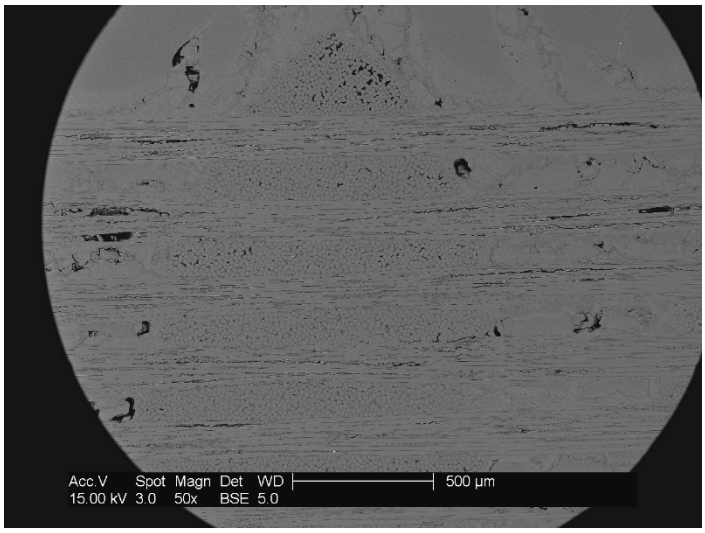


**Figure B-2.3.2: SEM Image of Polished 3-D S200-1, 145 mil @ 50x**.
Image shows porosity in this material.

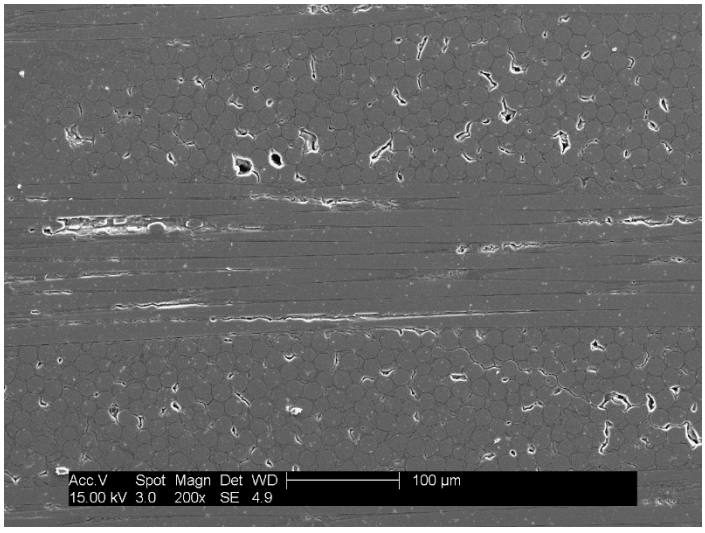


**Figure B-2.3.3: SEM Image of Polished 3-D S200-1, 145 mil @ 200x**.
Porosity throughout this material.

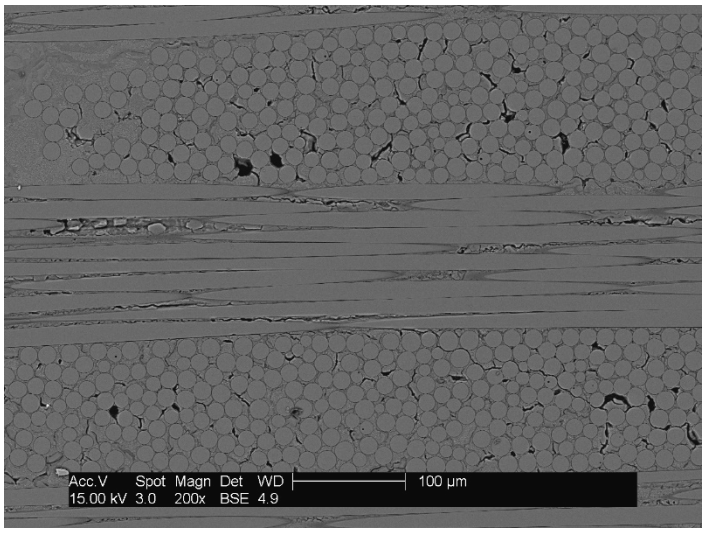


**Figure B-2.3.4: SEM Image of Polished 3-D S200-1, 145 mil @ 200x**

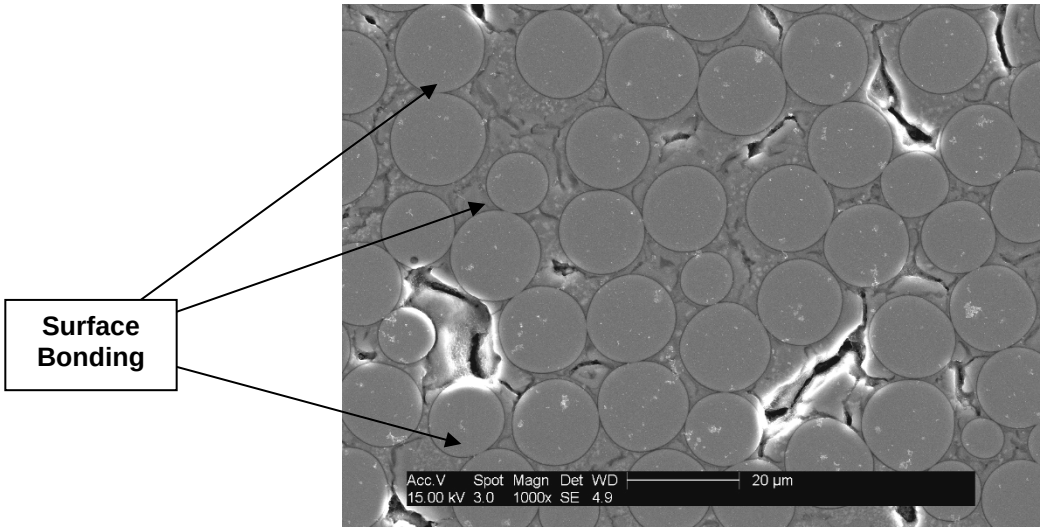


**Figure B-2.3.5: SEM Image of Polished 3-D S200-1, 145 mil @ 1000x**.
More surface bonding and porosity exhibited in this material.

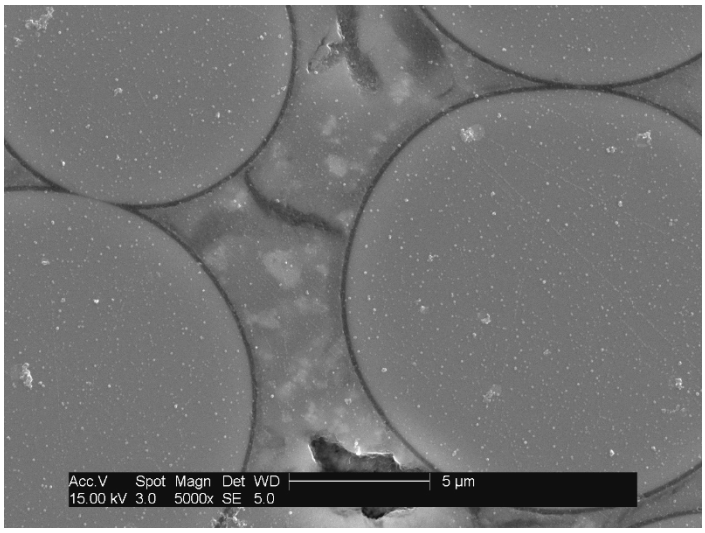


**Figure B-2.3.7: SEM Image of Polished 3-D S200-1, 145 mil @ 5000x**.
Good image of surface bonding.

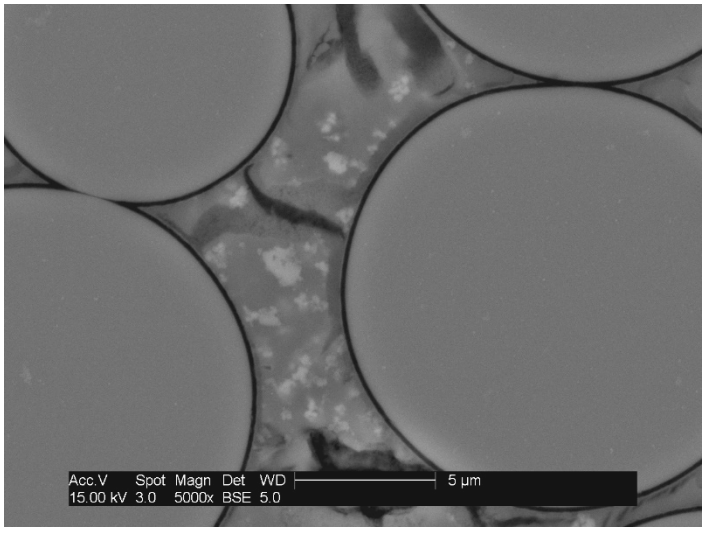


**Figure B-2.3.8: SEM Image of Polished 3-D S200-1, 145 mil @ 5000x**.
Same image with back scatter on.

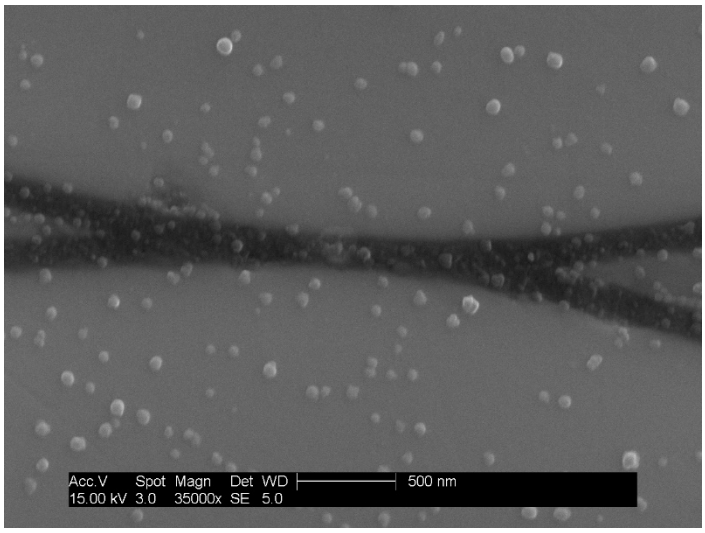


**Figure B-2.3.9: SEM Image of Polished 3-D S200-1, 145 mil @ 35kx.**
Image showing that some fibers that appear to be touching was not; however this is the case 10% of time.

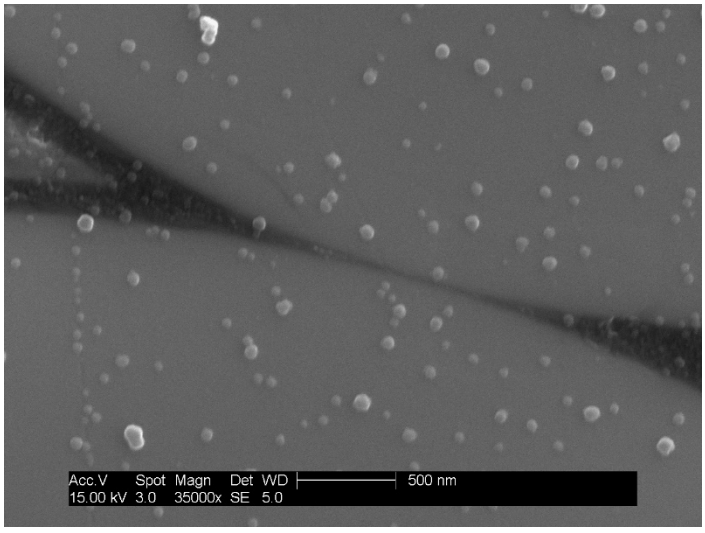


**Figure B-2.3.10: SEM Image of Polished 3-D S200-1, 145 mil @ 35kx**.
Image showing that some fibers that appear to be touching was touching which is the case 90% of time.

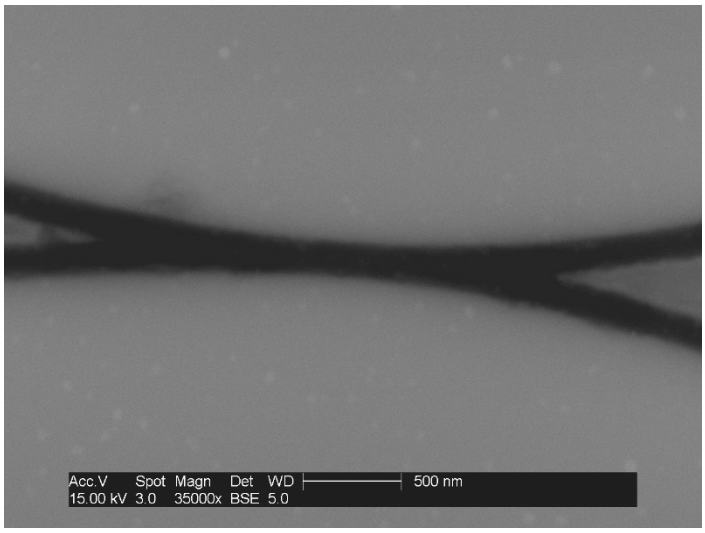


**Figure B-2.3.11: SEM Image of Polished 3-D S200-1, 145 mil @ 35kx**

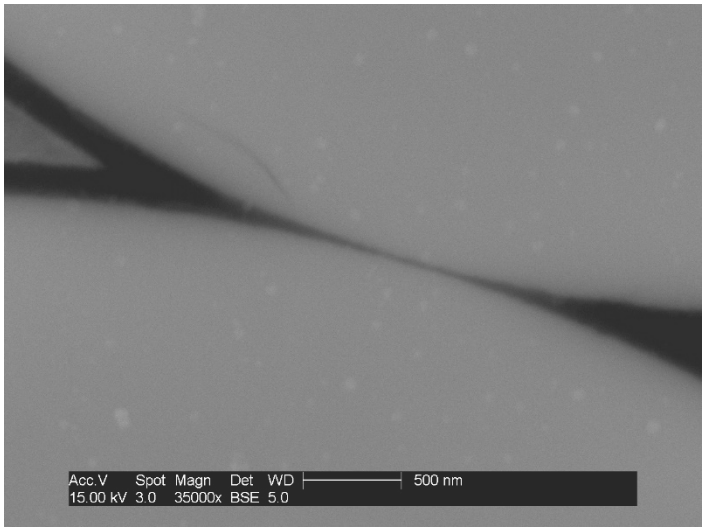


**Figure B-2.3.12: SEM Image of Polished 3-D S200-1, 145 mil @ 35kx**

## B-2.4 3-D STARFIRE, 80 MIL

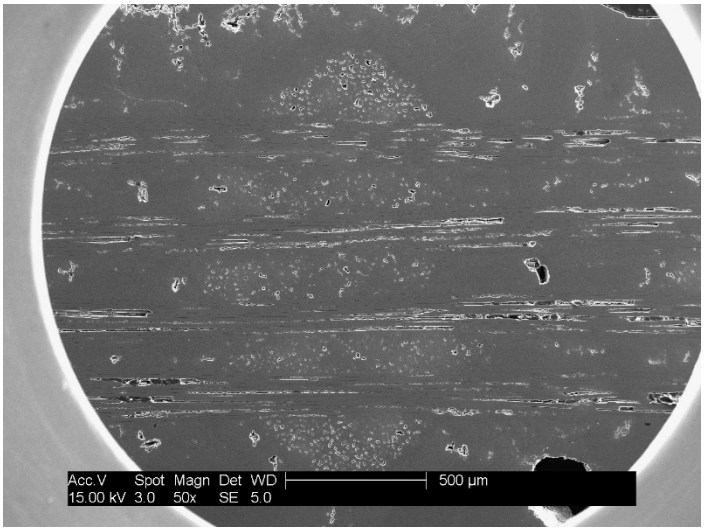


**Figure B-2.4.1: SEM Image of Polished 3-D Starfire, 80 mil @ 50x**

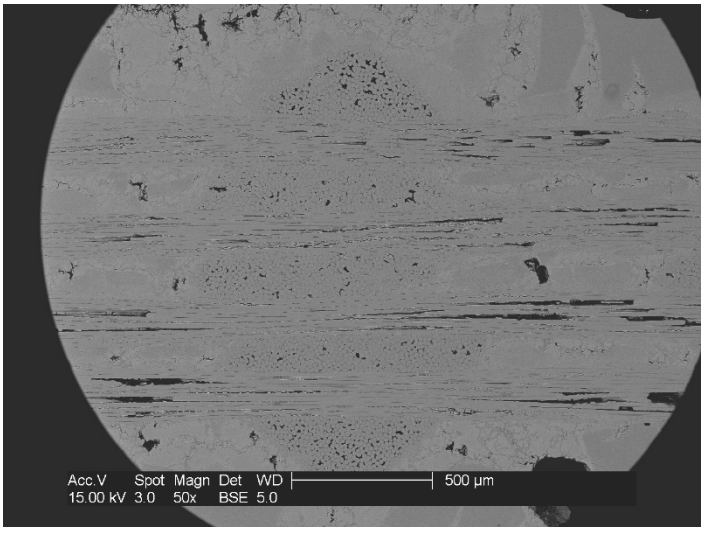


**Figure B-2.4.2: SEM Image of Polished 3-D Starfire, 80 mil @ 50x**

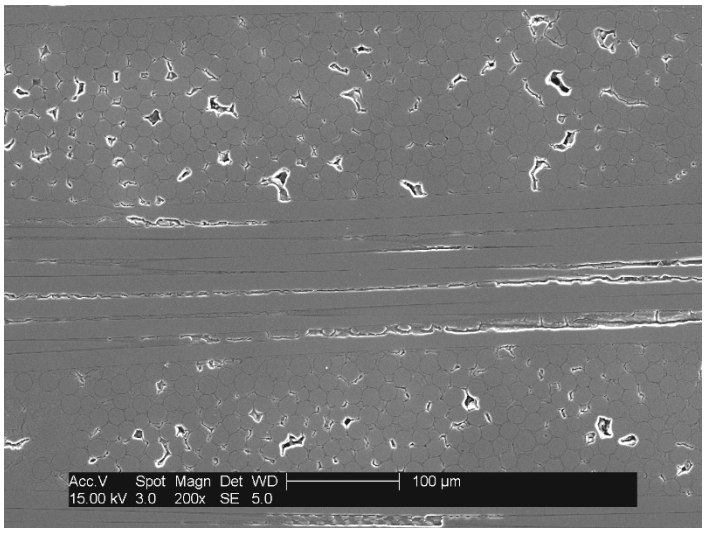


**Figure B-2.4.3: SEM Image of Polished 3-D Starfire, 80 mil @ 200x**

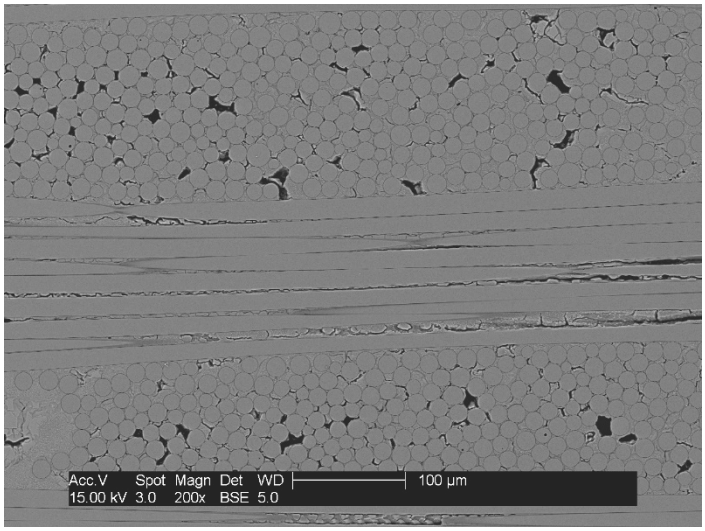


**Figure B-2.4.4: SEM Image of Polished 3-D Starfire, 80 mil @ 200x**

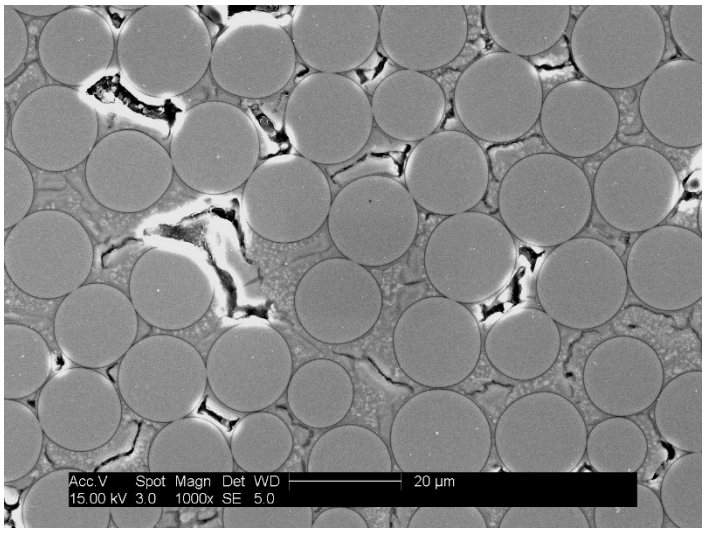


**Figure B-2.4.5: SEM Image of Polished 3-D Starfire, 80 mil @ 1000x**

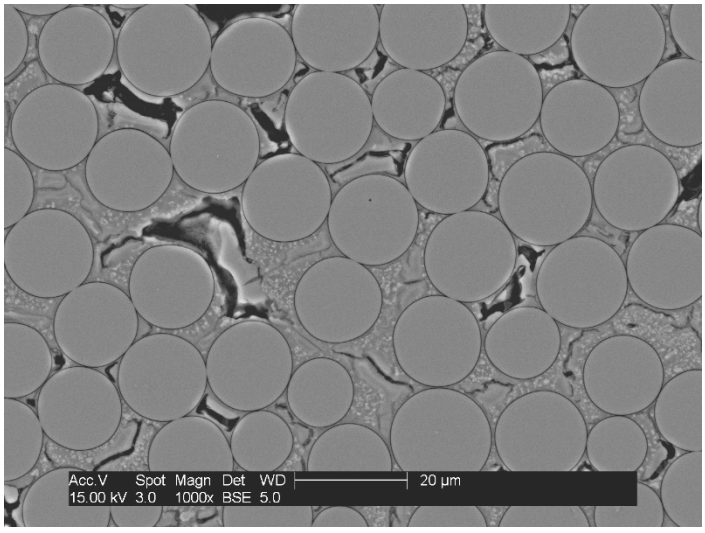


**Figure B-2.4.6: SEM Image of Polished 3-D Starfire, 80 mil @ 1000x**

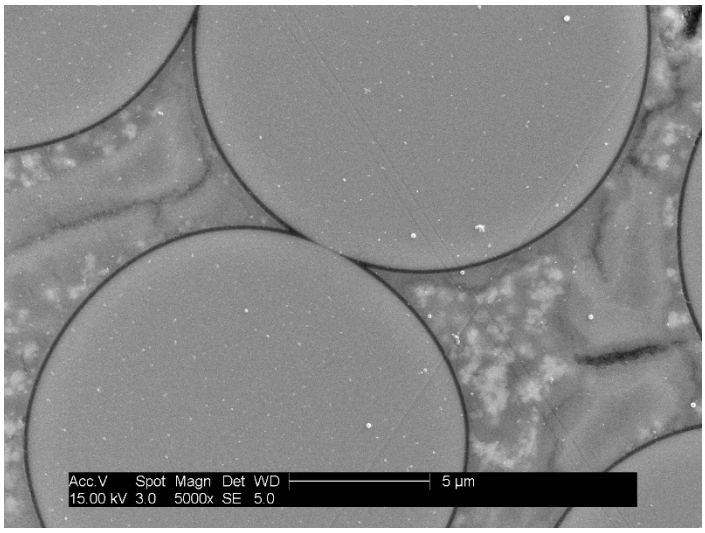


**Figure B-2.4.7: SEM Image of Polished 3-D Starfire, 80 mil @ 5000x**

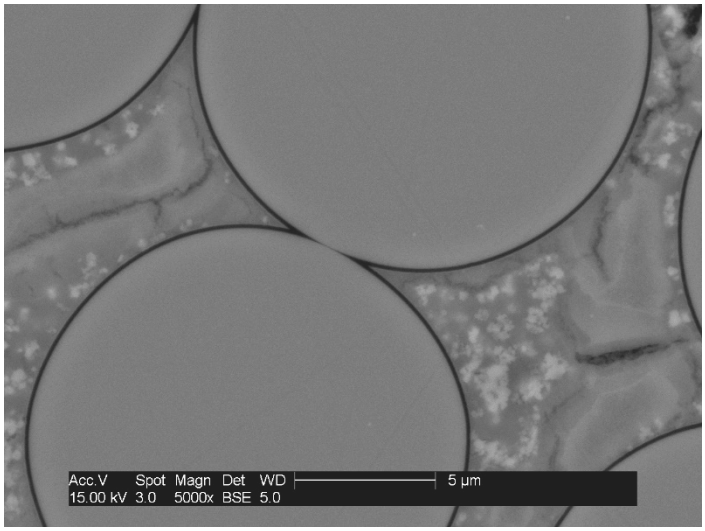


**Figure B-2.4.8: SEM Image of Polished 3-D Starfire, 80 mil @ 5000x**

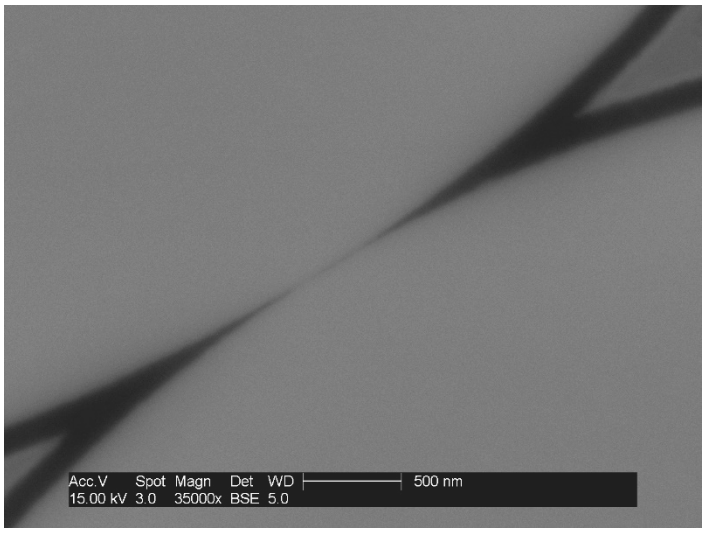


**Figure B-2.4.9: SEM Image of Polished 3-D Starfire, 80 mil @ 35kx**

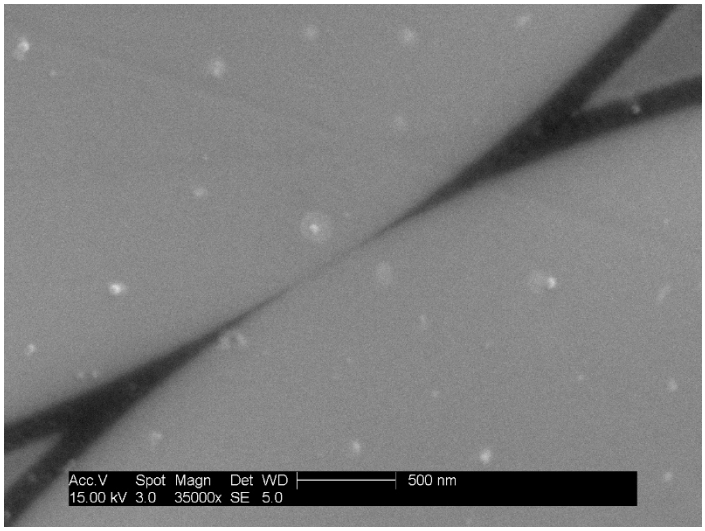


**Figure B-2.4.10: SEM Image of Polished 3-D Starfire, 80 mil @ 35kx**

## B-2.5 3-D STARFIRE, 145 MIL

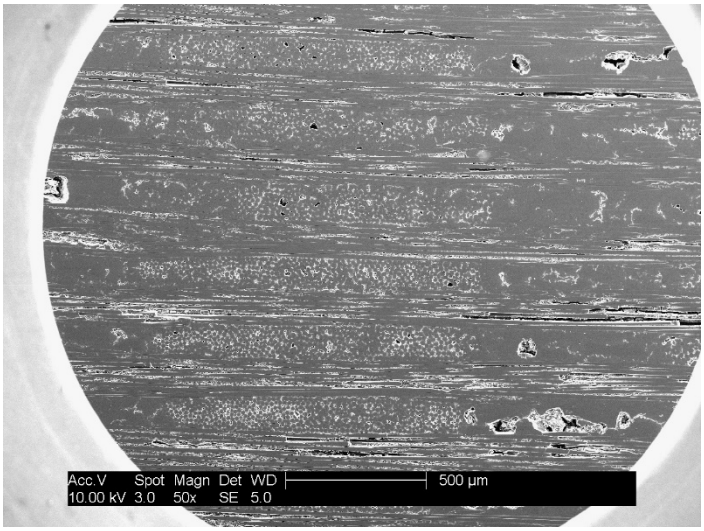


**Figure B-2.5.1: SEM Image of Polished 3-D Starfire, 145 mil @ 50x**

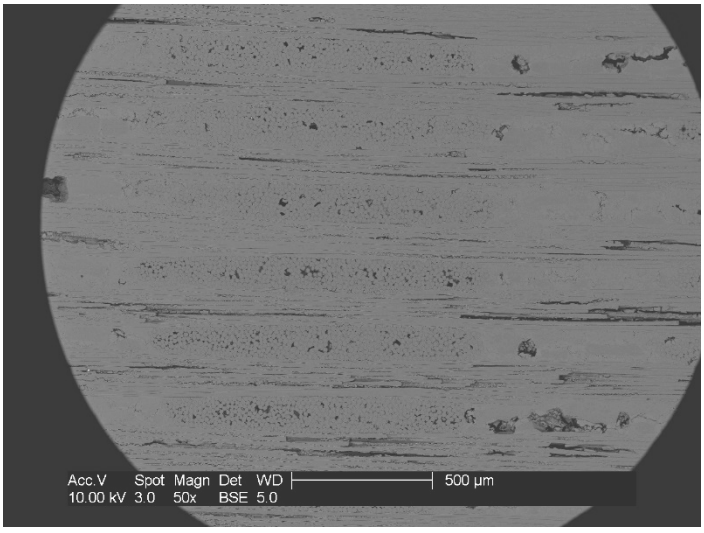


**Figure B-2.5.2: SEM Image of Polished 3-D Starfire, 145 mil @ 50x**

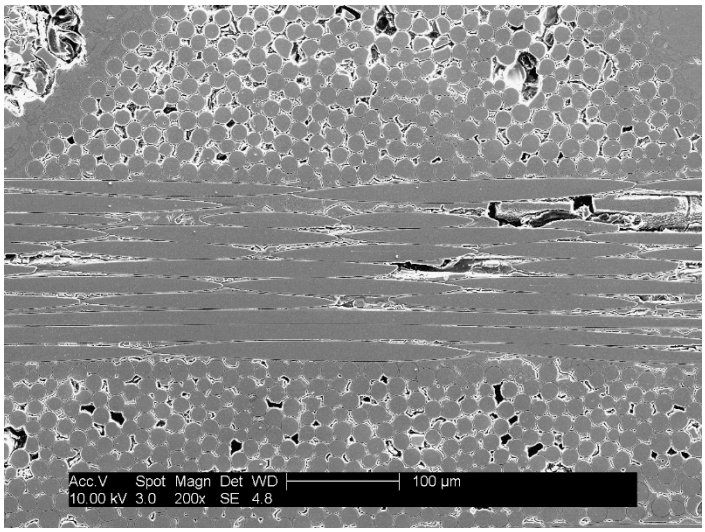


**Figure B-2.5.3: SEM Image of Polished 3-D Starfire, 145 mil @ 200x**

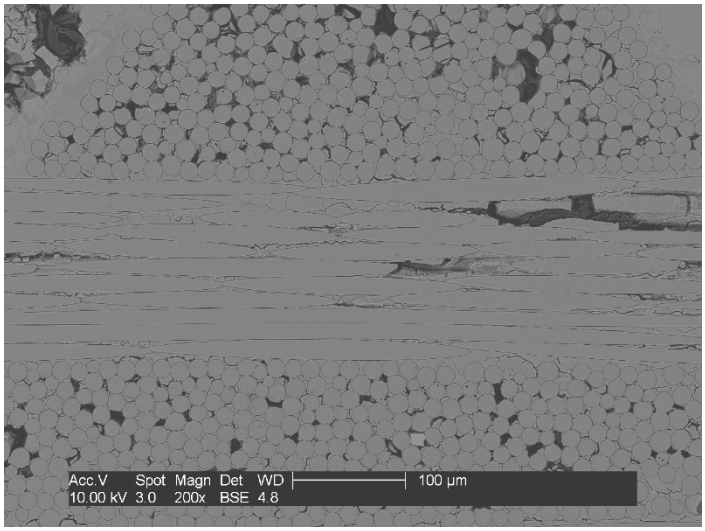


**Figure B-2.5.4: SEM Image of Polished 3-D Starfire, 145 mil @ 200x**

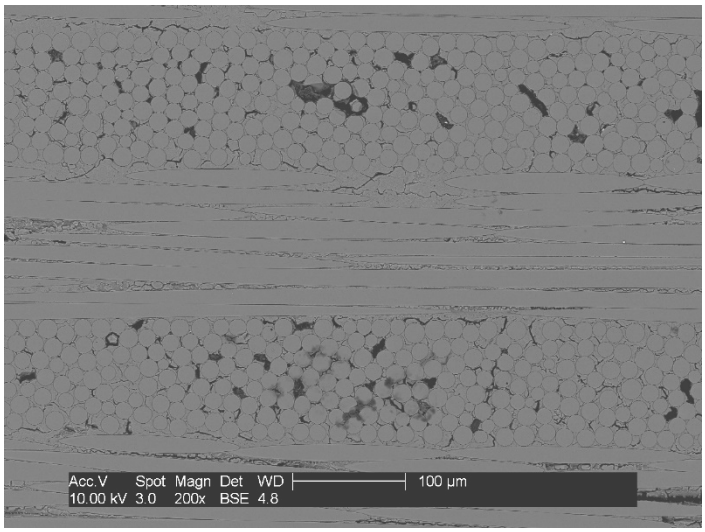


**Figure B-2.5.5: SEM Image of Polished 3-D Starfire, 145 mil @ 200x**

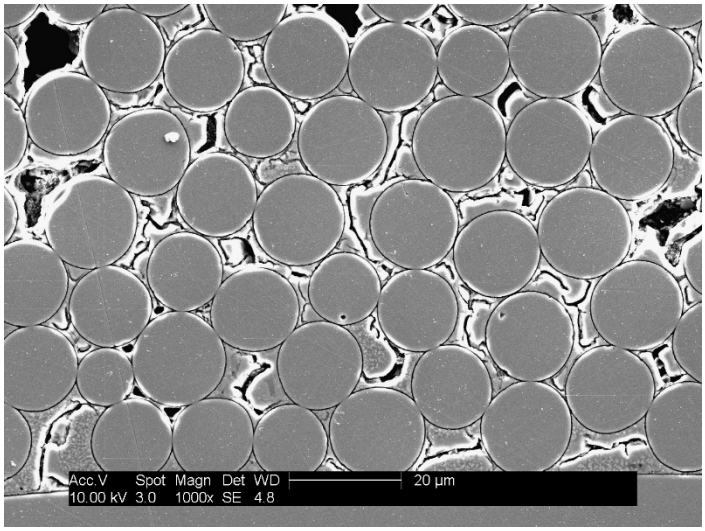


**Figure B-2.5.6: SEM Image of Polished 3-D Starfire, 145 mil @ 1000x**

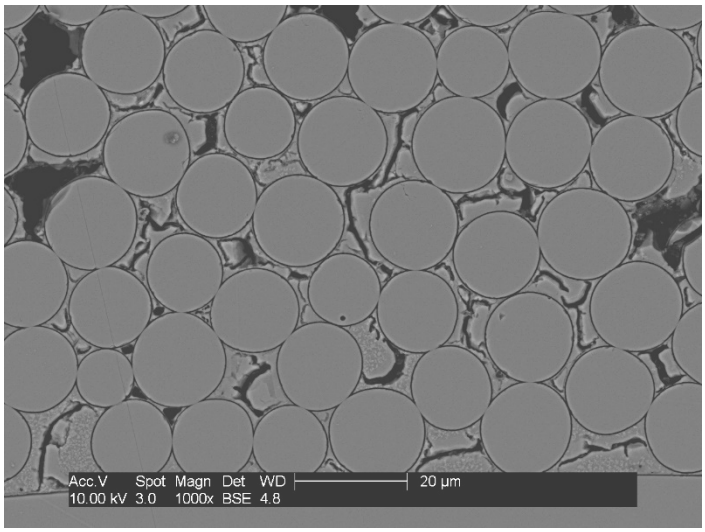


**Figure B-2.5.7: SEM Image of Polished 3-D Starfire, 145 mil @ 1000x**

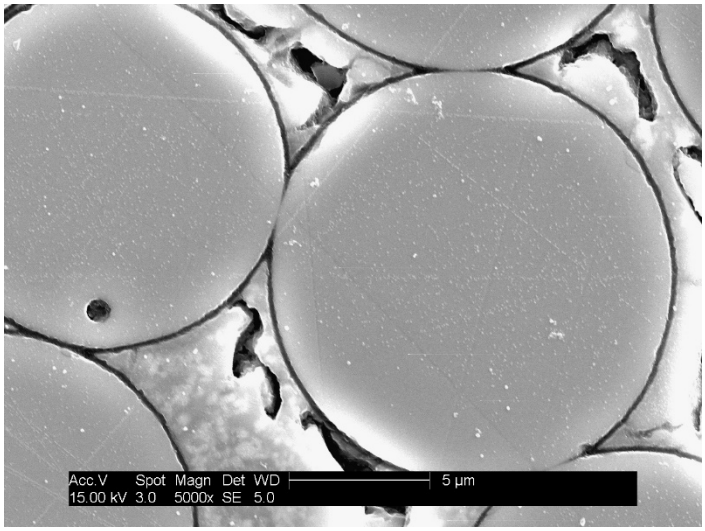


**Figure B-2.5.8: SEM Image of Polished 3-D Starfire, 145 mil @ 5000x**

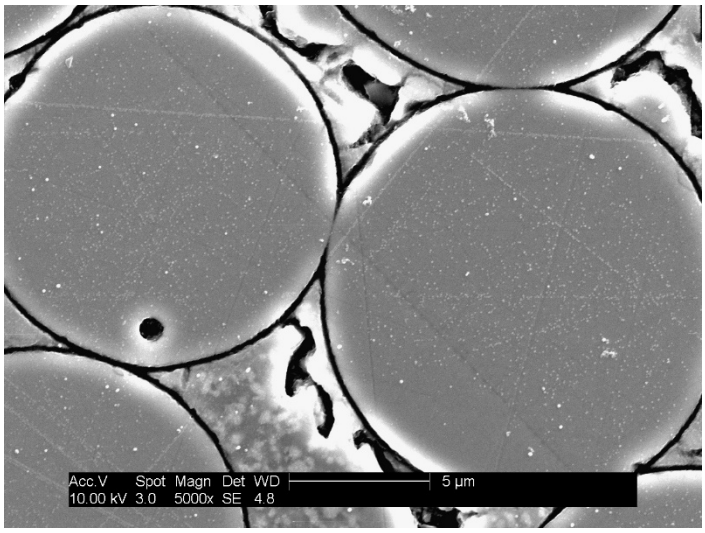


**Figure B-2.5.9: SEM Image of Polished 3-D Starfire, 145 mil @ 5000x**

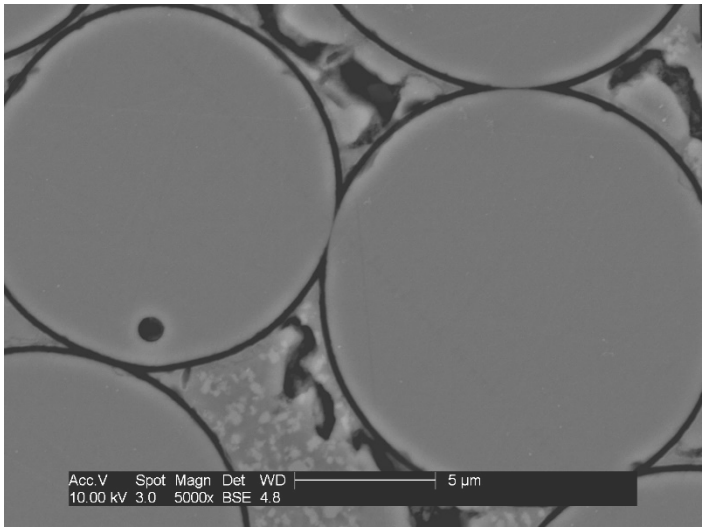


**Figure B-2.5.10: SEM Image of Polished 3-D Starfire, 145 mil @ 5000x**

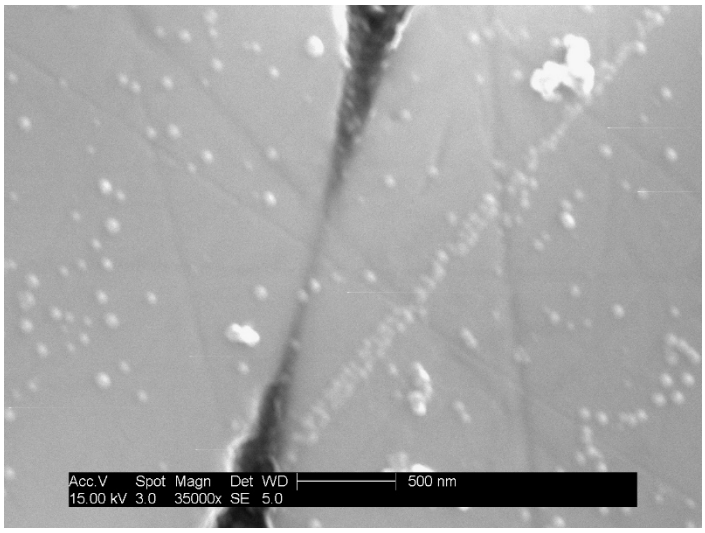


**Figure B-2.5.11: SEM Image of Polished 3-D Starfire, 145 mil @ 35kx**

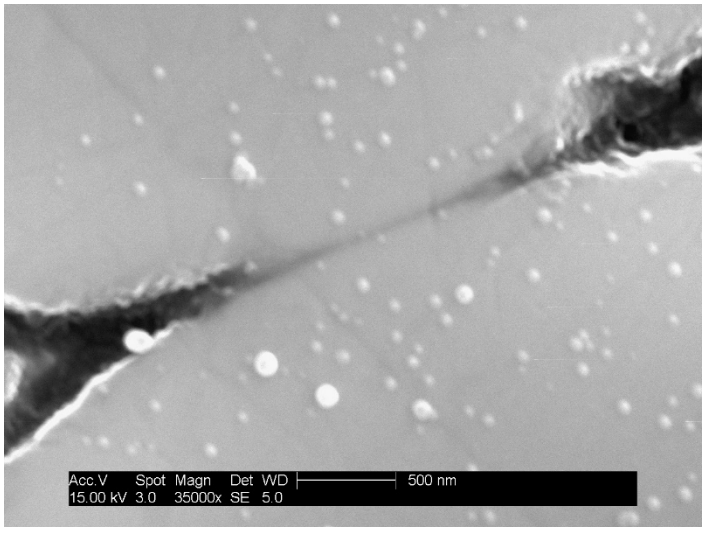


**Figure B-2.5.12: SEM Image of Polished 3-D Starfire, 145 mil @ 35kx**

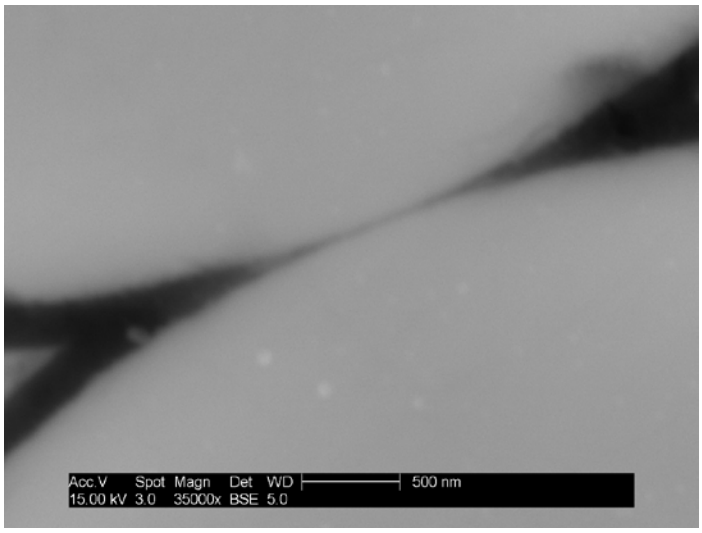


**Figure B-2.5.13: SEM Image of Polished 3-D Starfire, 145 mil @ 50x**

## APPENDIX C: STRESS VS. STRAIN PLOTS

### C-1 2-D, S200-1, 80 MIL

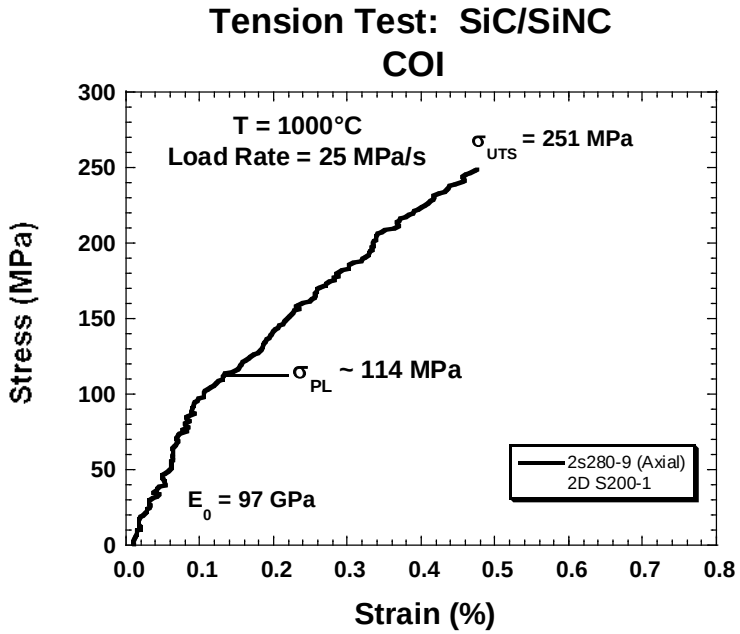


**Figure C-1.1: 2-D, S200-1, 80 mil Stress vs. Strain Plot (2s280-9)**

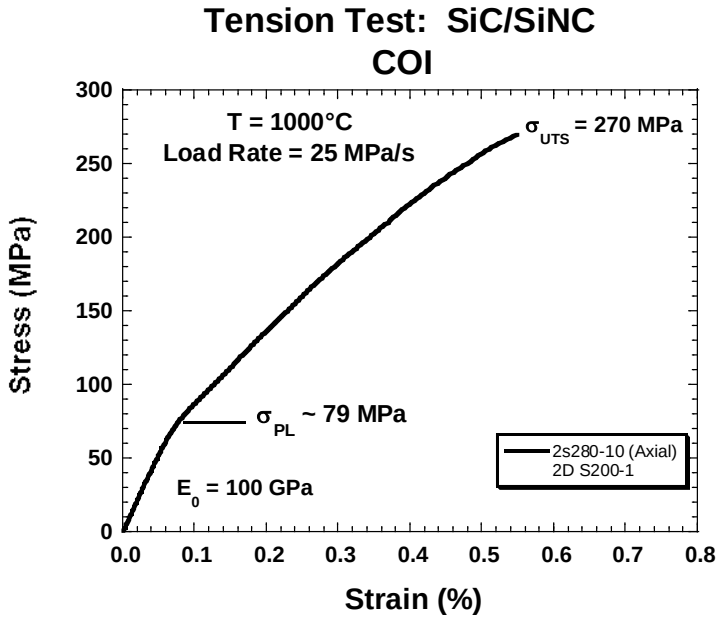


**Figure C-1.2: 2-D, S200-1, 80 mil Stress vs. Strain Plot (2s280-10)**

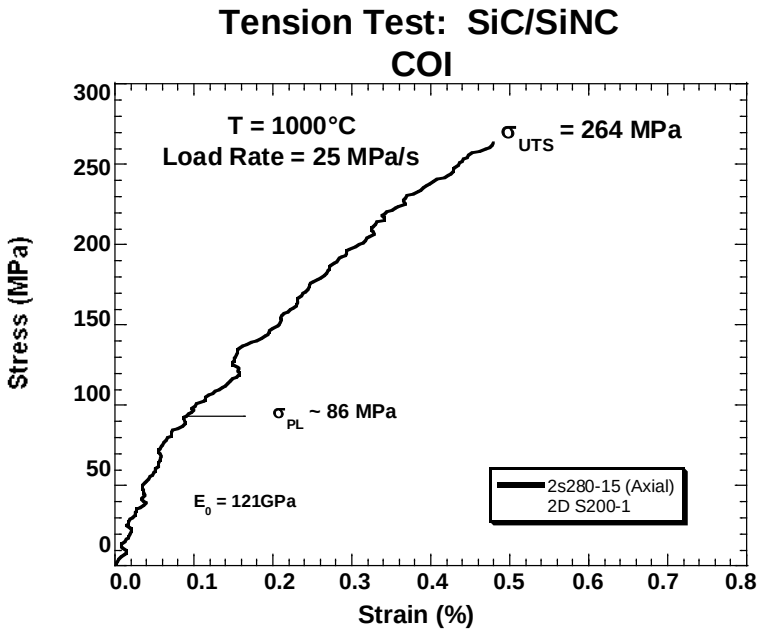


**Figure C-1.3: 2-D, S200-1, 80 mil Stress vs. Strain Plot (2s280-15)**

## C-2 3-D, S200-1, 80 MIL

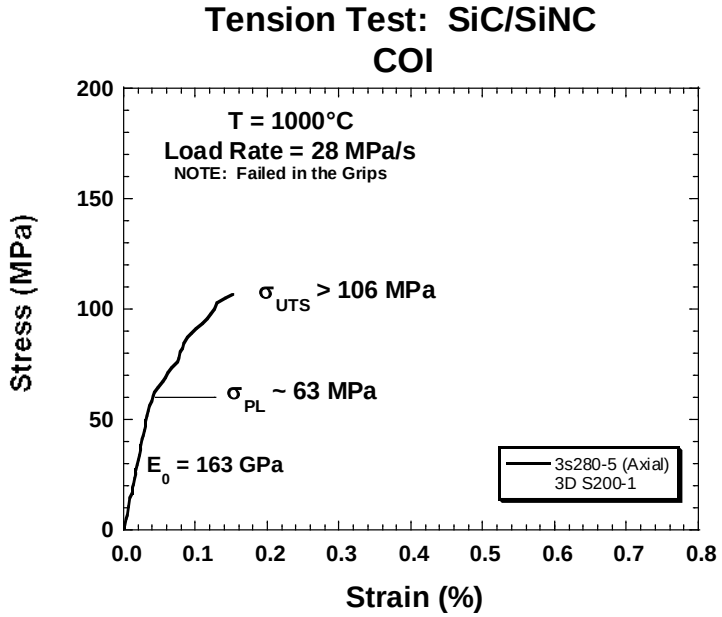


**Figure C-2.1: 3-D, S200-1, 80 mil Stress vs. Strain Plot (3s280-5)**

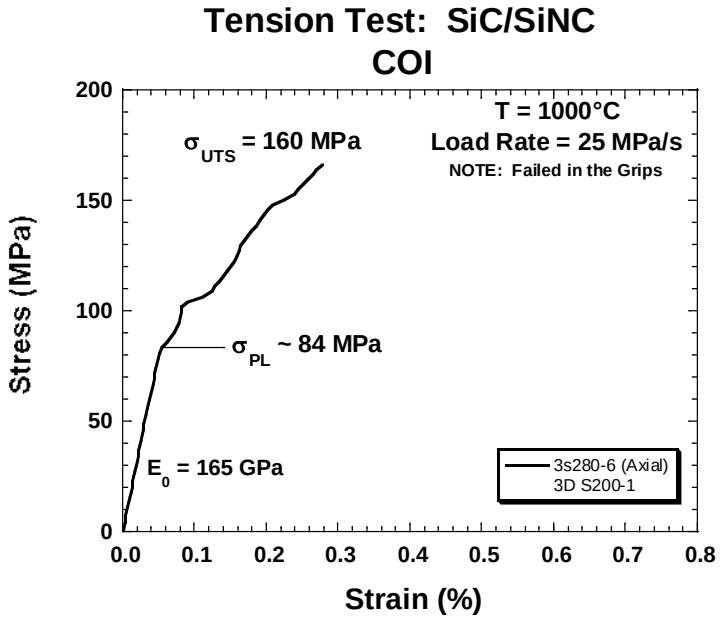


**Figure C-2.2: 3-D, S200-1, 80 mil Stress vs. Strain Plot (3s280-6)**

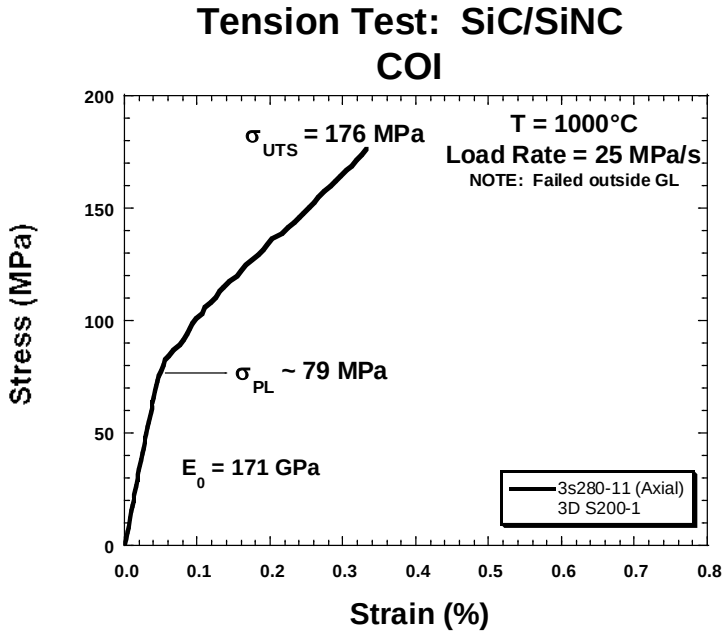


**Figure C-2.3: 3-D, S200-1, 80 mil Stress vs. Strain Plot (3s280-11)**

## C-3 3-D, S200-1, 145 MIL

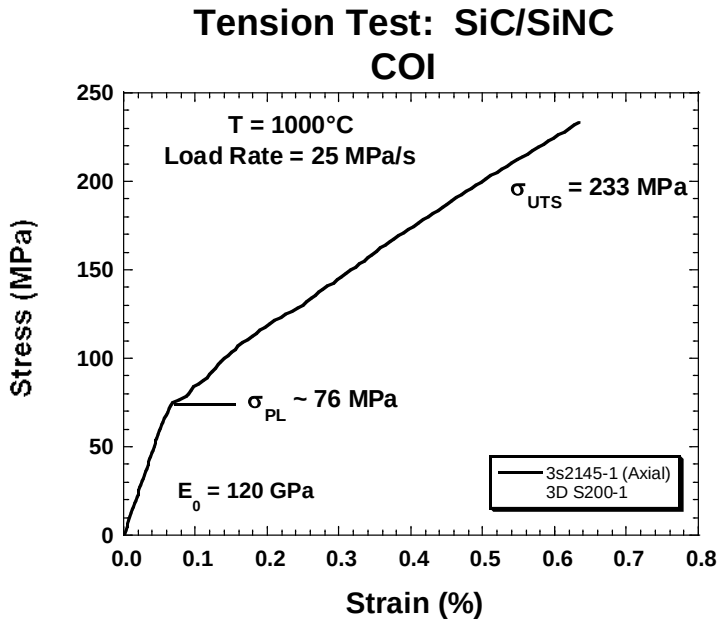


**Figure C-3.1: 3-D, S200-1, 145 mil Stress vs. Strain Plot (3s2145-1)**

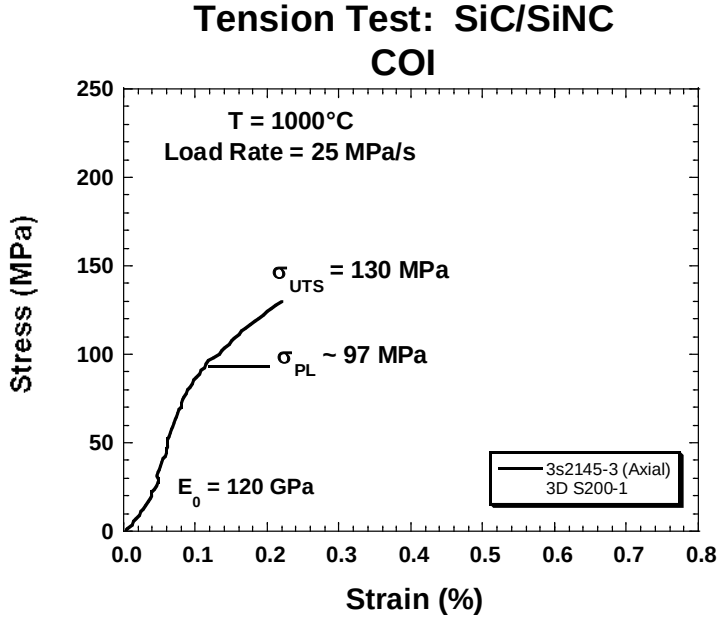


**Figure C-3.2: 3-D, S200-1, 145 mil Stress vs. Strain Plot (3s2145-3)**

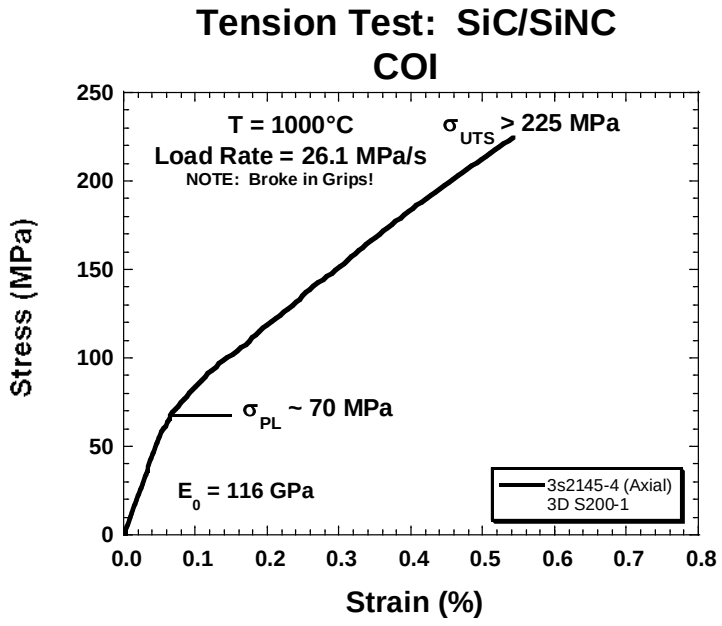


**Figure C-3.3: 3-D, S200-1, 145 mil Stress vs. Strain Plot (3s2145-4)**

## C-4 3-D, STARFIRE, 80 MIL

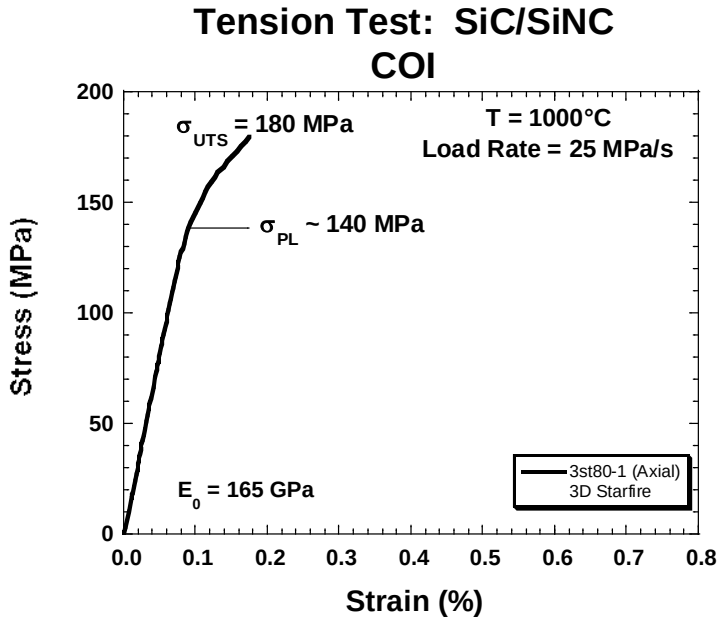


**Figure C-4.1: 3-D, Starfire, 80 mil Stress vs. Strain Plot (3st80-1)**

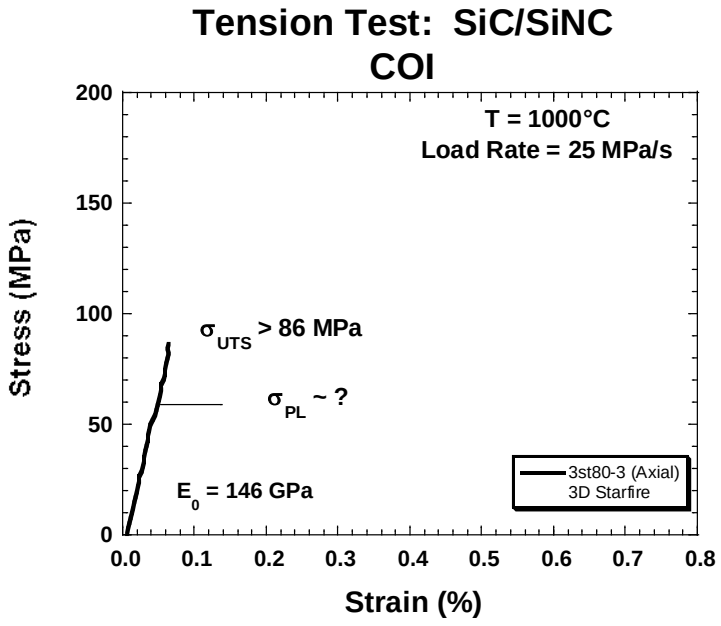


**Figure C-4.2: 3-D, Starfire, 80 mil Stress vs. Strain Plot (3st80-3)**

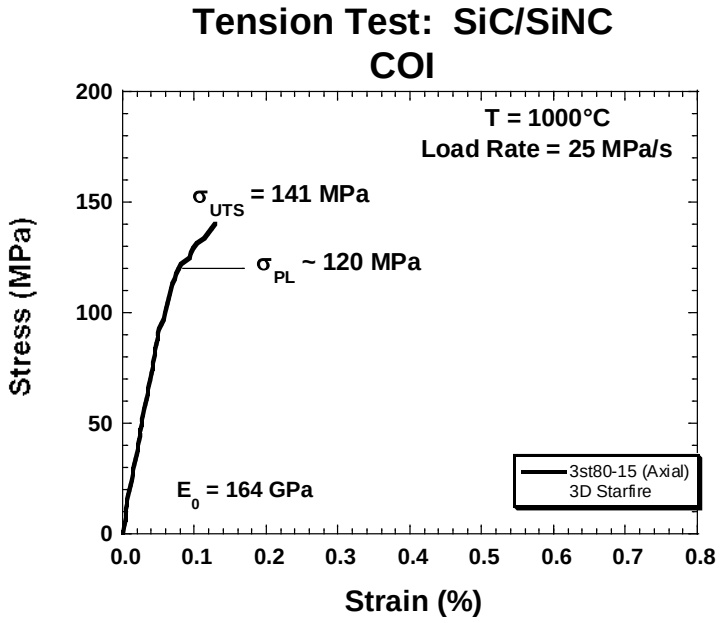


**Figure C-4.3: 3-D, Starfire, 80 mil Stress vs. Strain Plot (3st80-15)**

## C-5 3-D, STARFIRE, 80 MIL

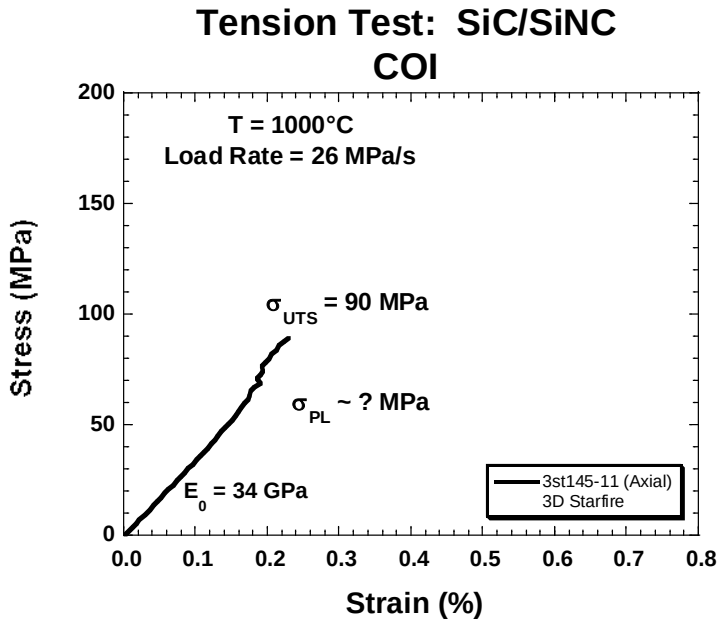


**Figure C-5.1: 3-D, Starfire, 145 mil Stress vs. Strain Plot (3st145-11)**

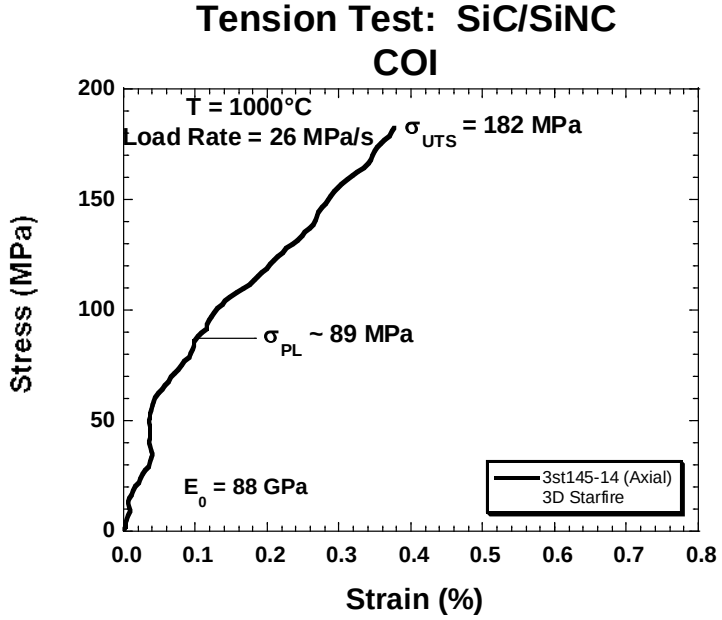


**Figure C-5.2: 3-D, Starfire, 145 mil Stress vs. Strain Plot (3st145-14)**

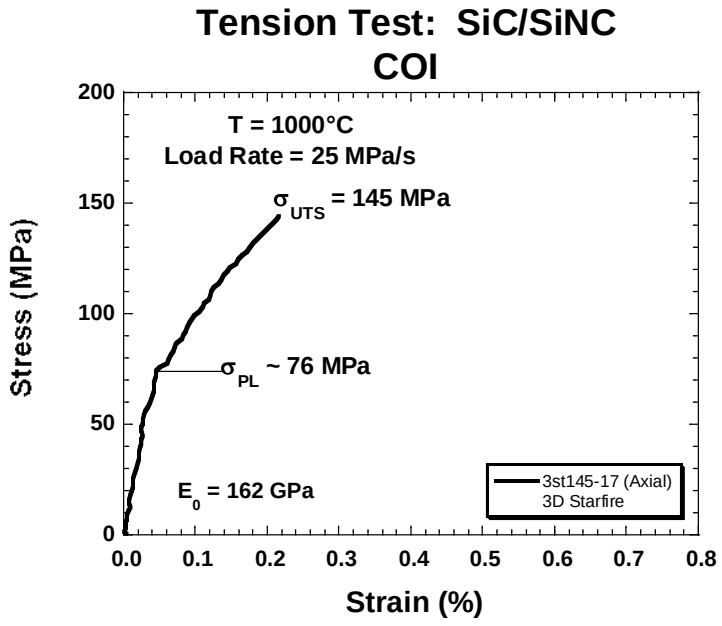


**Figure C-5.3: 3-D, Starfire, 145 mil Stress vs. Strain Plot (3st145-17)**

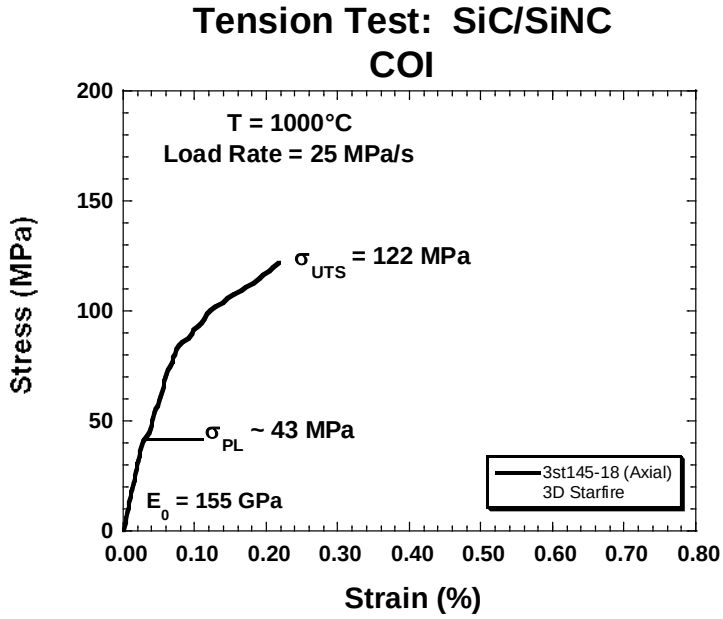


**Figure C-5.4: 3-D, Starfire, 145 mil Stress vs. Strain Plot (3st145-18)**

## LIST OF ACRONYMS, ABBREVIATIONS, AND SYMBOLS

| | |
|---|---|
| 2-D | Two-dimensional |
| 3-D | Three-dimensional |
| 8HSW | Eight-harness satin weave |
| AFRL | Air Force Research Laboratory |
| AFRL/RXCC | Composites Branch, Structural Materials Division of the Materials & Manufacturing Directorate, Air Force Research Laboratory |
| AFRL/RXSA | Acquisition Systems Support Branch, Structural Materials Division of the Materials & Manufacturing Directorate, Air Force Research Laboratory |
| ASTM | American Society for Testing and Materials |
| BN | Boron nitride |
| CG | Ceramic grade |
| CMC | Ceramic-matrix composite |
| COIC | COI Ceramics, Incorporated |
| DNC | Double-notch compression |
| E | Modulus of elasticity |
| $\varepsilon_f$ | Strain at Failure |
| GE | General Electric |
| GTE | Gas turbine engine |
| PIP | Polymer-infiltrated pyrolysis |
| PL | Proportional limit |
| RT | Room temperature |
| SEM | Scanning electron microscope |
| SiC | Silicon carbide |
| $Si_3N_4$ | Silicon nitride |
| SiNC | Silicon nitrocarbide |
| SiOC | Silicon oxycarbide |
| UDRI | University of Dayton Research Institute |
| USAF | United States Air Force |
| UTS | Ultimate tensile strength |